National Library of Canada
Acquisitions and Bibliographic Services Branch
395 Wellington Street
Ottawa, Ontario
K1A 0N4

Bibliothèque nationale du Canada
Direction des acquisitions et des services bibliographiques
395, rue Wellington
Ottawa (Ontario)
K1A 0N4

Your file Votre référence

Our file Notre référence

NOTICE

The quality of this microform is heavily dependent upon the quality of the original thesis submitted for microfilming. Every effort has been made to ensure the highest quality of reproduction possible.

If pages are missing, contact the university which granted the degree.

Some pages may have indistinct print especially if the original pages were typed with a poor typewriter ribbon or if the university sent us an inferior photocopy.

Reproduction in full or in part of this microform is governed by the Canadian Copyright Act, R.S.C. 1970, c. C-30, and subsequent amendments.

AVIS

La qualité de cette microforme dépend grandement de la qualité de la thèse soumise au microfilmage. Nous avons tout fait pour assurer une qualité supérieure de reproduction.

S'il manque des pages, veuillez communiquer avec l'université qui a conféré le grade.

La qualité d'impression de certaines pages peut laisser à désirer, surtout si les pages originales ont été dactylographiées à l'aide d'un ruban usé ou si l'université nous a fait parvenir une photocopie de qualité inférieure.

La reproduction, même partielle, de cette microforme est soumise à la Loi canadienne sur le droit d'auteur, SRC 1970, c. C-30, et ses amendements subséquents.

Canada

A Method for Full-Field Mechanical Testing of Biological Membranes Based on Electronic Speckle Pattern Interferometry (ESPI)

by
Paul Gilles Charette

A thesis submitted to
the Faculty of Graduate Studies and Research
in partial fulfillment of the requirements for the degree of
Doctor of Philosophy

Biorobotics Laboratory
Department of Biomedical Engineering
McGill University
June, 1994

ISBN 0-612-05686-4

Canada

SHORT TITLE

Full-field mechanical testing of biological membranes

Abstract

This thesis presents a novel method for mechanical testing of biological membranes. Although the method was developed specifically to study the stress and strain properties of pericardium (the membrane which encloses the heart), it is general in scope and is applicable to many other tissue types. Unlike existing test methods which only sample the material strain at a few selected points, the technique described in this thesis is a true *full-field* method: that is, the strain field is sampled uniformly at a high number of points across the entire material surface. The displacement and strain measurements are performed using laser-based *electronic speckle pattern interferometry* (ESPI) operating in transmission mode. Furthermore, unlike existing methods which only provide pure biaxial testing, the apparatus described here can apply any arbitrary planar stress configuration to the membrane under test, so that any aspect of the material behavior may be selectively emphasized.

In the course of this work, a new technique of phase unwrapping was developed to analyze optical phase images with a high noise content, such as speckle images. The method is robust and allows the analysis to be completely automated. Finally, the large volume of data generated by the experimental apparatus was analyzed and modeled using the *finite element method*. In traditional applications, finite elements are used to *predict* the behavior of material structures from known constitutive laws. In this application however, the finite element method was used for *distributed parameter estimation* in order to identify the unknown constitutive properties of the material under investigation. Experimental results which validate the entire procedure are presented. Calibration procedures, as well as theoretical noise calculations along with confirming experimental measurements are given.

Résumé

Cette thèse présente une nouvelle méthode pour faire l'étude des propriétés mécaniques des membranes biologiques. Quoiqu'elle ait été développée pour étudier spécifiquement le péricarde (la membrane enveloppant le coeur), le champ d'application de cette méthode est tout à fait général. Elle peut donc être employée avec n'importe quelle autre membrane biologique.

Par opposion aux méthodes existantes, qui mesurent les déplacements en quelques points seulement, la méthode décrite ici mesure les déplacements en tous points, c'est-à-dire de manière continue et sur toute l'étendue de la surface de la membrane. De plus, au contraire des méthodes existantes qui n'appliquent que des contraintes dans deux axes, cette méthode peut appliquer n'importe quelle combinaison de contraintes dans un plan. Les déplacements sont mesurés au moyen de la technique interférométrique laser "*electronic speckle pattern interferometry* (ESPI)" en mode de transmission.

Au cours de ce projet, une nouvelle technique de transformation de phase a également été developpée pour analyser des images de phase optique contaminées par un haut niveau de bruit. Cette technique est suffisamment robuste pour permettre une analyse entièrement automatisée des images. Enfin, les données expérimentales sont analysées et modélisées au moyen de la technique des *éléments finis*. Celle-ci est normalement utilisée pour prédire le comportement d'une substance dont les propriétés physiques sont connues. Ici par contre, elle est utilisée pour identifier de manière continue les propriétés inconnues de la membrane à l'étude. Des analyses théoriques de bruit ainsi que des résultats d'expériences confirmant la théorie et démontrant le bon fonctionnement des différentes étapes de la méthode sont présentés.

Acknowledgements

I wish to express my sincerest gratitude to my thesis director, Dr. Ian W. Hunter. The remarkable breadth and depth of his knowledge in so many different fields of science was an inspiration to me, and working in his group was a privilege. His outstanding ability as a builder of scientific apparatus and the incredible diversity of resources available in his laboratory made possible the ambitious scope of this work.

I wish to thank Dr. Morrel P. Bachynski, President of MPB Technologies Ltd. His company's support in funding and equipment were much appreciated.

I am grateful to Dr. Peter Hunter for having invited me to the University of Auckland in New Zealand to work on applied mathematics with him for two months. Our lively discussions on the finite element method in Whangamata allowed me to use this powerful tool as a basis for the analysis of my results. I am also in his debt for the material law fitting results presented in this thesis.

Special thanks to my colleague, Serge Lafontaine, whose tireless help was invaluable in many aspects of this work, at all hours of the day and night.

I thank my colleagues from the Biorobotics lab: Sander Boelen, Colin Brenan, Tilemachos Doukoglou, and Sylvain Martel for their help in various aspects of this work. I also thank Dr. Jason Bates for providing the pericardium samples.

Last but certainly not least, I am grateful to my lovely wife, Manon. Her seemingly never–ending reserves of patience, cheerfulness, and encouragement made it all worthwhile in the end. I am also very grateful for the support and encouragement I received from my family: Lyse, François, Dana and Alain, and especially from my parents, Yvette and Gilles.

Finally, I gratefully acknowledge the financial support accorded to me by le Fonds FCAR du Québec and the Medical Research Council of Canada.

Table of Contents

Lists of Figures Plates and Tables

Chapter 1

Introduction

This chapter describes the context and reasons for the rising interest in studying the mechanical properties of biological membranes. The significant challenges involved in this task are explained. Current methods of testing are reviewed and their deficiencies are pointed out. The rationale for developing a new method is explained and the fundamental design goals of the new method are outlined.

1.1 Mechanical testing of biological membranes

Many organs and tissues in the human body can be characterized as two dimensional "sheets" or "membranes", such as the stomach, bladder, uterus, skin, pleura, blood vessels, cornea, pericardium, and many more. In order to better understand the normal function of these tissues and the mechanisms which lead to their failure, their mechanical characteristics must be well understood. Similarly, in order to replace diseased or damaged tissue with synthetic or biological substitutes, the mechanical behavior of the replacement candidates must be measured and certified against the known characteristics of the original tissue in a healthy state.

The mechanical study of biological membranes is thus an important branch of the science of Biomechanics, which in itself is an important tool in the field of medicine. Indeed, to quote Fung (1981): "Physiology can be no more understood without Biomechanics than an airplane can without aerodynamics". Similarly, the mechanical function of the different biological membranes in the body can only be fully understood through experiments specifically designed for this purpose. The challenge is acute as most biological materials have markedly non-linear mechanical properties and generally exhibit large shear and bending strains within an elastic range which considerably exceeds that of most engineering materials (Thubrikar and Eppink, 1982).

Methods of testing biological membranes are generally aimed at identifying the constitutive properties of the material which relate imposed *stress* (force per unit area) to

resulting *strain* (deformation). The ultimate objective is to construct a constitutive model of stress and strain from the experimental data and then use the model to understand and predict the behavior of the tissue in a variety of circumstances. The model can also be used as a "standard" against which any artificial replacements can be compared.

Unfortunately, all existing methods of testing biological materials still fall short of the ultimate goal of fully characterizing the complex properties of living tissues (see Section 1.3). Although many current methods are more elaborate than standard engineering test methods, they nonetheless lack the number of degrees of freedom and spatial sampling requirements needed to measure the complete mechanical behavior of living tissue effectively. For this reason, a novel method of testing biological membranes which seeks to achieve this goal was developed and is described in this thesis. The method, which combines a number of recent but proven advanced engineering techniques, provides a rich amount of information not previously attainable using existing designs.

1.2 A case in point: Pericardium

The motivation behind the development of this new technique was the need to obtain detailed mechanical knowledge about the *pericardium* (the thin membranous sac which encloses the heart), in the context of our group's interest in the modeling of cardiac mechanics (Hunter and Smaill, 1988; Smaill and Hunter, 1991). Note that although the pericardium was our most immediate interest at the time of development, the new technique was designed to be applicable to any biological membrane and hence is completely general in scope.

The *pericardium*, which surrounds the heart in most mammals (Holt, 1970), actually consists of two membranes made of two tissue types (see Figure 1.1). The first tissue type is the thin *serous pericardium* which is composed of a single smooth layer of epithelial cells. The second tissue type is the much thicker *fibrous pericardium* which is composed of interlaced collagen and elastin fibers. The inner membrane, known as the *visceral pericardium* or *epicardium* consists of a single layer of serous pericardium which covers the outside of the heart wall. The outer membrane, known as the *parietal pericardium* or *pericardial sac* consists of an outer layer of fibrous pericardium and an inner layer of serous pericardium. The parietal pericardium thus forms a tough fibrous sac which encloses the heart and merges with the great vessels at the top. The thickness and number of attachment points to neighboring organs of the parietal pericardium vary among species.

The *parietal cavity*, which separates the visceral and parietal pericardia, is filled with the *pericardial fluid.*

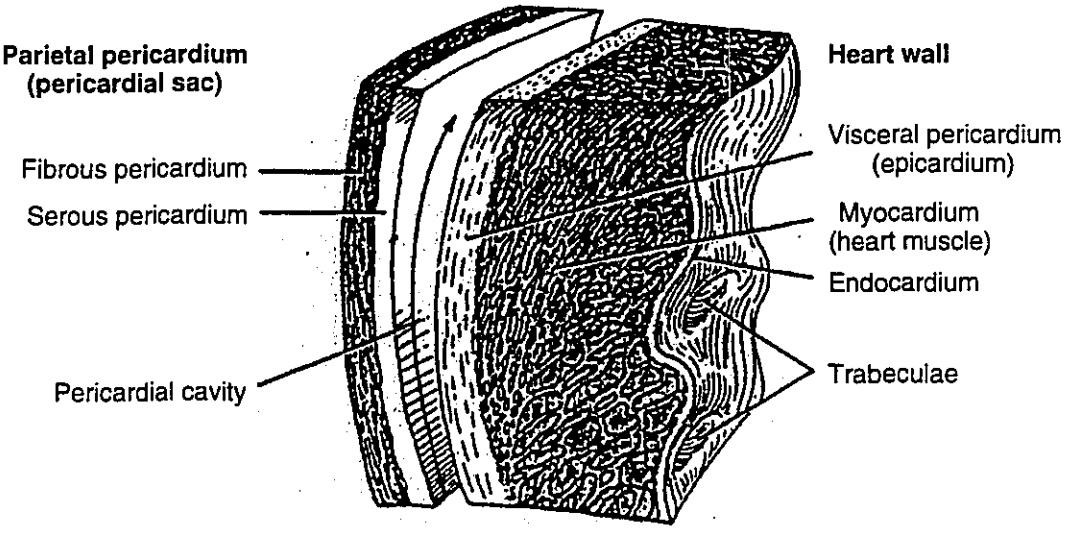

Figure 1.1: The pericardium (taken from Zioupos, 1989).

Note that, of the two pericardial membranes, it is the parietal pericardium which plays the major role in cardiac mechanics and as such has been extensively studied. The visceral pericardium is considered as an integral part of the heart and is not studied on its own. Henceforth in this thesis, as in the literature, the parietal pericardium will be referred to simply as "the pericardium".

Although the anatomy and histology of the pericardium are well documented (Holt, 1970), the role played by the pericardium in cardiac mechanics is still controversial (Tyberg *et al.*, 1986). It is thought that the pericardium serves to hold the heart in a fixed position and protect it from neighboring organs (Vito, 1979), that it prevents over-distention of the heart, enhances the interaction between the ventricles and affects the ventricular pressure-volume curve (Kanazawa *et al.*, 1983; Chew *et al.*, 1986; Lee *et al.*, 1985), and facilitates cardiac pressure work (Franklin and Davie, 1991). Pericardium is not essential to life (Vito, 1979), indeed it is often removed during cardiac surgery. However, constrictive pericardial function can be fatal in pathological situations such as cardiac tamponade (impairment of diastolic filling of the heart caused by a rise in the intrapericardial pressure) and constrictive pericarditis (swelling of the pericardium).

In any case, more detailed knowledge of the mechanical behavior of the pericardium is required to unequivocally determine its effect on the pumping action of the heart. As stated above, existing methods have been unable to resolve this question completely, which is why the new method described in this thesis was developed.

Note also that quite apart from its role in cardiac mechanics, pericardium is also extensively studied in the context of artificial heart valves (Crawford *et al.*, 1986; Zioupos *et al.*, 1992; Purinya *et al.*, 1994). Indeed porcine (pig) and bovine (cow) pericardium sheets have been used for over 15 years to manufacture artificial aortic valves because of their excellent longevity and resistance to repeated bending and shear. However, better evaluation techniques are also required in this industry for selecting prime valve material from raw pericardium sheets (Zioupos, 1991).

1.3 Review of current methods of testing biological membranes

The pericardium, like most biological membranes, is generally considered to be non-linear, inhomogeneous, anisotropic and viscoelastic (Choi and Vito, 1990; Zioupos *et al.*, 1992). It is also found by all recent studies to exhibit significant hysteresis and in that sense, it is not a truly elastic material. In short, it is not a simple material to test. However, since biological materials are generally considered to be incompressible (i.e.: a material for which the bulk modulus is many orders of magnitude larger than the shear modulus or Young's modulus), a full three dimensional model can be derived from complete two-dimensional tests (Vito, 1980).

Several groups have attempted to develop methods for mechanically characterizing pericardium and other biological membranes, to varying degrees of success. In the paragraphs below, a review of the three most common methods (uniaxial, inflation, and biaxial) is presented. Note that the review is not restricted to applications of pericardium testing since most techniques are applicable to any type of biological membrane. Note also that the review covers the last 25 years only since this period has seen the most important milestones in the evolution of biological materials testing, with the advent of computers and electronics technology. Many of the conclusions reached before this time are now open to question.

1.3.1 Uniaxial testing

In this simplest of methods, often used to test standard engineering materials, a thin strip excised from a membrane is clamped rigidly at one end and stretched at the other with an actuator. Forces exerted by the actuator are recorded with a transducer to calculate applied stress. In order to determine average normal strain, the total length change of the sample is determined either by recording the position of the moving clamp or by visually tracking markers affixed to the membrane surface.

Although uniaxial testing methods are only truly appropriate for tissues which experience forces along a single axis (such as muscle fibers, tendons or ligaments), they do nevertheless yield useful if incomplete information. Recent examples of such uniaxial tests (which are rarely published today for biological membranes) were performed on canine and human pericardium, as reported by Vito (1979) and Lee & Boughner (1985) respectively.

1.3.2 Inflation testing

In this type of testing, a patch of material is rigidly clamped along its outer edge over an aperture in a pressure vessel and inflated by positive pressure to form a bubble shape. When the inflating pressure P and radii of curvature R_1 and R_2 in the two orthogonal axes at the apex are known, the orthogonal tension components T_1 and T_2 in the plane of the sheet can be calculated using the Young-Laplace law for spheres:

$$P = \frac{T_1}{R_1} + \frac{T_2}{R_2}. \tag{1.1}$$

Hildebrand *et al.* (1969) used this method to test rubber, cat mesentery and pericardium. Displacements of the membrane at the apex and three other neighboring points were determined by using a microscope with a shallow depth of field objective to focus on four small beads cemented onto the membrane surface. Strain was computed in three directions 60^{o} apart by tracking the change in spacing between the beads.

More recently, Zioupos *et al.* (1992) reported on the use of a similar inflation technique to test the direction of anisotropy in bovine pericardium used for manufacturing artificial aortic valves. In this case however, a more powerful Moiré-based method was used to measure full field out-of-plane displacements (Kreske *et al.*, 1988).

1.3.3 Biaxial testing

The most complete of the current methods of testing biological membranes use a biaxial arrangement to stretch the material along two orthogonal axes in the plane independently (see Figure 1.2). The mechanical arrangement is identical in both axes, where the membrane is attached with sutures or clamps from both sides to stages. In the simplest mechanical arrangement, there are two moving stages and two fixed stages, as shown in Figure 1.2. In slightly more complex systems, the opposing stage pairs are mounted on a common lead screw and are driven in opposite directions by an actuator which rotates the lead screw. Forces are measured with a transducer mounted between the clamping arrangement and the stages.

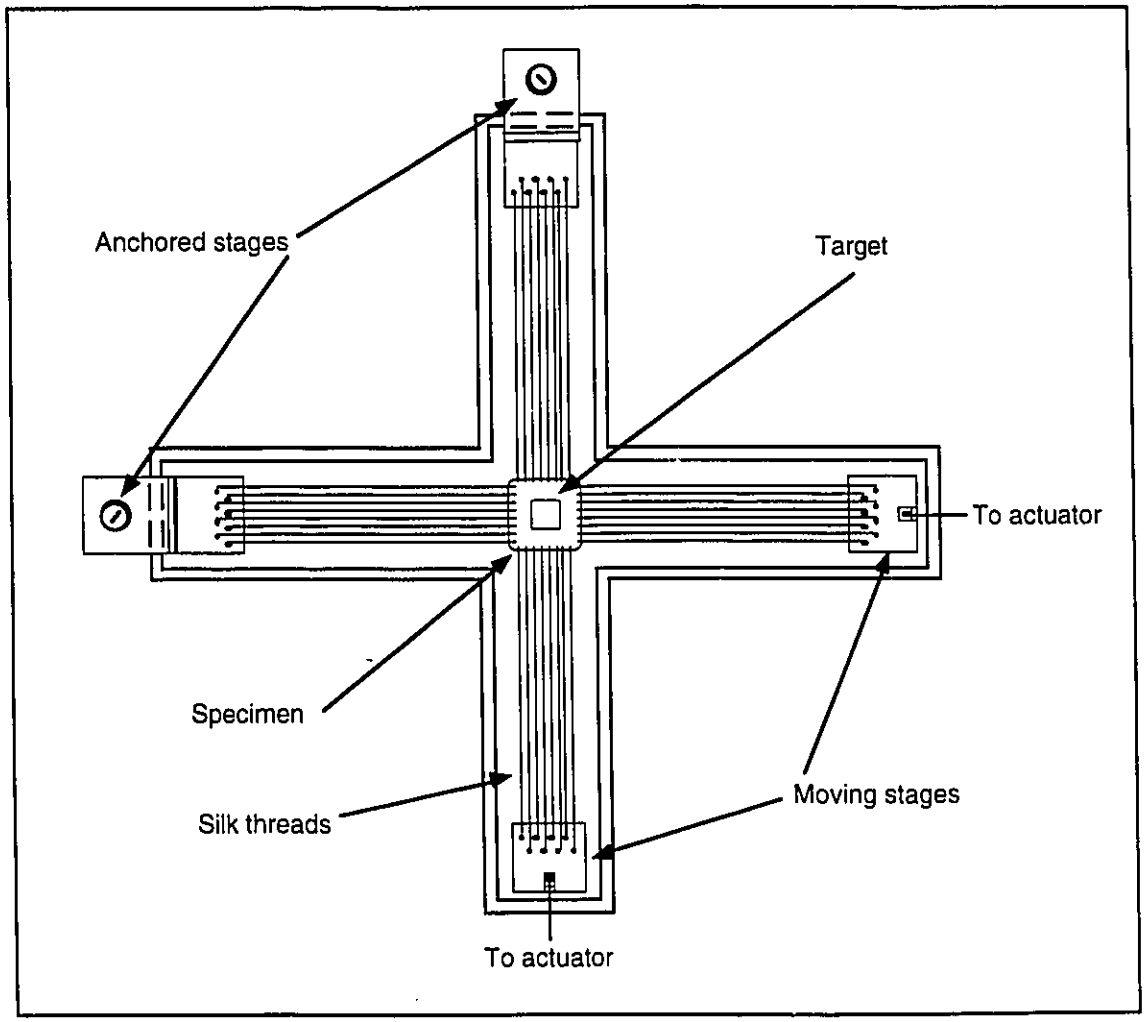

Figure 1.2: Biaxial testing rig for compliant biological tissue (reproduced from Lanir and Fung, 1974).

Early work by Lanir and Fung (1974) on rabbit skin inspired many subsequent workers in the field, both for experimental procedure and mathematical modeling. In their experimental apparatus, as is the case later on with Chew *et al.* (1986), the displacements in the central region of the membrane under test were estimated from the shape and position of a target shaped like the outline of a square (see Figure 1.2). The distances between opposing sides of the target were measured using two video cameras connected to video dimension analyzers. The average normal strains in the two orthogonal directions in the plane could then be estimated from the change in width and height of the target.

In a similar system, using instead a target shaped like a solid square, the width and height of the target were measured either with two video dimension analyzers in the case of Lee *et al.* (1985) or with two linear CCD arrays in the case of Vito (1980). Note that both targeting methods measure average normal strains only and rely on the uniformity of the strain field in the target area. If this is not the case, the measured average strains will not be an accurate reflection of the true strains.

A more interesting method of measuring strain in biaxial testing was first proposed by Hoffman and Grigg (1984) and subsequently used by Humphrey *et al.* (1987), Choi and Vito (1990), and Nielsen *et al.* (1991). In this method, four spot markers are positioned at the corners of a square area in the central region of the membrane where the strain is to be measured. The marker displacements during the experiments are recorded on video tape. Their trajectories are then determined subsequently from the video record either manually with a mouse or automatically using an appropriate image processing algorithm. The strain within the 4-sided polygonal area delimited by the four markers can then be continuously interpolated using bilinear basis functions, based on the displacements at the nodes. This method enables shear as well as normal strains to be estimated.

1.4 Deficiencies of current methods of testing biological membranes

The three methods outlined above each have a number of deficiencies which restrict the type of mechanical information that can be extracted from samples in an experiment. In the uniaxial case, simple elongation tests on strips cut from sheets do not in general enable the prediction of the mechanical behavior of the complete sheet (Hildebrand *et al.*, 1969). It is thought furthermore that damage to the fiber network in membranes such as pericardium

may be inevitable when a narrow strip is prepared (Lee *et al.*, 1985), thus changing its mechanical properties.

In the case of inflation testing, the simple Young-Laplace model yields no information on shear stress. Furthermore, because of the coupled system used to apply a deformation to the membrane, forces cannot be applied independently in different axes.

In the biaxial case, the simplest method of measuring strain (using square targets) yields an average measurement of normal strains only, without any shear information. The underlying assumption is that the strain field in the target area is completely uniform. In the case of the interpolated strain measurement with the four markers, the assumption is that displacements sampled at only four points will give an accurate reflection of the strain field across the entire central region of interest. In both cases, the strain ends up being grossly approximated under any but the simplest of testing protocols, and there is no direct way of verifying that the underlying assumptions indeed hold.

Because forces are imposed and measured in the normal directions only, there is no information acquired about how the membrane reacts to imposed shear stresses. Also, boundary forces applied to the central measurement target area cannot be determined directly: they must be estimated from the externally applied forces. The accuracy of this process remains uncertain, according to Nielsen *et al.* (1991). Indeed, they present the only quantitative study to our knowledge of how the stress and strain fields in a central region of interest are related to the applied boundary forces and to the overall membrane dimensions. Interestingly enough, Nielsen *et al.* (1991) found that the accuracy to which the stresses in the central region could be estimated is load dependent. Furthermore, since their analysis was performed under the assumptions of homogeneity, isotropicity and symmetric biaxial testing only, they state that for anisotropic and/or inhomogeneous materials, the applied forces would be considerably more complex to interpret.

Finally, membranes such as pericardium are considered to be *orthotropic*, where the anisotropy is characterized by preferred directions in the material behavior. If the material axes are not lined up correctly with the actuator stretching axes in pure biaxial tests, the difference in material properties in the two orthogonal directions cannot be measured independently and the test results are considerably prone to error (Choi and Vito, 1990). Indeed, in the worst case scenario when the material axes are aligned at 45° to the pulling axes, a highly orthotropic membrane might be perceived as being perfectly isotropic (Choi and Vito, 1990).

Although the anisotropy of pericardium is no longer in question today, the debate about the *direction* of preferred material axes continues. For example in the case of canine pericardium, Lee *et al.* (1985) and Choi and Vito (1990) reported that the degree and direction of anisotropy varied among specimens and showed no consistent anatomical direction of maximum stiffness. Mann *et al.* (1986) found that the pericardium *in-vivo* stretches mainly in the circumpheral direction and very little in the longitudinal direction. Chew *et al.* (1986) reported that the direction of anisotropy seemed to be history dependent! In the case of bovine pericardium, Zioupos *et al.* (1992) found that the direction of greatest extendibility lies within a 10° angular range about the circumpheral direction. Hence there is no consensus yet on how to resolve this basic issue and it is an *essential* requirement to obtain meaningful results using the biaxial testing method.

Clearly, a more powerful method of testing biological membranes is required which does not rely on a-priori restrictive assumptions about the behavior of the stress and strain fields in the membrane, or on any preferred direction in the material properties. It is this need which the method described in this thesis seeks to address.

1.5 A new method

In order to model the mechanical behavior of a material under test, the experimenter seeks to discover the relation between two physical quantities: applied stress and resulting strain. These quantities in turn are derived from two directly measurable experimental variables: applied forces and resulting material displacements.

The ideal method of mechanical testing complex materials such as biological membranes will fulfill the following conditions:

1) the applied forces at the boundary of the region under investigation in the material (the "field boundary") must be measured directly.

2) the available repertoire of applied stress fields must be extensive and completely general, in order to selectively or collectively emphasize any particular aspect of the material behavior.

3) the resulting displacements must be sampled throughout the material with a sufficiently high spatial sampling rate such that the measurements closely reflect the spatial structure of the strain field.

The first condition is achieved by using the entire membrane as the experimental target, not just a central area where the fields are well behaved. In this manner, the field

boundary and the membrane boundary are one and the same, where the forces are applied and directly measured. The second condition is achieved by using a sufficiently large number of actuators to pull at the membrane boundary from many directions independently, not simply in two orthogonal axes. The third condition is achieved by using a *full field* displacement measurement technique. The new method described in this thesis incorporates all three required attributes and thus imposes few if any restrictions on both the applied stress and resulting strain fields.

Full field techniques are methods of measuring a material property of interest in a spatially continuous manner, as opposed to taking measurements at a few discrete points. The available options for full field *in-plane displacement* measurements are (Walker and McKelvie, 1987):

(1) Moiré methods
(2) Holography
(3) Speckle methods
(4) Photo-elasticity
(5) Brittle lacquers

Because the material under test is a compliant biological membrane, the displacement measurement technique used must be mechanically non-invasive, in order not to affect the material behavior in any way. This fact alone excludes photo-elasticity and brittle lacquer techniques which both require the application of a coating to the material surface. This requirement also eliminates Moiré methods (Kreske *et al.*, 1988; Johnson *et al.*, 1989) which require bonding a grid to the material surface for in-plane displacement measurements.

This leaves holography and speckle methods (Ennos, 1968; Sciammarella and Narayanan, 1984; Jones and Wykes, 1989). Of all the speckle methods, speckle interferometry is the most powerful and the most versatile. Both holography and speckle interferometry are laser-based full field measurement techniques that have been successfully used with biological materials. For example, Kasprzak *et al.* (1994) report on the use of holography to measure changes of corneal curvature due to intraocular pressure changes and Conerty *et al.* (1992) report on the use of speckle interferometry with a fiber optic probe to measure tympanic membrane and vocal chord vibrations.

Although holography provides more visually pleasing images, speckle interferometry has several important advantages in practice. Indeed, the directional and magnitude sensitivity of speckle interferometry can be varied over a much larger range than with holography (Jones and Wykes, 1989). For all but the normal viewing direction (Jones

and Wykes, 1989), holographic techniques are sensitive to both in-plane and out-of-plane displacement gradients. Hence, in order to obtain in-plane displacement information only, the out-of-plane displacement information viewed in the normal direction must be separated from the combined in-plane and out-of-plane displacement information viewed from two other separate directions. Furthermore, in most practical cases, all three holographic viewing directions will have different displacement sensitivities. In contrast, speckle interferometers can be constructed in such as way as to be selectively sensitive to different displacement directions. For example when the material under investigation is a membrane, a simplified optical arrangement will enable measurements of in-plane displacements only.

To quote Stetson (1975) :"How many scholars would be willing to say that the most practical thing holography has done is to have called out attention to laser speckle?". Although this statement is probably intended as an exaggeration, it does nonetheless humorously illustrate the fact that, in the opinion of many, speckle interferometry is better suited to obtain quantitative results and often simply more practical to use as reported by Ratnam *et al.* (1992). For this reason, and because of the many practical advantages described above, speckle interferometry was chosen as the full field displacement technique to be used in the method described in this thesis.

Finally, one of the greatest challenges faced in this project was to find a way of efficiently analyzing the large volume of data generated by this new method, in order to extract meaningful information from it. Indeed, forces are applied and sampled at several points around the membrane, and displacements are measured in a continuous manner across the entire membrane surface, as opposed to at a few discrete points. For this purpose, the premier tool for continuum systems analysis, the *finite element method*, was used as the framework for data representation, analysis, and modeling.

1.6 Thesis outline and organization

This last section explains the organization of the chapters in this thesis.

- Chapter 1 is the introduction.

- Chapter 2 describes the basic theoretical principles behind the speckle effect. The mechanism by which speckle can be used as an information carrier is detailed and typical experimental designs are shown.

- Chapter 3 describes the novel experimental apparatus designed for this project. The different subsystems (optics, mechanics, and data acquisition & control) are detailed separately.

- Chapter 4 describes the noise analysis and calibration issues for the displacement and force measurements. Whenever possible, theoretical noise estimations are derived and verified against experimental measurements.

- Chapter 5 describes the data acquisition and the first stage of the image analysis procedure. A novel phase unwrapping algorithm developed for this project is detailed and a review of the deficiencies of currently available methods are explained.

- Chapter 6 describes the finite element-based modeling, analysis, and distributed parameter estimation procedure.

- Chapter 7 is the conclusion, which emphasizes the important results of this thesis, lists the original contributions of this work, and suggests the orientation of future work.

- Appendix contains hard copies of the different windows in the software graphical user interface designed and built to control the experimental apparatus and analyze the results. The program, called XVG, incorporates over 35000 lines of C code.

Chapter 2

Speckle Interferometry

This chapter describes the various aspects involved in speckle interferometry. The first sections deal with the physics behind the formation of speckle and its characteristics. The second section explores the subject of speckle statistics and its relevance to material property measurements. The last section explains the principles of speckle interferometry and demonstrates how speckle can be used to determine material displacements.

2.1 The speckle effect

The "speckle effect" occurs whenever temporally coherent light is either reflected from an "optically rough" surface or passes through a medium with random index of refraction fluctuations (Dainty, 1975). When viewed on a screen or through an imaging system, the resulting light field appears as a randomly distributed pattern of granules or "speckles" of varying intensities (see Figure 2.1).

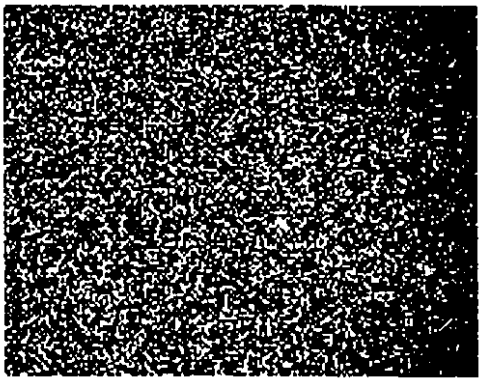

Figure 2.1: Speckle pattern generated by the transmission of laser light though medium with random index of refraction variations (in this case a thin biological membrane).

The speckle "pattern" or "field" as shown in Figure 2.1 results from the mutual interference of the individual coherent wavelets scattered by the surface micro-structures and/or by the index of refraction inhomogeneities, each having random relative phase. The

speckle pattern is not confined to a particular region in space but is in fact a stationary three dimensional interference pattern that fills the volume occupied by the interfering waves.

Interestingly enough, much of the early attention given to speckle was devoted to finding ways of reducing the occurrence of this phenomenon. Indeed in holography, speckle is an inevitable and undesirable noise source that degrades image quality. Many of the first workers in the field thus struggled with different methods of eliminating the speckle noise from the holograms. Soon afterwards however, it was discovered that the speckle field itself was an important information carrier, which from many respects was superior to the hologram.

Since the advent of the laser in the early 1960s, the study and use of speckle has increased dramatically. Today, speckle methods have become an important scientific tool for investigating the microscopic properties of material surfaces and structure. Much of the early work evolved mainly in the UK in the 1970s (Erf, 1978), specifically at the University of Loughborough. Erf (1978) elegantly sums up the birth of speckle as a useful tool from its initial unwanted beginnings with a quote from Benjamin Franklin:

> "Eliminate that which is bothersome,
> And your work shall be better for it; but-
> Find a use for that which offends thee,
> And thou shalt be twice rewarded."

There are two key elements in the formation of a speckle field. The first element is that the material which is used to generate the field must impose a randomly distributed pattern of optical delays on the incoming light wave. In other words, the phase of the incoming wavefront must be completely "scattered" or randomly changed at every point, either by the index of refraction inhomogeneities in the case of transmission, or by surface height variations (roughness) in the case of reflection, or both. When this phenomenon occurs, each point on the material surface can be considered as an individual point source of coherent Huygens wavelets, each with random phase. It is the coherent mutual interference of all those wavelets which then give rise to the speckle pattern. To give a contrary illustration, no speckle field is formed by the passage of light through a highly polished transparent plate (e.g. a glass plate) or by reflections from a mirror for example.

The second key element required for the formation of a speckle pattern is that the temporal coherence length of the light source must be much greater than the average phase

delay introduced by the surface micro-structures and/or by the index of refraction inhomogeneities. If this is not the case, the wavelets will not interfere coherently and no speckle pattern will form. Indeed, Hecht (1987) showed the results of an interesting experiment where the surface of a cement block was illuminated first with laser light and then with collimated light from an Hg arc lamp, both of about the same spatial coherence. While the temporal coherence length of the laser source was much greater than the surface feature dimensions, that of the Hg lamp was not. Hence the laser light photograph of the cement block shows a well developed speckle pattern completely obscuring the block surface features, whereas the Hg lamp photograph clearly shows the block surface, without speckles.

Finally, it should also be emphasized that speckles are not confined to visible light. Indeed, they occur at any wavelength in the electromagnetic spectrum, as well as in other areas such as acoustical imagery (Meunier *et al*, 1989), synthetic aperture radar (Goldstein *et al.*, 1988) or sub-atomic particle interactions (Dainty, 1975). Typical examples are the scattering of X-rays by liquids, radar "clutter", radio transmission "dead zones", and electron scattering by amorphous carbon films.

2.2 Statistical properties of speckle

As mentioned above, the use of speckle in science and engineering is motivated by the fact that the speckle field is an important information carrier. The most common uses of speckle-based methods are the measurement of small material displacements (for vibration and strain analysis for example), the measurement of object geometry or *contouring*, and the measurement of surface roughness (for surface finish evaluation for example). The link between the behavior and physical properties of interest of a given material under investigation and the properties of the corresponding speckle field is established by studying the statistics of speckle. It is thus an important subject which must be understood in order to extract quantitative information from the speckle pattern.

The study of the statistical properties of speckle is a large subject that has been and continues to be investigated by many authors both theoretically and experimentally. Only the most important aspects of speckle statistics are described in the following sections and their relevance to the application described in this thesis is emphasized. The discussion

below follows from the classical derivation of the statistics of a single linearly polarized speckle pattern, which is based on the following general assumptions:

(1) The diffusing or scattering medium consists of a large number of statistically independent scatterers.

(2) The phase and amplitude of each scattered wavelet are statistically independent of one another.

(3) All values of scattered wavelet phase in the $[-\pi,\pi]$ interval are equally likely.

(4) The incident wave is linearly polarized, and the scattering or diffusing medium does not depolarize the light.

(5) The wave is perfectly monochromatic.

(6) The size of the detector is greater than the speckle size.

Note that the classical derivation of speckle statistics pertains to speckle patterns generated by the *reflection* of a temporally coherent light wave from an optically rough surface. The conclusions of the analysis however are nevertheless equally applicable to the properties of a speckle pattern formed by the *transmission* of light through a material with index of refraction inhomogeneities. Indeed, the nature of the process which randomizes the optical phase and creates the speckle effect is immaterial: as long the assumptions listed above are fulfilled, a speckle pattern will be formed.

2.2.1 First order statistical properties of speckle

In this section, the statistical properties of speckle at a single point in space or "first order" statistics are described. The purpose of the discussion is to derive statistical expressions for the probability density of the irradiance and phase of the speckle field at every point. From these expressions, useful quantities such as the *speckle contrast* can be derived and related to the underlying material properties.

2.2.1.1 Statistics of a single linearly polarized speckle pattern

The approach taken below, after Goodman (1975) and Frieden (1991), is to derive the joint probability density function for the real and complex components of the electric field amplitude at a given point in space in the speckle pattern. The function is then inverted to obtain the joint probability density function for irradiance and phase. The joint density function is then integrated to separately give the marginal probability density functions for the irradiance and phase of the speckle pattern.

Let $u(x,y,z;t)$ represent the total linearly polarized electric field at point (x,y,z) in space at time t:

$$u(x,y,z;t) = A(x,y,z)e^{-i2\pi\nu t}, \tag{2.1}$$

where ν is the optical frequency and A represents the complex amplitude of the electric field with magnitude $|A(x,y,z)|$ and phase θ given by:

$$A(x,y,z) = |A(x,y,z)|e^{-i\theta(x,y,z)}. \tag{2.2}$$

The irradiance I of the electric field is then given by the following expression:

$$I(x,y,z) = \lim_{T\to\infty} \int_{-T/2}^{T/2} |A(x,y,z;t)|^2 dt = |A(x,y,z)|^2. \tag{2.3}$$

In the case of a speckle field, the amplitude A of the total electric field u will be the vector sum of a large number N of scattered wavelets. Let the wavelets have normalized complex amplitudes $N^{-0.5}a_k$, where $k = 1...N$, i.e.: each wavelet has a random phase θ_k and magnitude $N^{-0.5}|a_k|$. The amplitude of the total electric field is then given by:

$$A = \sum_{k=1}^{N} \frac{1}{\sqrt{N}} a_k = \frac{1}{\sqrt{N}} \sum_{k=1}^{N} |a_k| e^{-i\theta_k}, \tag{2.4}$$

where the subscripts "x,y,z" have been dropped to simplify the notation and all variables in the expressions below are understood to refer to quantities at a single point in space.

The objective now is to deduce the joint probability density function of the real and imaginary parts of the electric field amplitude A, from their respective statistical moments. The real and imaginary parts of the complex amplitude, A_r and A_i, are given by:

$$\begin{aligned} A_r &= \mathrm{Re}\{A\} = \frac{1}{\sqrt{N}} \sum_{k=1}^{N} |a_k| \cos\theta \\ A_i &= \mathrm{Im}\{A\} = \frac{1}{\sqrt{N}} \sum_{k=1}^{N} |a_k| \sin\theta \ . \end{aligned} \tag{2.5}$$

The expected values of the real and imaginary components of the complex electric field magnitude, $\langle A_i \rangle$ and $\langle A_r \rangle$, averaged over an ensemble of points are given by:

$$\begin{aligned} \langle A_r \rangle &= \frac{1}{\sqrt{N}} \sum_{k=1}^{N} \langle |a_k| \cos\theta_k \rangle = \frac{1}{\sqrt{N}} \sum_{k=1}^{N} \langle |a_k| \rangle \langle \cos\theta_k \rangle = 0 \\ \langle A_i \rangle &= \frac{1}{\sqrt{N}} \sum_{k=1}^{N} \langle |a_k| \sin\theta_k \rangle = \frac{1}{\sqrt{N}} \sum_{k=1}^{N} \langle |a_k| \rangle \langle \sin\theta_k \rangle = 0 \quad , \end{aligned} \tag{2.6}$$

since:

a) under assumption (2), the expected value of the product of two independent quantities (phase and magnitude) is equal to the product of the expected values.

b) under assumption (3), the expected values of the sin or cos functions over the $[-\pi, \pi]$ interval are equal to 0.

Similarly, it can be shown that the second order moments are given by the following expressions:

$$\begin{aligned} \langle A_r^2 \rangle &= \frac{1}{N} \sum_{k=1}^{N} \sum_{m=1}^{N} \langle |a_k| \cos\theta_k \rangle \langle |a_m| \cos\theta_m \rangle = \frac{1}{2N} \sum_{k=1}^{N} \langle |a_k|^2 \rangle \\ \langle A_i^2 \rangle &= \frac{1}{N} \sum_{k=1}^{N} \sum_{m=1}^{N} \langle |a_k| \sin\theta_k \rangle \langle |a_m| \sin\theta_m \rangle = \frac{1}{2N} \sum_{k=1}^{N} \langle |a_k|^2 \rangle \\ \langle A_r A_i \rangle &= \frac{1}{N} \sum_{k=1}^{N} \sum_{m=1}^{N} \langle |a_k| \cos\theta_k \rangle \langle |a_m| \sin\theta_m \rangle = 0 \quad . \end{aligned} \tag{2.7}$$

Hence the real and imaginary components of the complex amplitude have zero mean, identical variances, and are uncorrelated. Furthermore, from assumption (1) we know that both are made up of the sum of a very large number (N) of statistically independent contributions. From the central limit theorem (Frieden, 1991), it follows that A_r and A_i are both asymptotically Gaussian. Therefore, since A_r and A_i are Gaussian and uncorrelated, their joint probability density function is a simple product of two Gaussian marginal densities:

$$P_{r,i}(A_r, A_i) = \frac{1}{2\pi\sigma^2} e^{\left\{-\frac{A_r^2 + A_i^2}{2\sigma^2}\right\}}, \tag{2.8}$$

where:

$$\sigma^2 = \lim_{N\to\infty} \frac{1}{2N} \sum_{k=1}^{N} \left\langle |a_k|^2 \right\rangle. \tag{2.9}$$

Having obtained the joint probability density function for the real and imaginary parts of the total electric field amplitude, Equation (2.8) is then inverted to obtain the joint density function for the electric field irradiance I and phase θ. They are related to the complex amplitude components by:

$$\begin{aligned} I &= A_r^2 + A_i^2 \\ \theta &= \tan^{-1} \frac{A_i}{A_r}. \end{aligned} \tag{2.10}$$

It can shown from (2.8) and (2.10), using standard techniques for transformation of random variables (Frieden, 1991), that the corresponding joint probability density function for irradiance I and phase θ is given by:

$$p_{I,\theta}(I, \theta) = \begin{cases} \frac{1}{4\pi\sigma^2} e^{\left(-\frac{I}{2\sigma^2}\right)} & I \geq 0, -\pi \leq \theta \leq \pi \\ 0 & \textit{otherwise.} \end{cases} \tag{2.11}$$

Finally, (2.11) is integrated separately with respect to I and θ to obtain the marginal probability density functions for irradiance $p_I(I)$ and phase $p_\theta(\theta)$:

$$p_I(I) = \begin{cases} \frac{1}{2\sigma^2} e^{\left(-\frac{I}{2\sigma^2}\right)} & I \geq 0 \\ 0 & \text{otherwise,} \end{cases} \tag{2.12}$$

$$p_\theta(\theta) = \begin{cases} \frac{1}{2\pi} & -\pi \leq \theta \leq \pi \\ 0 & \text{otherwise.} \end{cases} \tag{2.13}$$

Hence Equations (2.12) and (2.13) demonstrate that the irradiance of a monochromatic linearly polarized speckle pattern has an exponential probability density function, whilst the phase has a uniform probability density function. Both facts are well known fundamental properties of speckle which have been experimentally confirmed many times.

As the field irradiance I is the only directly observable quantity in a speckle pattern, its statistical properties are investigated further. It can be shown (Goodman, 1975) that the n^{th} moment of the irradiance $\langle I^n \rangle$ is given by:

$$\langle I^n \rangle = n!\left(2\sigma^2\right)^n = n!\langle I \rangle^n. \tag{2.14}$$

Since $\langle I^2 \rangle = 2\langle I \rangle^2$ from (2.14), the *variance* σ_I^2 of the speckle field irradiance is given by:

$$\sigma_I^2 = \langle I^2 \rangle - \langle I \rangle^2 = \langle I \rangle^2. \tag{2.15}$$

Finally, the contrast C is a useful speckle statistical measure of the *development* of the speckle pattern. It is defined as the ratio of the standard deviation of the irradiance to its mean:

$$C = \frac{\sigma_I}{\langle I \rangle}. \tag{2.16}$$

The contrast is related to the physical properties of the material used to generate the speckle pattern. It ranges from a minimum value of zero, when the light field is perfectly specular as in the case of reflections from a perfect mirror for example, to a maximum value of unity when the speckle pattern is "fully developed". From (2.15), it is seen that for a speckle pattern which obeys the six assumptions listed at the beginning of this section, the standard deviation σ_I of the irradiance is equal to its mean value $\langle I \rangle$, and the contrast, C, is equal to 1. Intermediate contrast values occur when the speckle field only partially fulfills the six basic assumptions. The dependence of speckle contrast on material properties is investigated in the next section.

2.2.1.2 Dependence of speckle contrast on material properties

Although the speckle contrast bears no direct quantitative relation to the displacement measurements, it is nevertheless an important factor in the *resolution* of the displacement measurements. Indeed, as explained in later sections, material displacements are estimated from the optical phase of the speckle field, and the speckle contrast is a factor in the achievable resolution in the phase measurements. A material which generates a fully developed speckle pattern will give better phase estimates than a material which generates a low contrast speckle pattern.

It is also interesting to note that probability density models for speckle irradiance and phase given by (2.12) and (2.13) are actually only appropriate under asymptotic conditions. These models are valid only when the speckle contrast is at its maximum, or equivalently when the speckle pattern is "fully developed". Hence because of the relevance of speckle contrast to speckle statistics and the measurement of material displacements, the known dependence of speckle contrast on surface roughness is briefly explored below, to give the reader an idea of the dependence of the contrast on actual material properties.

In the study of surface roughness measurements with speckle, the contrast itself is used as the information carrier, as it bears a direct relation to the size of the surface micro-structures. Goodman (1975) derives a complete theoretical expression for speckle contrast as a function of the standard deviation of the surface height deviation. The intricacies of the relation between speckle contrast and surface roughness is a relatively large subject however that has been investigated by several authors and exceeds the scope of this thesis. Only the most important result which has a direct bearing on this work will be given here.

Note that the speckle contrast will also depend on the volumetric distribution of scatterers throughout a material in the case of transmission speckle. However, this relation does not appear to have been investigated.

An interesting series of experiments which elegantly illustrates the dependence of speckle contrast on surface roughness was reported by Fuji and Asakura (1974). Using ground glass diffusers of different roughness, they demonstrated that the standard deviation of the irradiance in a speckle pattern is directly proportional to the standard deviation of the surface roughness, up to the point of maximum contrast (see Figure 2.2). Below the maximum, the standard deviation of irradiance increases linearly (and the background irradiance correspondingly decreases), as the surface roughness increases, thus increasing the contrast C.

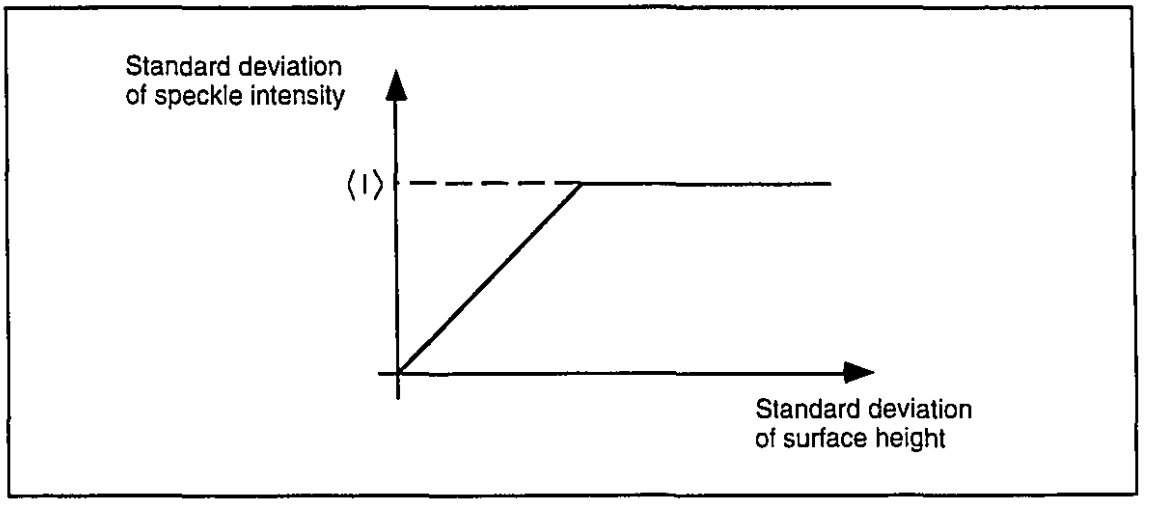

Figure 2.2: Plot of the standard deviation of speckle irradiance versus the standard deviation of surface roughness.

When the standard deviation of irradiance reaches its maximum at the mean value $\langle I \rangle$, the curve "saturates" and the contrast remains constant even for greater surface roughness. Similarly, the probability density function for irradiance goes from a quasi-Gaussian when the contrast is low to a negative exponential as in (2.12) when the contrast is at its maximum. The physical mechanism behind this behavior is the following: the maximum contrast is achieved when the average height of the surface micro-structures exceeds the wavelength of the incident light. This ensures that the phase of the scattered wavelets is uniformly distributed in the $[-\pi, \pi]$ interval and hence fulfills assumption (3)

stated earlier. Any surface roughness increase beyond this point will not serve to further "randomize" the phase distribution.

It is reasonable to speculate that the same behavior occurs with a speckle pattern generated in transmission by index of refraction inhomogeneities. When the scatterers within the material uniformly randomize the phase of the incident light in the $[-\pi, \pi]$ interval, a fully developed speckle pattern will result. In the event that the contrast is low in a transmission speckle system, the material surface can be "roughed up" to increase the contrast and thereby increase the displacement measurement resolution. This is in fact a frequent practice in standard reflection-type speckle interferometers used for studying polished metals for example, where special coatings such as matte white paint are used.

As explained in the Chapter 1, the material under investigation in this application was a biological membrane, more specifically pericardium. Contrast measurements from a speckle pattern generated by the passage of laser light through a canine pericardium membrane yielded a value of approximately 0.8, which is sufficient for good quality phase measurements. The uncertainty on this result however is rather high because of the low dynamic range in the irradiance measurements, due to the limited resolution of the analog-to-digital converters in the frame grabber board, as explained in the next chapter.

2.2.2 Second order speckle statistical properties

In this section, second order statistics are used to derive the average *speckle size*. This is a measure of the two dimensional spatial structure of speckle irradiance or "coarseness" of the overall pattern, at a particular observation plane in space. The speckle size is a particularly important statistic as it must be intimately matched to the characteristics of the system used to view the speckle field, in order to maximize the measurement resolution. In a speckle pattern, a small circular area element which has a diameter equal to the speckle size is often referred to simply as "a speckle".

Speckles can be either "objective" or "subjective", depending on the method used to view the field. It is shown below that the spatial structure of the irradiance differs in both cases. As before, the derivations in this section assume that the diffusing medium generates a speckle field which obeys the six assumptions listed at the beginning of this chapter.

2.2.2.1 Objective speckle size

This section describes the statistics of a speckle field viewed without imaging optics at an observation plane in space in the far field, as shown in Figure 2.3. In the Figure, the speckle field is formed by the passage of a temporally coherent wave through a diffuser at $\boldsymbol{r}$, and the field is viewed at an observation plane at $\boldsymbol{r}'$, at a distance z from the diffuser.

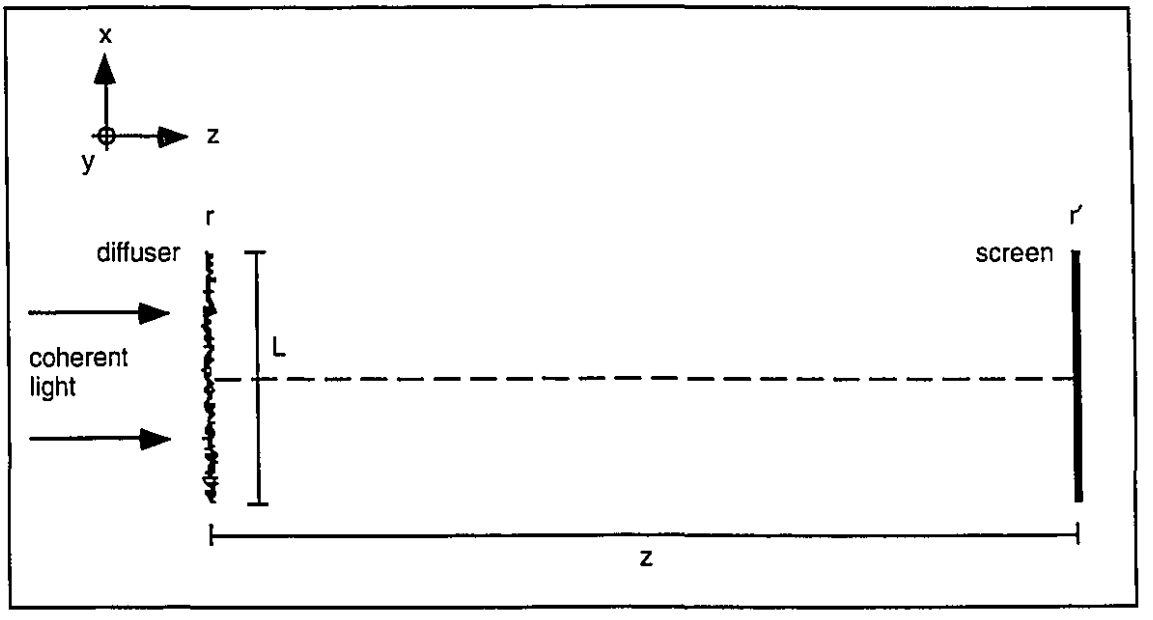

Figure 2.3: Objective speckle pattern formed by the passage of coherent light through an $L \times L$ square area of a diffusing medium at $\boldsymbol{r}$, with index of refraction inhomogeneities and/or optically rough surfaces, observed at $\boldsymbol{r}'$.

It can be shown (Goodman, 1975) that if an $L \times L$ square area is illuminated on the diffuser, the autocorrelation function $R(\Delta x, \Delta y)$ of the irradiance in the xy plane at $\boldsymbol{r}'$, is given by:

$$R(\Delta x, \Delta y) = \langle I \rangle^2 \left[1 + \operatorname{sinc}^2\left(\frac{L\Delta x}{\lambda z} \right) \operatorname{sinc}^2\left(\frac{L\Delta y}{\lambda z} \right) \right], \tag{2.17}$$

where Δx and Δy are lags in the x and y directions, $\langle I \rangle$ is the mean irradiance, z is the distance to the observation plane, and λ is the wavelength of the light in the medium.

The average speckle size d_o is a measure of the "decorrelation distance" between any two points in the speckle pattern and is defined specifically in this case as the distance between the first zeros of the sinc function in (2.17), where:

$$d_o = \frac{\lambda z}{L}. \tag{2.18}$$

It can be seen from (2.18) that the objective speckle size d_o is proportional both to the wavelength of the light and to the distance between the diffuser and the observation plane. Furthermore, the speckle size is inversely proportional to the width of the illuminated area on the diffuser. This type of speckle is termed "objective" because the speckle size depends only on the diffusing area and the distance to the viewing plane, but not on the imaging system used to view the field.

2.2.2.2 Subjective speckle size

When the interference pattern is viewed through an imaging system, as shown in Figure 2.4, the speckles are termed "subjective", because their size depends only on the characteristics of the imaging system. In the figure, the speckle field is formed by the passage of a coherent wave through a diffuser at $\boldsymbol{r}$ at a distance s_O from the imaging lens. The resulting speckle field is viewed at $\boldsymbol{r}'$ in the image plane of the lens, at a distance s_i from the lens.

Goodman (1975) has derived an expression for the autocorrelation function $R(\Delta x, \Delta y)$ of the light irradiance in the xy plane at $\boldsymbol{r}'$:

$$R(\Delta x, \Delta y) = \langle I \rangle^2 \left[1 + \left| 2 \frac{J_1\left(\frac{2\pi a r}{\lambda s_i}\right)}{\left(\frac{2\pi a r}{\lambda s_i}\right)} \right|^2 \right], \tag{2.19}$$

where $\langle I \rangle$ is the mean value of the irradiance, J_1 is a Bessel function of the first kind, a is the radius of the lens, and $r = (\Delta x^2 + \Delta y^2)^{1/2}$ is the magnitude of the lag in the radial direction.

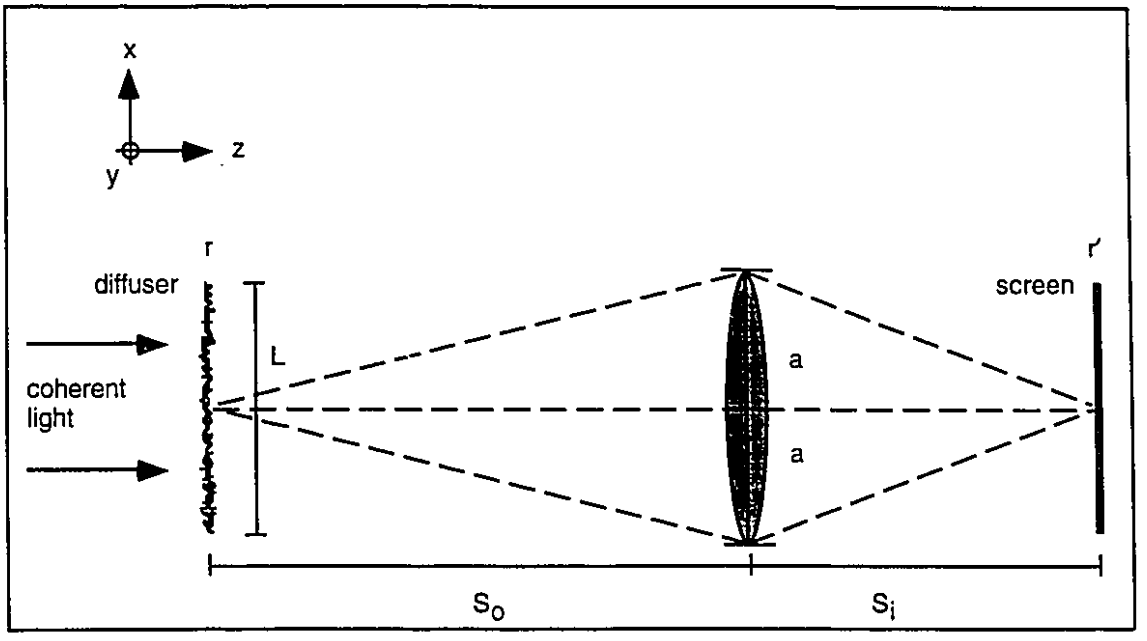

Figure 2.4: Subjective speckle pattern formed by the passage of coherent light through a diffusing medium at r, with index of refraction inhomogeneities and/or optically rough surfaces, observed with an imaging system in the image plane of the lens at r'.

As before, the average speckle size d_s is a measure of the "decorrelation distance" between any two points in the speckle pattern is defined specifically in this case as the separation of the first two minima of the Bessel function in (2.19), where:

$$d_s = \frac{1.22\lambda s_i}{a}. \tag{2.20}$$

It can be seen from (2.20) that the subjective speckle size is simply the diameter of the Airy disk or the diffraction limit of the optical system, and hence depends only on the characteristics of the imaging system itself. Therefore, each individual speckle is generated by a material element of surface area ΔA, where the diameter of ΔA is equal to d_s/M, and M is the magnification of the imaging system. A typical subjective speckle size is around 25 μm.

2.3 Speckle interferometry

Speckle metrology-based techniques used for displacement measurements can be loosely classified into two categories: (i) speckle photography, and (ii) speckle

interferometry. Two major factors distinguish the two categories: displacement sensitivity, and the absence or presence of interference with a reference wave or with a second speckle pattern. Excellent reviews of speckle metrology can be found in textbooks by Dainty (1975), Erf (1978), and Jones & Wykes (1989), as well as in papers by Ennos (1978), and Pryputniewicz (1985). As the experimental technique described in this thesis is based on speckle interferometry, the subject of speckle photography exceeds the scope of this work and is only briefly outlined in the next paragraph for comparison purposes.

In the most common method of speckle photography, the target is illuminated with a single laser beam, and the resulting speckle pattern is recorded on a photographic plate. A second exposure of the same plate is made to record the speckle pattern emanating from the target after it has moved or deformed. The resulting photograph once developed will contain dark and light bands or "fringes". The direction and spacing of the fringes can be made sensitive to in-plane or out-of-plane material displacement magnitude or gradients, depending on the optical configuration. The displacement sensitivity is fairly coarse compared to speckle interferometry and varies from 0.1 mm to 100 mm per fringe.

In the early days of work with speckle photography, it was realized that speckle fields were fully coherent and could thus be used in interference. Leendertz (1970) first demonstrated that two speckle fields could interfere together and yield a third resulting speckle pattern whose irradiance structure was dependent on the phase and irradiance distribution of the two interfering fields. This was the first of many published applications in a field which came to be known as *speckle interferometry*. As will be explained in the following sections, the sensitivity of such techniques to material displacements can be as high as a fraction of the wavelength of the incident light.

Initially, the recording media for speckle interferometers were photographic plates. However, it was soon realized that unlike holography, the high spatial resolution of photographic emulsions was not required and video cameras could be used instead to record the speckle patterns. The first such design was published by Butters and Leendertz (1971). Using their method, images could then be digitized and recorded on magnetic media. In turn, digitization of speckle images allowed access to the vast number of available digital image processing tools, and the field came to be known as *digital holography*, *TV holography*, or more commonly as *electronic speckle pattern interferometry (ESPI)* (Tyrer, 1986; Bergquist *et al.*, 1986) or as *digital speckle pattern*

interferometry (DSPI). It is on this type of technique (ESPI/DSPI) that the present experimental apparatus is based.

2.3.1 Speckle interferometer configurations

As stated in Chapter 1, speckle interferometers can be made selectively sensitive to different displacement directions. The most common configurations are for "in-plane" displacements and "out-of-plane" displacements. Both configurations are discussed in this section.

As explained earlier, each individual speckle in the pattern results from the sum of a large number of coherent contributions, each with random phase and amplitude. The speckle itself however can be modeled as a single "total" wave with associated "total" phase and amplitude, which are random as well. Thus when a speckle from one field is allowed to interfere coherently with a speckle from another field, the resulting irradiance I can be expressed in a manner similar to the interference equation for two waves, of Michelson interferometer fame:

$$I = I_b + I_m \cos(\theta + \Delta\theta), \tag{2.21}$$

where I_b and I_m are respectively the random background and "modulation" components of the irradiance, θ is the fixed random phase difference between the speckles due to the material scattering structure, and $\Delta\theta$ is the phase difference due to changes in the material behavior.

In speckle interferometry, the phase difference term $\Delta\theta$ can be made sensitive to material displacements. Thus by recovering $\Delta\theta$, pointwise material displacements can be estimated at every speckle, with a corresponding lateral sampling resolution roughly equivalent to the speckle size (i.e.: the resolving power of the imaging system), hence the designation of "full-field" technique. Furthermore, as stated in Chapter 1, one of the great advantages of speckle interferometry over holography is that the system can be made selectively sensitive to either in-plane or out-of-plane displacements.

2.3.1.1 In-plane displacement sensitive configuration

The speckle interferometer shown in Figure 2.5 below was originally proposed by Leendertz (1970) and is sensitive to in-plane displacements only. In this design, a coherent source such as a laser is split into two beams which are directed onto the target at $\boldsymbol{r}$ from equal and opposing angles ϕ from normal incidence. The resulting speckle field is recorded at $\boldsymbol{r}'$ in the image plane of the lens.

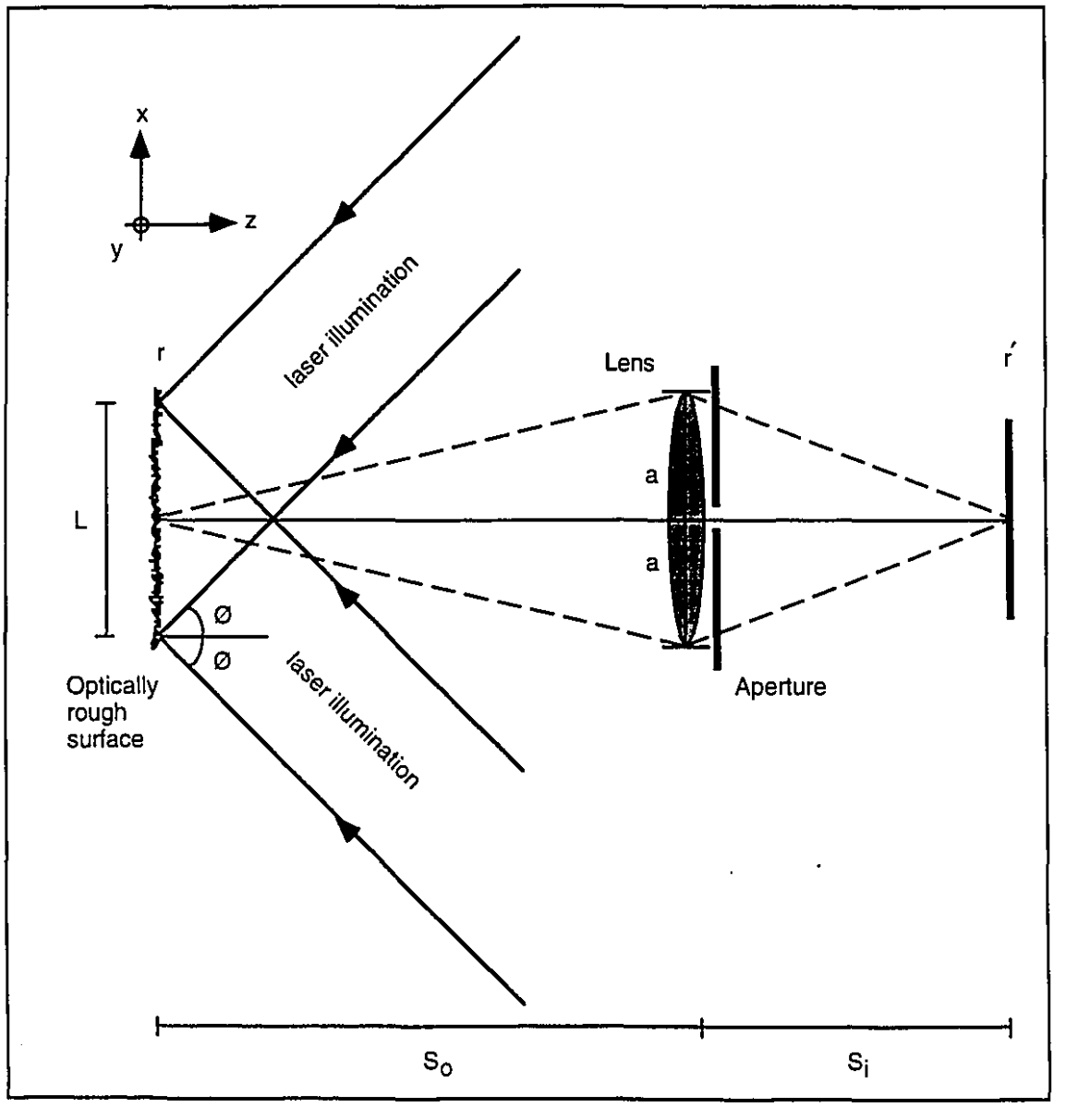

Figure 2.5: Speckle interferometer configuration for measuring in-plane displacements along the x axis only. Design originally proposed by Leendertz (1970).

When the speckle size is adjusted via the aperture (see Equation 2.20) to match the detector array cell size at r', each detector element samples the irradiance of a single speckle. If a material element of surface area ΔA moves in either the y or z directions, the two interfering beams impinging on ΔA will suffer an equal path length change and the resulting speckle irradiance given by (2.21) will not change. If ΔA moves in the x direction by a distance d_x, the path traveled by one of the incident waves will *increase* by $d_x \sin\phi$, and the second incident wave will suffer an identical path length *decrease*. In this case, the optical phase change $\Delta\theta$ in (2.21) will be given by (Jones and Wykes, 1989):

$$\Delta\theta = \left(\frac{2\pi}{\lambda}\right) 2d_x \sin\phi = \frac{4\pi}{\lambda} d_x \sin\phi. \tag{2.22}$$

Hence in this manner, pointwise in-plane material displacements are encoded in the phase of the corresponding individual speckles. Similarly, when the illumination is incident on the sample in the yz plane, as opposed to the xz plane, the interferometer is sensitive to y displacements only.

The success of the mapping process between material displacements and optical phase change $\Delta\theta$ relies on two critical facts. First, the area ΔA which generates a single speckle must contain a large number of individual scatterers. Second, if the material element ΔA displaces by an amount d, then d must be much smaller than the diameter of ΔA. When both conditions are fulfilled, the terms I_b, I_m, and θ in (2.21) will change very little for a displacement d, whereas the phase difference term $\Delta\theta$ will undergo relatively large changes given by (2.22).

The effect of the relative sizes of the displacement d and the size of the material element ΔA is expressed by the visibility factor γ. Equation (2.21) is actually a over-simplification of the true interference process which should normally also include the visibility factor γ (Butters *et al.*, 1978):

$$I = I_b + \gamma I_m \cos(\theta + \Delta\theta). \tag{2.23}$$

In practice, as the displacement distance d approaches the size of the material element ΔA, changes in the terms I_b, I_m, and θ in (2.21) are no longer negligible and can not be decoupled from the true optical phase change $\Delta\theta$. In effect, the speckle irradiances

before and after displacement become *decorrelated* (Owner-Petersen, 1991). This phenomenon is quantified by the visibility factor γ, which acts as a scaling factor on the modulation term I_m. The dependence of the visibility on the displacement magnitude d is shown in the plot of Figure 2.6. When d is much smaller than the diameter of ΔA, the visibility is close to 1 and the speckle modulation is high. Alternatively, when d is close to the diameter of ΔA, the visibility is near zero and the speckle modulation is low. This is referred to as *speckle decorrelation.*

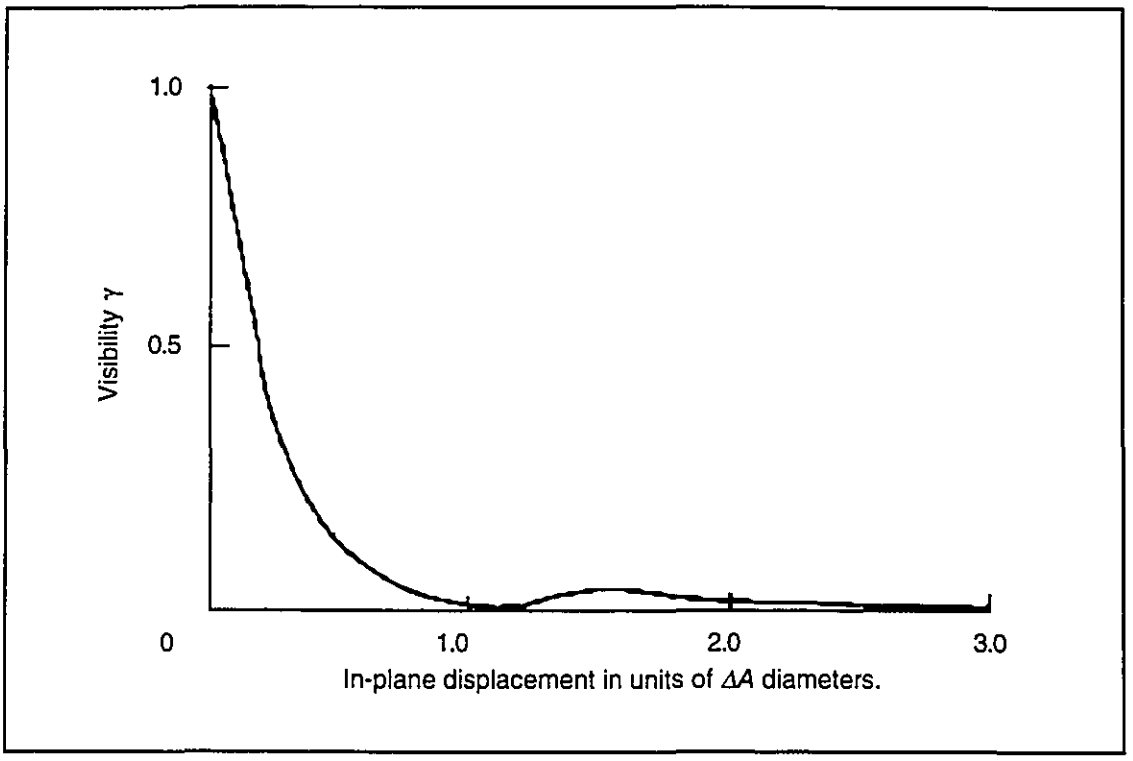

Figure 2.6: Visibility γ as function of in-plane displacement in units of ΔA diameters, where ΔA is the surface area size of a material element which generates a single speckle. Taken from Butters *et al.* (1978).

Note also that the speckle contrast C defined by (2.16) has a similar effect on the scaling of speckle modulation. Indeed, it is an average relative measure of the strength of the irradiance modulation values I_m compared to the background irradiance values I_b in (2.21). Both the properties of speckle contrast (which depends on the material properties) and visibility (which depends on the displacement size) have a direct bearing on the resolution of the phase measurements. Indeed, for a high contrast and high visibility speckle pattern, the modulation I_m will dominate on average over the background irradiance I_b, so that the cosine term in (2.21) will be easily resolved by a detector. If however the

contrast and visibility of the pattern are low, the I_m term will on average only represent a small modulation on the larger background irradiance I_b, and will easily be obscured in noise.

2.3.1.2 Out-of-plane displacement sensitive configuration

For z axis out-of-plane sensitive displacements, a simple Michelson interferometer may be used, with one of the mirrors replaced by the target material. The speckle field is viewed through an imaging system consisting of a lens and an aperture, which focuses the light at an observation plane. This system is not very light efficient however because the reference wave must also go through the aperture controlling the speckle size.

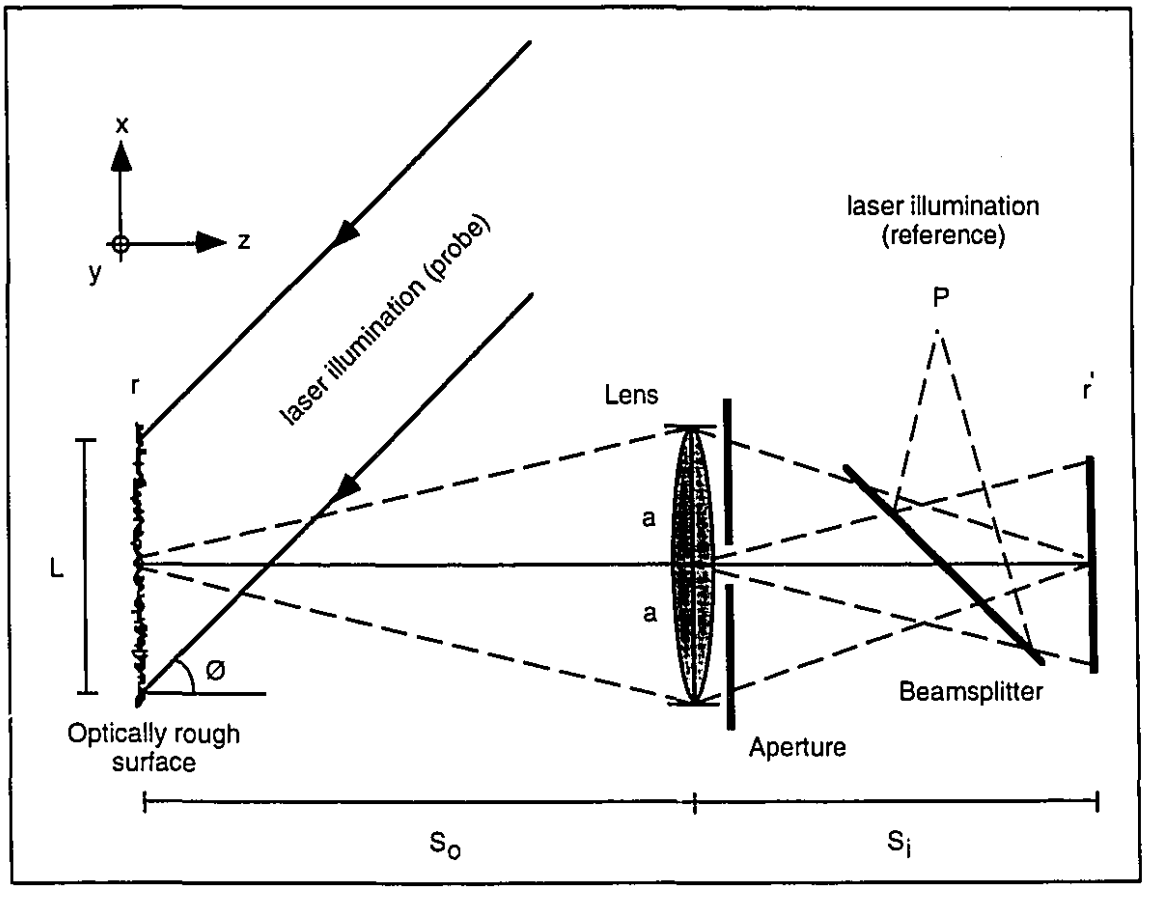

Figure 2.7: Speckle interferometer configuration for measuring out-of-plane displacements along the z axis only.

A better arrangement is shown in Figure 2.7. In this design, a coherent light beam is split into the "probe" and "reference" beams respectively. The probe beam illuminates the target at shallow angle ϕ from the surface normal and the reflected light forms a speckle

pattern. The speckle field is collected by the lens and focused onto the observation plane at $\boldsymbol{r}'$. The reference beam is focused down at point P in such a way that it appears to diverge from the center of the imaging lens. This is required in order to equalize the path lengths to all points in the observation plane. The reference is then photo-mixed with the speckle field by the beamsplitter. An aperture controls the speckle size so that it may be resolved by the imaging device at $\boldsymbol{r}'$, which records the interference pattern between the speckle field and the plane reference wave.

As before, when the speckle size is adjusted via the aperture to match the detector array cell size, each detector element samples the irradiance of a single speckle. If a material element of surface area ΔA moves in the z direction by a distance d_z, the path length for the probe beam will decrease by $d_z cos\phi$ with respect to the reference. If the incidence angle ϕ is sufficiently small, displacements in the x or y directions may be neglected. The speckle irradiance is again be given by (2.21), but where:

$$\Delta\theta = \left(\frac{2\pi}{\lambda}\right) d_z \cos\phi. \tag{2.24}$$

2.3.2 Displacement measurements

The basic technique for extracting in-plane and out-of-plane material displacement information from speckle patterns is a two-step process, as explained in this section. In all cases, a first speckle pattern is recorded with the target in a "reference" state, using either of the above in-plane or out-of-plane configurations. The target is then displaced or deformed, and a second speckle pattern is recorded. The two speckle patterns are then digitally processed to recover the *relative* displacement between the target states. The required processing is a simple subtraction or addition in the case of *correlation* interferometers, or more involved algorithms as in the case of *phase-stepping* interferometers. Note however that in both cases, the displacement measurement is a relative one, with reference to the initial target state.

The mapping between phase and displacement, given either by (2.22) or (2.24), depends on the wavelength of the laser light λ and the geometry of the interferometer. In the images resulting from the digital processing of two speckle patterns, certain distinctive features appear which are known as "*fringes*": dark or light bands in the case of correlation interferometers, or discontinuities in the case of phase-stepping interferometers. The *fringe*

spacing or *fringe sensitivity* corresponds to the specific material displacement distance that causes an exact 2π change in the speckle phase. It is calculated by equating (2.22) and (2.24) to 2π. Hence, the respective fringe spacings for in-plane and out-of-plane sensitive interferometers are given by:

$$d_{x,y} = \frac{\lambda}{2\sin\phi}, \tag{2.25}$$

$$d_z = \frac{\lambda}{\cos\phi}. \tag{2.26}$$

2.3.2.1 Correlation interferometers

When two speckle patterns recorded before and after deformation are digitally subtracted, the resulting image contains dark bands or fringes, which correspond to areas of constant displacement or *maximum correlation*. A typical example is given in Figure 2.8 which shows correlation fringes corresponding to out-of-plane displacements.

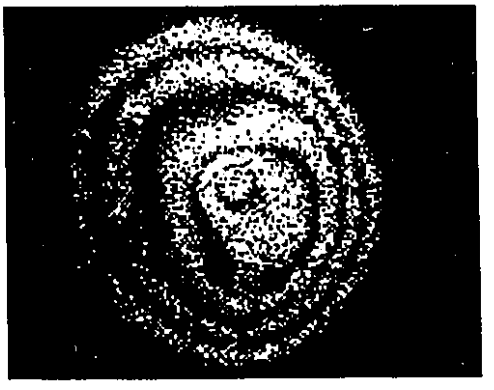

Figure 2.8: Speckle pattern correlation fringes corresponding to out-of-plane displacements, where the fringe sensitivity is 1μm.

The principle behind the formation of the fringes is as follows: consider a material element of surface area ΔA and its associated speckle at the observation plane. As explained above, each such speckle can be considered to behave as an independent Michelson interferometer, modeled by Equation (2.21). When a material element ΔA moves as a result of overall material deformation, the corresponding speckle phase $\Delta\theta$ cycles in the range $[-\pi,\pi]$, according to equations (2.22) or (2.24). In fact, when $\Delta\theta$ changes by an integer multiple of 2π the speckle irradiance will cycle back to its original value. Hence when two speckle images sampled before and after deformation are *subtracted*, any pixels

corresponding to phase changes which are multiples of 2π will be null or black, thus forming dark fringes.

The main problem with correlation interferometers is that they provide information about displacement direction magnitude only, not direction. Indeed, a fringe pattern like the one shown in Figure 2.8 could correspond to a depression, an elevation, a circular wave pattern, or a combination of the above. Hence correlation interferometers are only suited to simple deformation analysis problems where *a priori* information can be used to deduce the direction of displacement.

2.3.2.2 Methods for recovering optical phase

There are several methods available for recovering true phase information from full field interferometry techniques (Reid, 1986; Sirkis, 1992). The main ones are phase-stepping, spatial homodyning (also known as the method of spatial carrier fringes or Fourier transform method), and heterodyne methods. With such techniques, the speckle phase $(\theta + \Delta\theta)$ in the interference term in (2.21) can be calculated at every point in the interference pattern. Since this true phase can have any negative or positive value in the $[-\pi, \pi]$ interval, both the magnitude and direction of displacements can be determined.

2.3.2.2.1 Phase-stepping method

In phase-stepping methods, a number of speckle pattern images of the target in a given state are acquired, while one of the two incident light beams is phase-shifted with respect to the other by known amounts. The resulting images are then processed according to various algorithms (see Table 2.1), to generate a final data set which separately yields the phase $(\theta + \Delta\theta)$ and modulation I_m of the interference term in (2.21) at every point. The advantage of this method is that it yields very accurate estimates of the phase and the measurement confidence increases with the number of images used by the phase-shifting algorithm (Creath, 1985, 1988). The disadvantage of this method is that multiple images of the target in a given state must be acquired. This is not a problem however when the mechanical events under investigation are highly repeatable (as in the study of vibrations) or when the image sampling process is fast compared to the time scale of the material displacements (as in the present application).

2.3.2.2.2 Fourier transform method

The Fourier transform method, originally introduced by Takeda *et al.* (1982) for one dimensional problems and later extended to two dimensional applications by Macy (1983), has been successfully used in holography and Moiré methods for recovering phase information from interference patterns. In this method, the interference pattern is bandpassed filtered in the Fourier domain to remove the background intensity values I_b and the complex inverse Fourier transform of the filtered image yields the phase $(\theta + \Delta\theta)$ and modulation I_m of the interference pattern at every point.

Recently, Preater and Swain (1992, 1994) reported the successful use of the Fourier transform method to recover phase information from speckle interferometry correlation fringes. There is however some doubt concerning the general applicability of this method to speckle interferometry. Furthermore, the Fourier transform method requires fairly severe bandpass filtering (Kreis and Jüptner, 1989). This in effect imposes an upper limit on the number of fringes in any image, in order for the speckle and fringe spatial frequency components to be well separated in the Fourier domain. The great advantage of this method however is that only one image of the target in a given state is required. This is particularly useful for studying transient dynamic events.

2.3.2.2.3 Heterodyne method

Finally, the last of the available procedures for recovering true phase information from full field interference patterns is termed the heterodyne method. In this method, the probe and reference beams have a mutual frequency offset $\Delta\omega$, normally in the upper kHz or lower MHz range. The interference pattern thus becomes a temporally varying signal at frequency $\Delta\omega$, where the material displacements are encoded as a phase modulation. By scanning the interference pattern with a point detector having a sufficient bandwidth and demodulating the resulting signal with a coherent reference, the interference pattern phase at every point can be recovered.

2.3.2.3 Use of the phase-stepping method

In this application, the phase-stepping method was chosen over the Fourier transform method mainly because of its ability to estimate reliably the phase in the presence of high noise levels. Indeed, the volume scattering effect due to the passage of the laser

light *through* the biological material under investigation seemed to greatly hinder the formation of the speckle correlation fringes required by the Fourier transform method. In fact, the correlation fringes were often completely unobservable. In contrast, by using a phase-stepping algorithm with a sufficiently high number of images, good quality results could always be obtained. Heterodyne methods were not considered because of the need for a scanning detector.

In phase-stepping methods, the speckle irradiance I_i at a point in the image at the i^{th} phase step is expressed as:

$$I_i = I_b + I_m \cos(\theta + \Delta\theta + \alpha_i), \tag{2.27}$$

where α_i is the relative phase shift between the two light beams at the i^{th} phase step. For mathematical convenience in the following derivation, (2.27) is expressed as (2.28) below, with the change of variable given by (2.29):

$$I_i = a_o + a_1 \cos\alpha_i - a_2 \sin\alpha_i, \tag{2.28}$$

where:

$$a_0 = I_b, \quad a_1 = I_m \cos(\theta + \Delta\theta), \quad a_2 = I_m \sin(\theta + \Delta\theta). \tag{2.29}$$

Equation (2.28) is simply a general equation with three unknowns (the a_i). Hence by stepping the phase by three different known amounts, α_i, and recording the irradiance values, I_i, three distinct equations containing the a_i are generated at every point and an exact solution can be found. By varying the phase step α_i over a number, N, of distinct steps, where N is greater than three, an improved estimate of the unknown quantities is obtained. The solution, which is optimal in the least squares sense, is computed at every point by solving the normal equation system $a=A^{-1}B$, where:

$$\underbrace{\begin{bmatrix} N & \sum\cos\alpha_i & -\sum\sin\alpha_i \\ \sum\cos\alpha_i & \sum\cos^2\alpha_i & -\sum\cos\alpha_i\sin\alpha_i \\ -\sum\sin\alpha_i & -\sum\cos\alpha_i\sin\alpha_i & \sum\sin^2\alpha_i \end{bmatrix}}_{A} \underbrace{\begin{bmatrix} a_0 \\ a_1 \\ a_2 \end{bmatrix}}_{a} = \underbrace{\begin{bmatrix} \sum I_i \\ \sum I_i\cos\alpha_i \\ -\sum I_i\sin\alpha_i \end{bmatrix}}_{B}. \tag{2.30}$$

Note that the matrix inverse A^{-1} need be computed only once since it depends solely on the phase steps α_i, which are generally the same at every point in the image.

The speckle phase $(\theta+\Delta\theta)$ and modulation I_m can be calculated using:

$$\theta + \Delta\theta = \tan^{-1}\left(\frac{a_2}{a_1}\right), \tag{2.31}$$

$$I_m = \sqrt{(a_1)^2 + (a_2)^2}. \tag{2.32}$$

When the phase steps α_i are equally distributed across one period as in (2.33) below, the off-diagonal elements in the matrix A become zero. In this case, simplified expressions for the phase and modulation are given by (2.34) and (2.35), which do not require solving the matrix equation:

$$\alpha_i = \frac{2\pi(i-1)}{N}, \quad i = 1...N, \tag{2.33}$$

$$\theta + \Delta\theta = \tan^{-1}\left\{\frac{\sum_{i=1}^{N} I_i \sin\alpha_i}{\sum_{i=1}^{N} I_i \cos\alpha_i}\right\}, \tag{2.34}$$

$$I_m = \sqrt{\left(\sum_{i=1}^{N} I_i \sin\alpha_i\right)^2 + \left(\sum_{i=1}^{N} I_i \cos\alpha_i\right)^2}. \tag{2.35}$$

According to Creath (1985), a well calibrated phase-stepping system which digitizes the speckle irradiance to 8 bits of resolution, can be expected to have a phase noise standard deviation of about $\lambda/100$. As in most interferometry techniques, the recovered phase is "wrapped" in the $[-\pi,\pi]$ interval. In order for the absolute magnitude of displacements to be determined, the phase must first be "unwrapped" to $[-\infty,+\infty]$. This topic is explored in Chapter 5.

N	Algorithm	Authors / Comments
a: 2	$\tan^{-1}\left\{\frac{I_2}{I_1}\right\}$	Santoyo *et al.* (1988); Kerr *et al.* (1990). With a $\pi/2$ phase offset in the reference, the sin and cos of the unknown angle are obtained and the unknown amplitude is divided out.
b: 3	$\tan^{-1}\left\{\frac{\sqrt{3}(I_2 - I_3)}{(2I_1 - I_2 - I_3)}\right\}$	General least squares solution with equal phase steps of $2\pi/3$.
c: 3	$\tan^{-1}\left\{\frac{I_3 - I_2}{I_1 - I_2}\right\}$	Wyant *et al.* (1984). Equal phase steps of $\pi/2$.
d: 3	See reference	Vikram *et al.* (1993) This method uses two steps of equal but unknown phase α.
e: 4	$\tan^{-1}\left\{\frac{I_4 - I_2}{I_1 - I_3}\right\}$	General least squares solution with phase steps of $\pi/2$. A very common algorithm.
f: 4	$\tan^{-1}\left\{\frac{3I_2 - (I_1 + I_3 + I_4)}{(I_1 + I_2 + I_4) - 3I_3}\right\}$	Schwider *et al.* (1993) The algorithm is in fact an average of two staggered 3 step method measurements.
g: 4	$\tan^{-1}\left\{\frac{\sqrt{(I_1 - I_4 + I_2 - I_3)(3I_2 - 3I_3 - I_1 + I_4)}}{(I_2 + I_3 - I_1 - I_4)}\right\}$	Carré (1966) The original phase-stepping algorithm. It uses 4 phase steps of unknown but equal phase.
h: 5	$\tan^{-1}\left\{\frac{2(I_2 - I_4)}{2I_3 - I_5 - I_1}\right\}$	Hariharan *et al.* (1987) This algorithm is the most common in commercial interferometers, with phase steps of $\pi/2$. It reduces certain numerical errors inherent to 4 step methods.
i: 7	$\tan^{-1}\left\{\frac{\sqrt{3}(I_2 + I_3 - I_5 - I_6) + (I_7 - I_1)/\sqrt{3}}{(-I_1 - I_2 + I_3 + 2I_4 + I_5 - I_6 - I_7)}\right\}$	Larkin and Oreb (1992) This method is applicable to non-sinusoidal waveforms, such as when higher order harmonics are introduced by detector non-linearity.
j: N	See reference	Surrel (1993) This is a generalization to N steps of a formulation which uses averaging with N samples to add robustness to the standard N-1 formulation. This algorithm is identical to the 5 step method for N=5.

Table 2.1: Phase-stepping algorithms.

There are a number of available phase-stepping algorithms in the literature, which require varying numbers of phase steps (see Table 2.1). The general trade-off is that of parsimony of data and speed of acquisition, versus better signal-to-noise ratio (SNR) and greater immunity to systematic errors. Furthermore, some methods require phase steps of known magnitude, whereas others merely require the steps to be equal, but of unknown magnitude (cf. the Carré algorithm, Table 2.1.g). Such methods are useful when a diverging beam illuminates the target. In this case, the phase step α_i changes across the extent of the target but remains constant at each point.

Excellent reviews of basic phase-stepping principles and error analysis can be found in Creath (1985, 1988) (with emphasis on decorrelation errors due to object tilt and finite detector area), Kerr and Tyrer (1987), Schmit and Creath (1992) (with emphasis on errors due to phase-shifter miscalibrations and detector non-linearities), and in Larkin and Oreb (1992) (with emphasis on propagation of errors due to properties of the arctan function).

The phase-stepping algorithm selected for this application was the general least squares formulation using four equi-spaced steps of $\pi/2$ (see Table 2.1.e). It was found that four images gave the optimal balance between parsimony and noise reduction, i.e.: 3-steps methods gave poor results and 5-steps methods gave only minor improvements which did not justify the storage and acquisition of a fifth image. Of the 4-step methods, the general least squares formulation was chosen because of its simplicity and corresponding ease of theoretical noise analysis. Again, this method was compared to other 4-step methods and was found to perform equally well to within the experimental error.

In actual experimental setups, various methods of changing the optical phase in the reference beam have been used. The most common method involves mounting a mirror on a piezo-electric actuator (Maas and Vrooman, 1989). Other methods such as rotating a polarizer in one beam path (Wyant *et al.*, 1978), and using strain induced phase changes in optical fibers (Joenathan, 1991) have also been used. In this application, a rotating glass window was used to vary the optical phase in one of the two interferometer arms, as explained in the next chapter.

Chapter 3

Experimental Setup and Data Acquisition

This chapter describes in detail the design and construction of the experimental apparatus. The design is modular and hence each apparatus subsystem is described separately. The unique design features which distinguish the system from common methods of materials testing are highlighted.

3.1 Experimental apparatus : General overview

As explained in Chapter 1, the goal for this project was to design and build a system capable of performing mechanical testing of biological membranes, in order to identify the underlying nature and spatial distribution of their material properties. Because of the special nature of such materials, it was shown that existing techniques were either inappropriate or incomplete, and so a new method was devised. In this method, an experimental apparatus (described in this Chapter) is used to acquire experimental data which is then analyzed in two stages, as explained in Chapters 5 and 6.

The apparatus, shown in block diagram form in Figures 3.1 to 3.5, can be divided into four main subsystems: the optical subsystem (see Section 3.2), the mechanical subsystem (see Section 3.3), the data acquisition and control hardware subsystem (see Section 3.4), and the data acquisition and control software subsystem (see Section 3.5). The apparatus was specially designed to meet the challenging needs of mechanical testing of thin compliant biological membranes, which are known to have material properties which are non-linear, anisotropic and inhomogeneous. As such, special experimental design features distinguish this apparatus from most others in the literature, and they are listed in this section.

The vast majority of speckle interferometer designs operate with light *reflected* from a material surface. However, most biological membranes are translucent (e.g. pericardium, pleura, etc.) or even highly transparent (e.g. cornea), hence they reflect very little light. Therefore, an unusual feature of this apparatus which sets it apart from common designs is that it operates in *transmission*, rather than in reflection. Indeed, for a thin translucent target material, a transmission setup is much more light efficient. In this operation mode, the speckles originate from scattering both by the surface micro-structures and by the material index of refraction inhomogeneities.

The underlying assumption in using changes in the speckle field to deduce planar displacements of the target membrane, is that the membrane thickness is small compared to its surface area. In this case, changes to the speckle field are attributed mainly to material displacements in the plane of the membrane and effects due to material displacement gradients in the normal direction are negligible. Results of the experimental verification of this assumption are presented in the next chapter.

A second important aspect of this design is that the material under test is a living biological tissue, which requires special conditions during experiments. Indeed, the membrane under investigation must be mounted in a sample chamber or "bath" filled with physiological saline solution to keep it in a healthy state. Furthermore, the solution must be kept at a constant temperature for the duration of the experiment. The laser light thus propagates through four different media: air, glass, saline solution, and the biological membrane itself.

A third important design aspect pertains to the method of separately acquiring the two orthogonal components of in-plane displacements. Because of the optically inhomogeneous nature of the target material, the speckle fields generated by the passage of polarized light through the membrane are themselves partially depolarized. Hence the two speckle fields corresponding to the planar displacement components cannot be physically separated by polarization, as in the design by Mendoza Santoyo *et al* (1990). Because of this and the fact that a single wavelength source is used, the displacement components must be acquired sequentially in time, rather than simultaneously. In order to achieve this, two light delivery systems which partly co-propagate along a common path are used to illuminate the target in orthogonal planes of incidence. Only one of the two delivery systems is active at any one time.

The apparatus is laid out three dimensionally in two levels: the optics are mounted on a optical table at the bottom level, and the mechanical perturbation actuators and sample chamber are mounted on a square plate above the table surface. The entire setup is enclosed in a custom built environmental isolation enclosure (Brenan *et al.*, 1992), which minimizes thermal, acoustic, and electromagnetic noise from the surrounding laboratory environment. The enclosure is built around a wooden frame which is covered with lead and copper sheets, for low frequency acoustic and electromagnetic noise insulation respectively. The inside of the enclosure is lined with fiberglass panels for medium to high frequency acoustic damping. The enclosure is raised and lowered on pneumatic pistons and rests on an aluminum square tubing manifold, which provides feedthrough connections for electrical cabling and tubing.

Three photographs of the experimental apparatus are given in Plates I, II, and III at the end of this Chapter. The photographs show three views of the apparatus on the optical table and the neighboring workstation and instrumentation rack.

3.2 Optical subsystem

The optical subsystem design (see Figures 3.1 and 3.2) is based on the method of speckle pattern interferometry for in-plane displacement measurements, more specifically on the original design by Leendertz (1970). This classic system, shown in Figure 2.5, is still the most common design today for this type of measurement. As opposed to the original Leendertz design however, the speckle patterns are recorded by a video camera, as in the family of ESPI/DSPI techniques. However, since the system operates in transmission, the speckle pattern is collected by the camera from the opposite side of the target (see Figure 3.2).

As shown in the diagram of the optical layout (Figure 3.1), the coherent source for the apparatus is a 10 mW He-Ne laser (red, $\lambda = 632.8$ nm, Melles-Griot model 05LHP991), linearly polarized in the plane of the optical table. The light from the laser passes through a custom built digitally controlled shutter and is directed by mirror M1 through a digitally controlled *liquid crystal retarder* (LCR) (Meadowlark Optics cell and digital controller model D1040) and into a custom beam expander (microscope objective MO and lens L). The non-polarizing beamsplitter BS1 deflects 50% of the light into the phase-shifted arm of the interferometer to mirror M2, and passes the other 50% of the light

into the unshifted arm of the interferometer to mirror M7. The polarizing beamsplitters PBS1 and PBS2 selectively direct the laser light either to the e_1e_3 plane with the M4/M5 mirror pair, or to the e_2e_3 plane with the M3/M6 mirror pair, depending on the light polarization state. Note that all optics were purchased from Melles-Griot and all non-custom mounts are Mini Series mounts purchased from Newport Corporation.

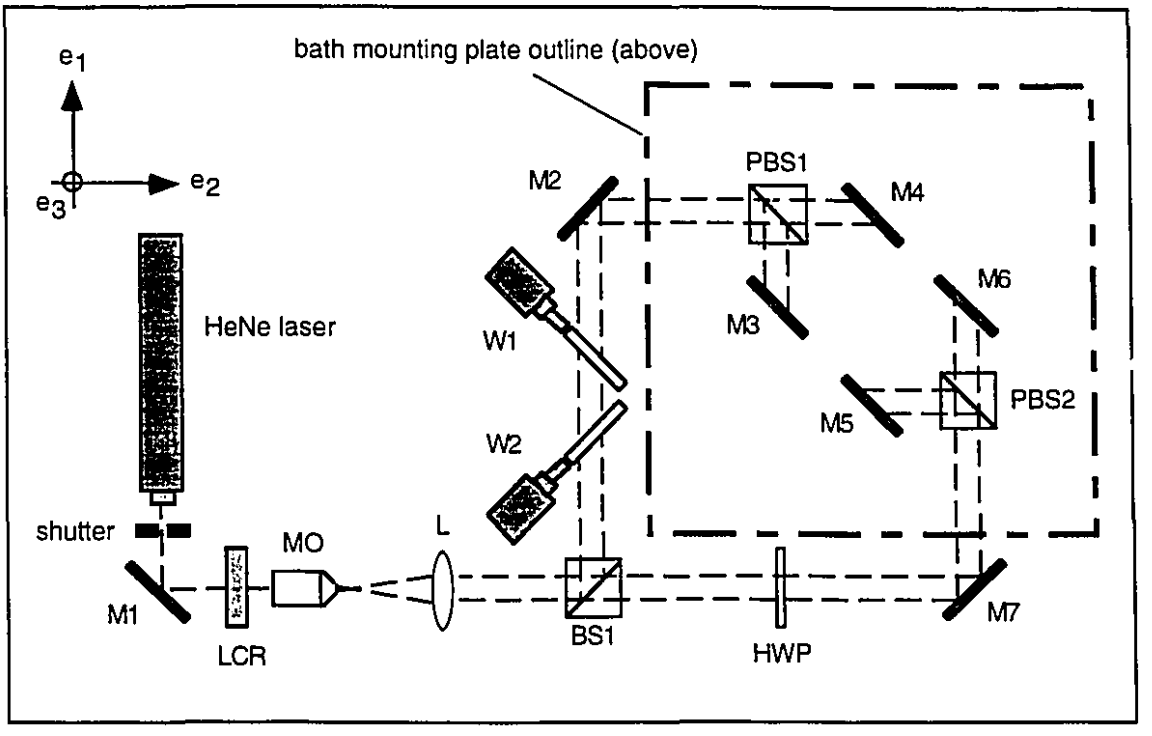

Figure 3.1: Top view of the apparatus optics layout on the optical table, below the bath mounting plate.

The digitally controlled LCR is used to toggle between two birefringent states of phase retardation difference: zero and one half wave retardations. The LCR thus acts as a half wave plate that can be switched on and off digitally. By orientating the fast and slow axes of the LCR at 45° from the plane of the optical table, the laser light polarization axis can be flipped between the *S* state (parallel to the table) and the *P* state (normal to the table). Hence the computer, via the LCR, selects either one of the light delivery systems for the e_1e_3 plane (M4/M5) or for the e_2e_3 plane (M3/M6), to transmit the laser light to the membrane above. The fixed half wave plate HWP, which also has its fast and slow axes oriented at 45° from the plane of the optical table, ensures that M4 is paired with M5 and that M3 is paired with M6.

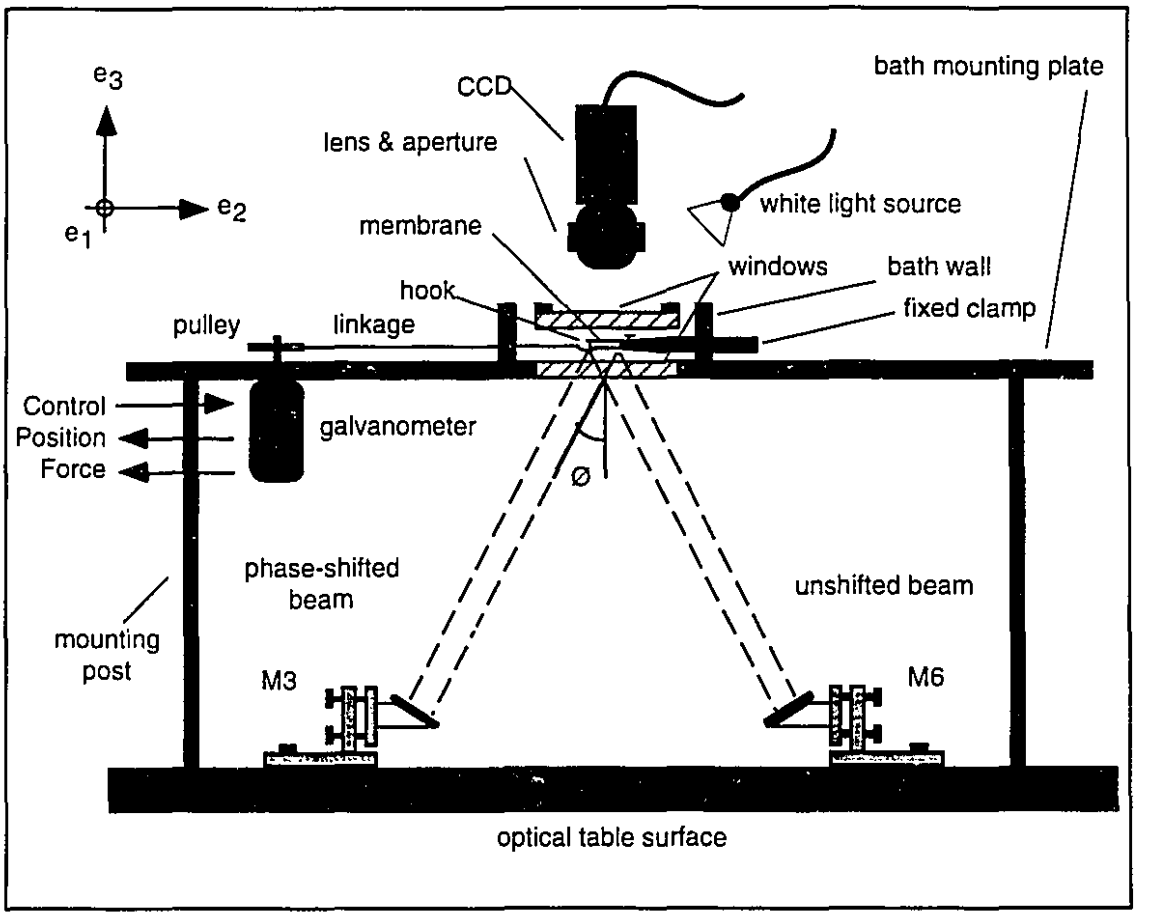

Figure 3.2: Side view of the apparatus on the optical table showing both the optical and mechanical layouts.

Phase shifting of the light in one of the two arms of the interferometer is achieved by custom built computer controller phase shifters consisting of two optical grade circular glass windows W1 and W2 which are counter-rotated in the light path. Two windows are required to cancel the lateral shift introduced by the changing optical beam deflection on rotation. The windows are mounted on precision rotary electromagnetic actuators (galvanometers) (General Scanning model G350DT).

As stated above, a single laser beam pair is directed at any one time from the optical table to the membrane above, where the two beams in a pair are incident at equal and opposing angles ϕ from the surface normal. In the apparatus, the angle of incidence ϕ was nominally 19.3°, which corresponds to a fringe sensitivity of 0.96 μm/fringe for in-plane displacements (see Equation 2.25). The biological membrane is held in a bath which has anti-reflection coated glass windows at the top and bottom surfaces. The bath is mounted

on a 400 mm × 400 mm square 20 mm thick plate, which sits approximately 300 mm above the optical table surface atop mounting posts. The bath is filled with saline solution (0.85% NaCl).

The light from both beams passes through both the membrane and saline solution, and generates a speckle field which is recorded by the CCD array camera (Panasonic model GP-MF552) mounted above the bath. A CCD based video camera was chosen as the imaging device because of its sensitivity in the red region of the spectrum and the linearity of its response (Joenathan, 1990). This particular CCD was selected because of its high sensitivity (minimum illumination of 0.79 mW/m^2, at 555 nm), high dynamic range (59 dB signal to noise ratio), and relatively high pixel count (768H×493V). The light sensing element size is 6.5 μm × 5.5 μm and the center-to-center pixel spacing is 13.0 μm horizontally and 11.0 μm vertically. A 25 mm focal length lens with integrated aperture focuses the speckle pattern onto the camera sensor and allows independent adjustment of the speckle size. The speckle images recorded by the camera are digitized by a 640×480×16 frame grabber board (IBM VCAA Video Capture Adapter).

The CCD device used in this apparatus is a "gray level" camera which records an integrated measure of light irradiance across the entire visible spectrum (and beyond) at each pixel. The frame grabber board however is an RGB color device. It thus processes the analog signal from the CCD array as a color signal where all three primary colors have equal values. The video input is digitized by three A/Ds and the result is packed into a 16 bit word, where the bit distribution is either 6 red, 6 green, and 4 blue (664 mode), or 5 red, 6 green, and 5 blue (565 mode). In order to maximize the number of bits per sample, either the green value or the red value in the 664 mode should be used. It was found that the red A/D had a lower noise level than the green A/D, so the 6 red bits in 664 mode were used.

Finally, an incoherent white light source is also included in the setup to take images of the membrane under normal light, for such tasks as tracking markers and membrane hook positions. The custom digitally controlled shutter (see Figure 3.1) blocks the laser light when the computer activates the white light source.

3.3 Mechanical subsystem

As stated in Chapter 1, the apparatus must be able to apply an arbitrary state of plane stress to the membrane under test. This is achieved by using a number of actuators arrayed circularly around the membrane, each pulling independently. Furthermore, a relatively large number of actuators is desirable in order to minimize "edge effects" or high stress concentrations at the tether points. The apparatus described here has 16 computer controlled actuators equally spaced (22.5°) around the membrane. In the experiments described in this thesis, 3 of these actuators were removed and replaced by a fixed clamp, as shown in Figure 3.3, for reasons explained in Chapter 5.

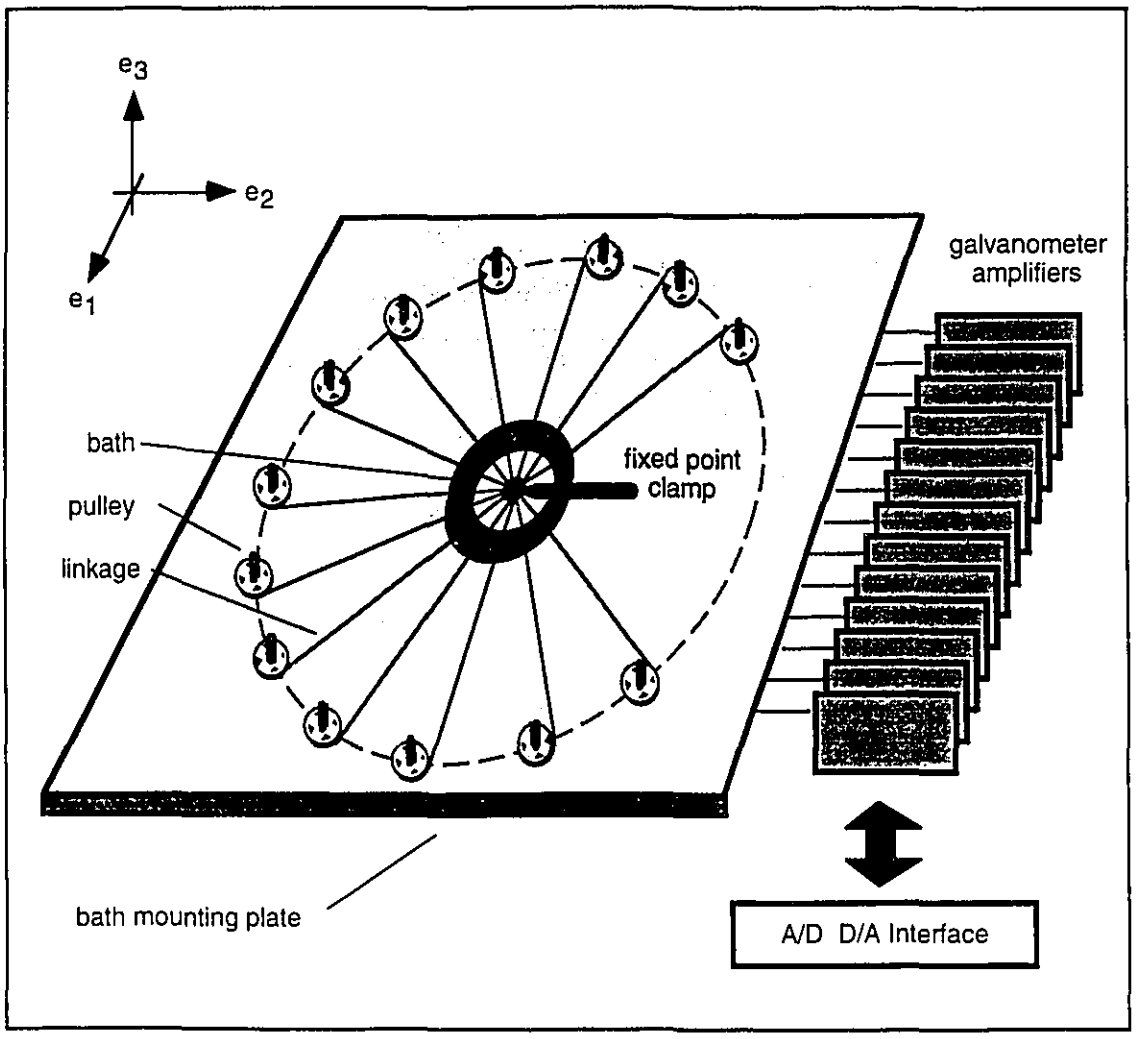

Figure 3.3: Top/side view of the bath mounting plate showing the mechanical perturbation layout with the 13 stretch galvanometers, linkages, fixed clamp, and sample chamber.

The actuators are temperature compensated rotary electromagnetic actuators (galvanometers) (General Scanning model G350DT). The galvanometer shafts have a maximum angular excursion of ±25° and can apply a maximum torque of 0.2 N·m. They are driven by dedicated amplifier/controllers (General Scanning model AE1000) which have a single input voltage command and three output voltages proportional to shaft angle, position acknowledge, and coil current. The motor shaft angle is controlled by an analog PID closed-loop feedback control circuit in the AE1000s. A heat pad attached to the outside of the motor housing (driven by closed-loop temperature control circuitry) keeps the actuator at a nominal operating temperature close to 40 °C, to within 0.5 °C. This is done to reduce the temperature fluctuations which alter the galvanometer current to force relation.

The galvanometers are installed below the bath mounting plate with the shafts protruding above the plate surface. Thin custom pulleys (diameter: 40 mm, thickness: 2 mm) are mounted on the galvo shafts. The galvanometers apply forces to the membrane via linkages which are shown in Figure 3.4. The linkages consists of a short length of fine flexible chain (830C 10 carat gold, 0.2 mm diameter wire, 11.8 links/cm) which wraps around the pulleys at one end and is soldered to 250 µm diameter stainless steel wire at the other end. The stainless steel wires go through thin "vacuum grease"-filled slots in the bath walls. Finally, the wires are connected to small gold plated fish hooks (#12) which tether to the membrane edge. The forces applied by the actuators are determined indirectly by measuring the amplifier voltage outputs proportional to the current through the motor coils.

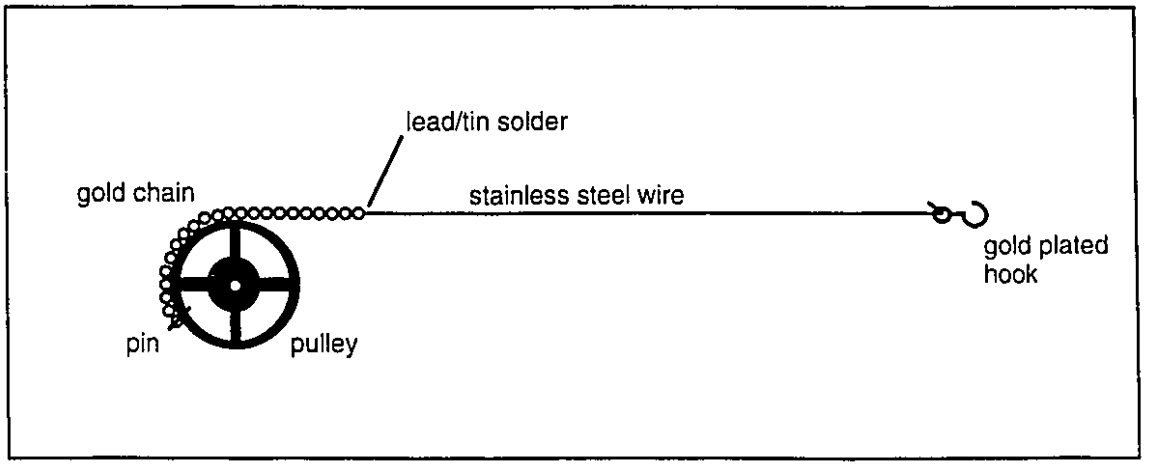

Figure 3.4: Pulling linkages.

Since the speckle interferometry based technique used here measures relative displacements, a fixed point on the sample must be provided as a reference point for absolute measurements. This is achieved by holding the membrane with a triangular shaped clamp at one point (see Figure 3.3), where the fixed reference is defined to be the point at the end of the clamp tip.

The entire mounting plate and bath are held at constant temperature by the controlled heating action of the galvanometer heater pads. A thermocouple inside the bath allows the computer to monitor the membrane temperature throughout the experiment. The mounting plate, bath, and most of the custom machined components were optically black anodized to reduce stray reflected light and to provide a tough surface finish.

3.4 Data acquisition and control hardware subsystem

The entire experiment is controlled in real-time by a workstation (IBM RISC System/6000 model 520). A data flow diagram for control and data acquisition in shown in Figure 3.5. The computer interfaces to external devices via the UNIMA I/O system (Martel *et al*, 1992). The UNIMA system is a real time analog and digital I/O interface system custom built by our group for the IBM RISC System/6000 workstations. The system design is modular and the basic components are 16 channel 20 bit D/A *UDAC* cards, 32 channel 16 bit (18 bits internal, 50 kHz single channel) A/D *EMAP* cards, and 32 bit digital I/O interface cards.

The flow diagram in Figure 3.5 depicts the various external devices used by the workstation during an experiment in the leftmost column, and the workstation bus on the right. The diagram is separated horizontally into three areas by hatched lines. The top two areas show the devices which interface to the UNIMA analog and digital I/O systems respectively, and the bottom area shows the image acquisition system.

As shown in the figure, the EMAP/UDAC analog modules in the UNIMA system are used to control and measure force from the 13 stretch galvanometers, to control the two phase-stepping galvanometers, and to monitor the bath temperature via the thermocouple. The UNIMA digital interface system is used to control the LCR, as well as the laser light shutter and the white light source via a digitally activated switch.

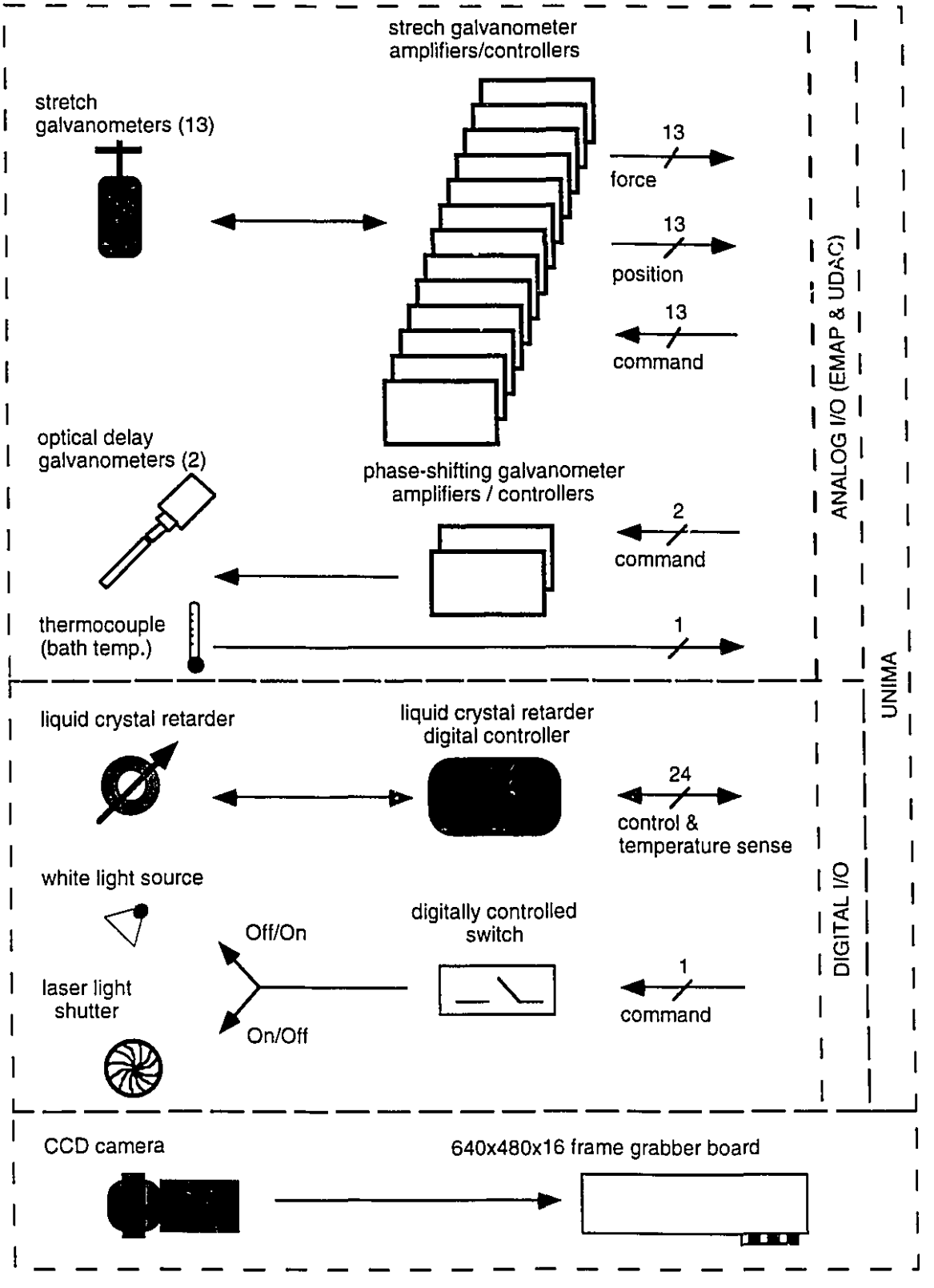

Figure 3.5: Data acquisition and control flow diagram

Note that in order to minimize 60 Hz electrical line noise, the galvanometer amplifiers as well as all analog electronics in the UNIMA system are powered by large (5 MJ) lead/acid deep cycle discharge batteries. This precaution decreased overall electrical noise dramatically.

3.5 Data acquisition and control software subsystem

The workstation and the subsequent data analysis were controlled by a custom application program called *XVG*, running under the AIX Windows operating system (IBM X-Windows). The program, written over the course of this project, consists of over 35000 lines of C code. The program has a flexible graphical user interface (GUI) outer shell which was built with the help of the IBM AIC interface composer utility (IBM, 1993). The many different XVG interface windows used to interact with the user for experimental control and data analysis tasks are shown in the Appendix. The XVG program functionality is shown in flow chart form in Figure 3.6. As seen in the figure, the program code is separated into six functional blocks:

(1) Image acquisition:	this functional block includes code to control the image acquisition from the frame grabber board and process the data according to the phase stepping algorithm.
(2) Image processing:	this functional block includes code to execute a variety of image processing functions on the data such as space and frequency domain filtering, morphological operations, polynomial and spline modeling, etc. This functional block also included the finite element analysis and modeling code.
(3) File I/O:	this functional block includes code to save the data to disk under a variety of formats such as TIFF, MATLAB, etc.
(4) UNIMA interface:	this functional block provides a library of interface routines to the various UNIMA subsystems, for use by other functional blocks.
(5) 3D graphics display:	this functional block includes code to interactively manipulate the data sets in three dimensional space, using the GL graphics library.
(6) Sequence animation:	this functional block includes code to create animated sequences from data set sequences, which can be shown on the workstation screen or downloaded directly to a digitally controlled VCR.

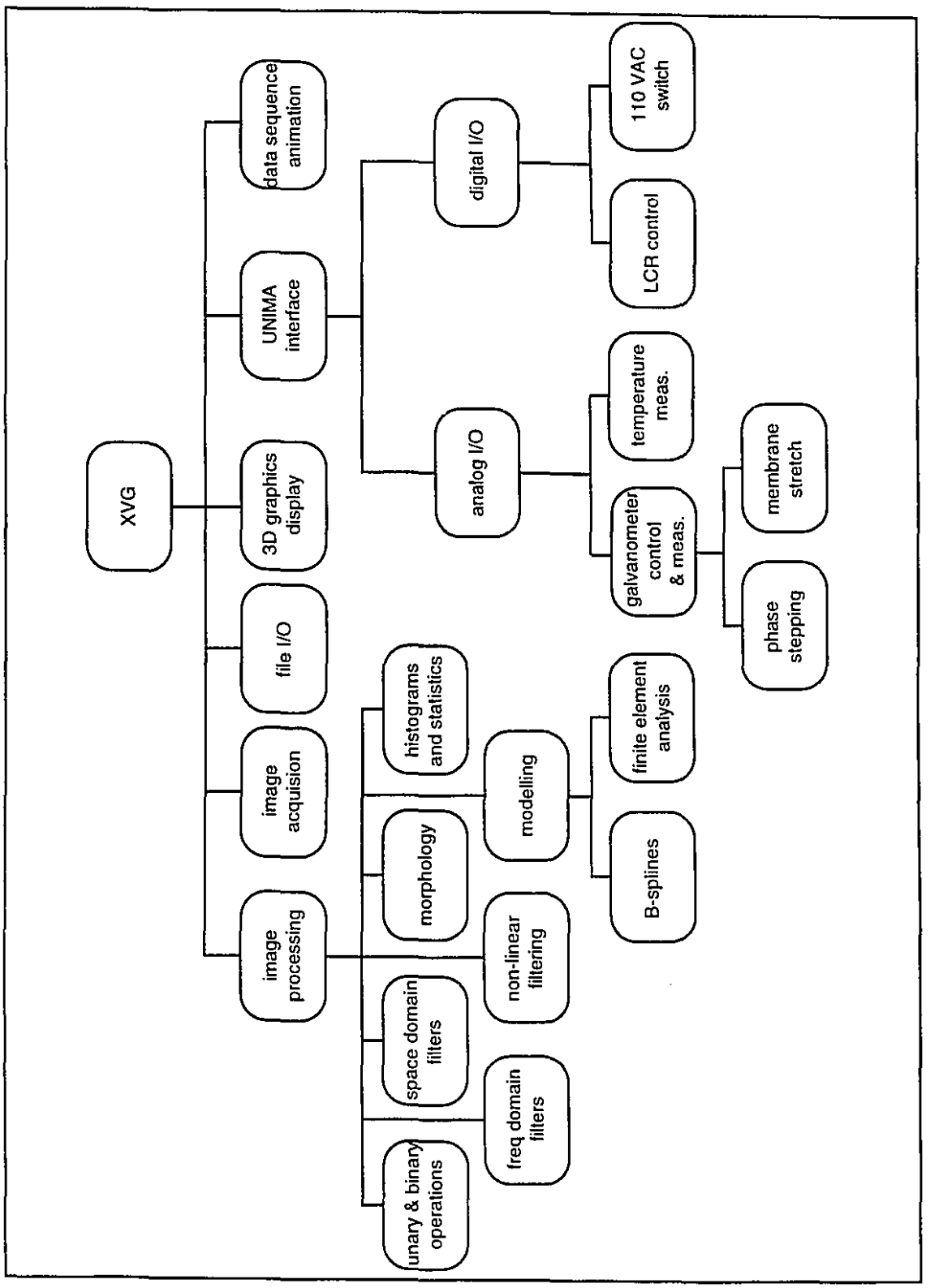

Figure 3.6: Software structure block diagram of the control, data acquisition and analysis program XVG.

PLATE I: Photograph of the experimental apparatus on the optical table with the environmental isolation enclosure in the fully raised position.

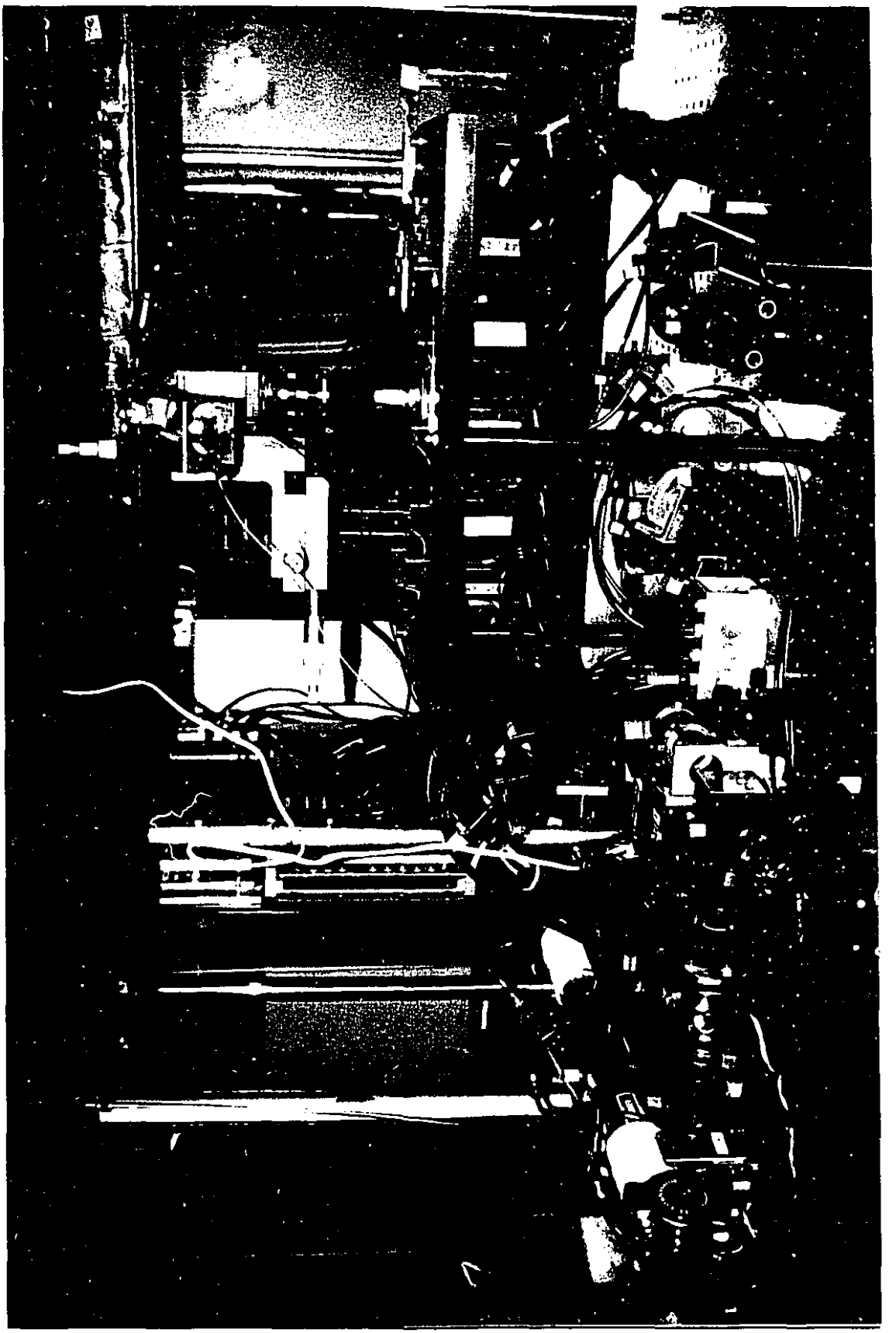

PLATE II: Close-up photograph of the experimental apparatus on the optical table.

PLATE III: Photograph of the instrumentation rack and workstation.

Chapter 4

Noise Analysis and Calibration

This Chapter describes the different calibration and noise level estimation procedures used for the experimental apparatus and the subsequent experimental results presented in the Chapters 5 and 6. The Chapter is divided in two parts which separately address the calibration and noise analyses for the forces measurements, and for the displacement calculations from the optical phase measurements. Theoretical error calculations are compared to experimental noise measurements whenever possible.

4.1 Displacement measurement calibration and error analysis

In speckle interferometry, as explained in Chapter 2, material displacements are determined indirectly from measurements of optical phase changes in the speckle pattern. Obviously, the underlying assumption is that the optical phase changes reflect the material displacements in some predictable way, and that this displacement-to-phase mapping can be inverted to recover the original displacements.

In order to evaluate the uncertainty or error on the final displacement estimates, the mechanism by which displacements are converted to optical phase and then back to displacements must be studied in detail, and the noise associated with each step in the process must be considered separately. This sequence of events is shown in block diagram form in Figure 4.1. The present section studies each step of the sequence in turn and concludes with the calculation of a global noise estimate for the displacement calculations.

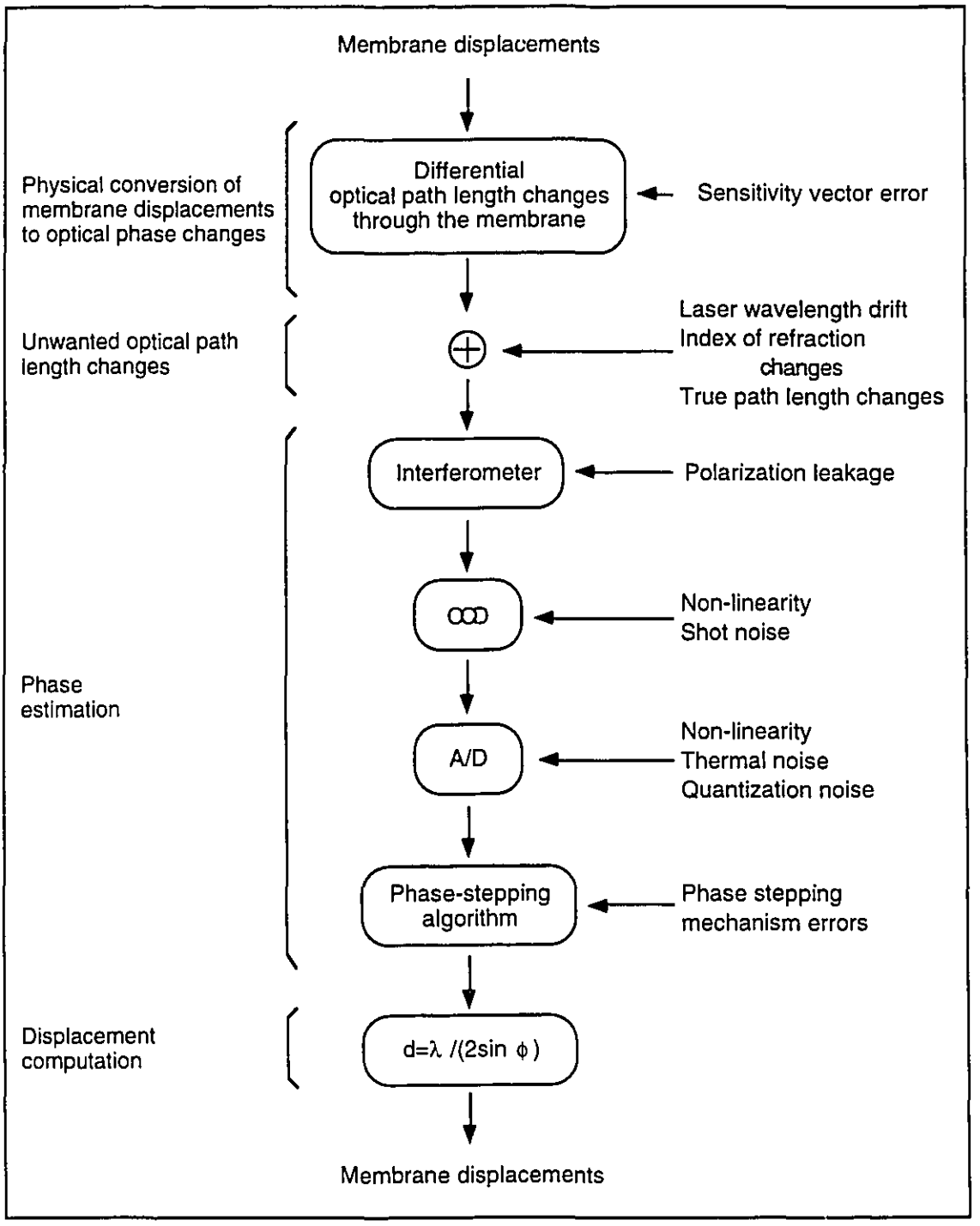

Figure 4.1: Block diagram description of the different steps involved in the measurement of membrane displacements. The error sources for each step are shown on the right.

In the Figure, the various steps in the sequence are shown vertically, with the error sources inherent to each step shown on the right. As explained in Chapter 2, membrane

displacements cause differential optical phase changes between the two laser beams transmitted through the material. Because the two light waves are coherent, their mutual interference converts the phase differences between the beams into a stable irradiance pattern encoding which can be recorded by a video camera and digitized for computer processing. Using phase-stepping methods, the phase difference between the two wavefronts can be recovered, from which displacements are then calculated based on the geometry of the interferometer.

In the following error analysis, the displacement-to-phase mapping sequence is grouped into three separate processes (as shown on the left in Figure 4.1):

(1) Physical conversion of displacements to optical phase changes.

(2) Unwanted optical path length changes.

(3) Phase estimation (Interferometry, CCD recording, A/D conversion, phase-stepping).

Note that the last process in Figure 4.1, termed "displacement computation" is simply the mathematical inverse of the physical processes in steps (1) through (3). It is considered "noiseless" relative to the other three processes for two reasons. First, all calculations are done in double precision floating-point, so that roundoff error is negligible compared to measurement errors inherent to physical processes. Second, the uncertainty on the physical constants used in the computation (λ and ϕ) is included in the first three processes of the noise analysis.

In Sections 4.1.1 to 4.1.3, each of the first three processes shown in Figure 4.1 is analyzed separately. In Section 4.1.4, a global noise figure for displacement measurements is given, based on the analysis of the three preceding sections. Note that while certain noise processes could be modeled theoretically, others could only be estimated from experimental measurements. Whenever possible, experimental confirmation of theoretical noise calculations are presented. Required calibration procedures are also described. The reader is encouraged to refer to Figure 4.1 frequently as the error analysis that follows is rather involved.

4.1.1 Physical conversion of material displacements to optical phase changes

The mapping of material displacements into optical phase changes in based on the *sensitivity vector* of the interferometer. The degree to which the direction of the sensitivity vector can be ascertained is finite, and hence carries with it a basic measurement uncertainty. In this section, this error term is evaluated and an experiment designed to verify the theoretically predicted value is presented.

Note that in speckle interferometry, as explained in Chapter 2, planar displacements are *separately* measured along two orthogonal sensitivity vectors in the plane. In the discussion below, the noise analysis concerns the sensitivity vector along the e_1 axis only, as the analysis for the sensitivity vector along the e_2 axis is identical.

The mapping between material displacements and optical phase change $\Delta\theta$ (see Equation 2.25) at a point is based on projection of the displacement vector $\boldsymbol{d}$ onto the sensitivity vector $\boldsymbol{K}$ as shown in Figure 4.2 below (Jones and Wykes, 1989):

$$\Delta\theta = \frac{2\pi}{\lambda}(\mathbf{K} \bullet \mathbf{d}), \tag{4.1}$$

where:

$$\mathbf{K} = (\mathbf{n}_a - \mathbf{n}_o) - (\mathbf{n}_b - \mathbf{n}_o) = (\mathbf{n}_a - \mathbf{n}_b), \tag{4.2}$$

and:

$$\mathbf{d} = d_1\mathbf{u}_1 + d_2\mathbf{u}_2 + d_3\mathbf{u}_3, \tag{4.3}$$

where n_a and n_b are unit vectors in the illumination directions, n_o is a unit vector in the observation direction, and the u_i are unit vectors along the e_i axes. Since n_a and n_b are unit vectors, K can be expressed as:

$$\begin{aligned}\mathbf{K} = {} & (\sin\phi_a\cos\varphi_a + \sin\phi_b\cos\varphi_b)\mathbf{u}_1 \\ & + (\sin\phi_a\sin\varphi_a - \sin\phi_b\sin\varphi_b)\mathbf{u}_2 \\ & + (\cos\phi_a - \cos\phi_b)\mathbf{u}_3\end{aligned} \tag{4.4}$$

Hence from (4.1) to (4.4), the optical phase change $\Delta\theta$ resulting from a material displacement $\boldsymbol{d}$ along the sensitivity vector $\boldsymbol{K}$ is expressed by:

$$\begin{aligned}\Delta\theta = \frac{2\pi}{\lambda}\{&(\sin\phi_a\cos\varphi_a + \sin\phi_b\cos\varphi_b)d_1 \\ &+(\sin\phi_a\sin\varphi_a - \sin\phi_b\sin\varphi_b)d_2 \\ &+(\cos\phi_a - \cos\phi_b)d_3\}\end{aligned} \qquad (4.5)$$

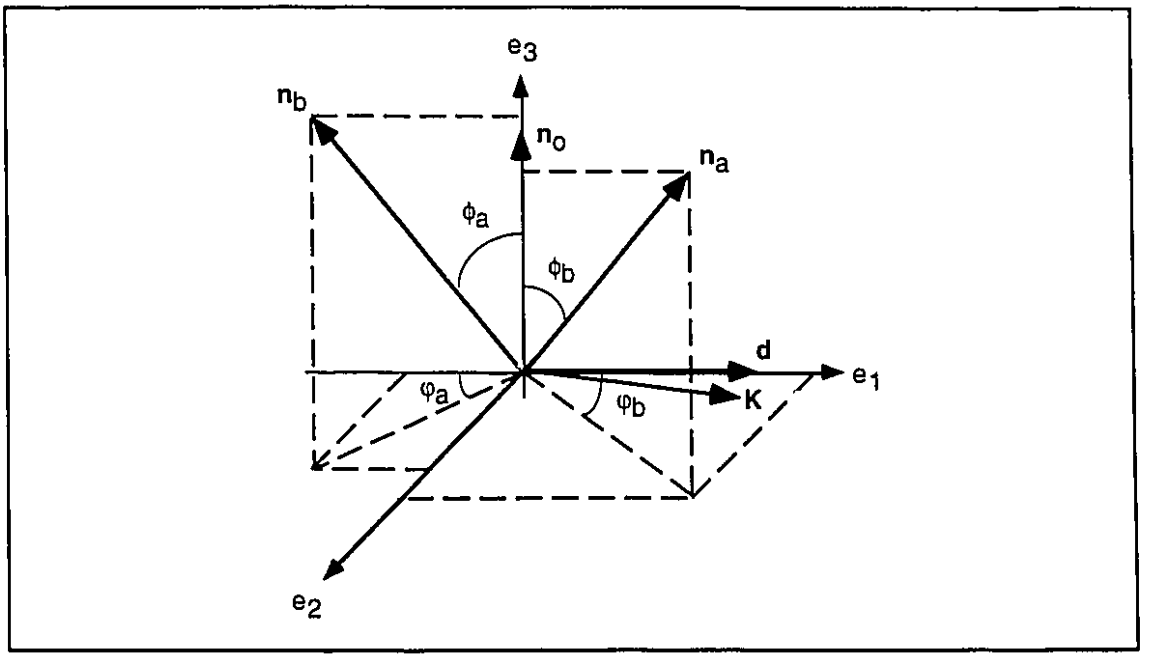

Figure 4.2: Schematic diagram used to determine the sensitivity vector $\boldsymbol{K}$ of the interferometer ($\boldsymbol{K} = \boldsymbol{n}_a - \boldsymbol{n}_b$), where $\boldsymbol{n}_a$ and $\boldsymbol{n}_b$ are unit vectors in the directions of illumination, $\boldsymbol{n}_o$ is a unit vector in the direction of observation, and $\boldsymbol{d}$ is the displacement vector of a material point.

4.1.1.1 Uncertainty on the sensitivity vector direction

For perfect alignment, when $\phi_a=\phi_b=\phi$ and $\varphi_a=\varphi_b=0$ (where ϕ is the theoretically ideal angle of incidence of both light beams onto the membrane surface), (4.5) reduces to:

$$\Delta\theta = \frac{4\pi d}{\lambda}\sin\phi, \qquad (4.6)$$

which is the standard relation between surface displacements and optical phase changes for in-plane displacements (see Equation 2.22). In practice however, perfect alignment is an

asymptotic goal, and the angles ϕ and φ can only be determined to a finite degree of accuracy.

In the apparatus, the uncertainty on both angles was due mainly to the hysteresis and finite mechanical stability of the optical mounts. Indeed, all optical mounts have a certain amount of mechanical "play" or hysteresis. Although this problem can be alleviated by locking the mounts into position with a set screw for example, this often makes delicate alignment more difficult because the optics may shift slightly when the screw is tightened.

All mounts used in the apparatus (part off-the-shelf, part custom made) relied on the stiffness of restoring force mechanisms (such as a spring) for stability. Hence over time, because of factors such as the raising and lowering of the environmental enclosure, thermal cycling and other mechanical noise, the optical alignment shifted slightly within the hysteresis range of the mounts. The estimation of the angles φ and ϕ was also limited by the relatively short distance (1 m) over which the laser beams could be propagated for alignment. This distance was constrained by the environmental protection enclosure volume, when in the fully raised position.

Therefore, because of the mechanical hysteresis in the mounts and the finite alignment propagation distance, it was estimated experimentally that the angles ϕ and φ could be determined to the following accuracies:

$$-1.5^{o} \leq \varphi \leq 1.5^{o} \quad (\text{nominal} = 0^{o},\ \delta\varphi = \pm 1.5^{o})$$

$$18.7^{o} \leq \phi \leq 19.9 \quad (\text{nominal} = 19.3^{o},\ \delta\phi = \pm 0.6^{o}).$$

In the ideal case, the sensitivity vector $\boldsymbol{K}$ has no component in either the e_2 or e_3 directions, and has a single component equal to $2\sin\phi$ along the e_1 axis. Hence the worst case error in the direction of $\boldsymbol{K}$ occurs when the component along the e_1 axis is *minimized* and the component along the e_2 axis is simultaneously *maximized*. The component along the e_3 axis is irrelevant since by hypothesis the displacements of the membrane occur only in the e_1e_2 plane. The worst case situation occurs when $\delta\phi = -1.5^{o}$ and $\delta\varphi = \pm 0.6^{o}$ simultaneously.

In the experiments (see Chapter 5), the membrane displacements were generally quasi-uniform, i.e.: $d_1 \approx d_2 \approx d$. In this case, with $-\delta\varphi_a = \delta\varphi_b = 0.6^o$ in order to maximize the component of $\boldsymbol{K}$ along the e_2 axis, (4.5) reduces to:

$$\Delta\theta = \frac{4\pi\sin(\phi - \partial\phi)d}{\lambda}\{\cos(\partial\varphi) - \sin(\partial\varphi)\}. \tag{4.7}$$

In both (4.6) and (4.7) the phase change $\Delta\theta$ and displacement d are related by a simple scaling factor. The difference between both scaling factors is a measure of the worst case error in the process of physical conversion of material displacements to optical phase changes. Using the specified values for the nominal and worst case values of φ and ϕ in equations (4.6) and (4.7) respectively, the worst case error on $\Delta\theta$ is equal to $\pm 5.6\%$. For the special case of uniaxial displacements in the e_1 direction only (i.e.: $d_2 = 0$), as in the test experiment described below, the worst case error on $\Delta\theta$ is $\pm 3\%$.

Note that the wavelength, λ, of the light in the medium also carries an uncertainty which affects the scaling between displacement and phase (see (4.6) and (4.7)). However, unlike the uncertainty in $\boldsymbol{K}$ which is systematic, the uncertainty on λ changes with time throughout the experiment. For this reason, this effect is studied in section 4.1.2 along with other time-varying factors.

4.1.1.2 Experimental noise measurement

A special experiment was designed to evaluate the effect of the sensitivity vector uncertainty on the phase measurements. In the experiment, a target membrane was repeatedly stretched by a known amount along a single axis. The known displacement value was then compared to the experimental measurements obtained with speckle interferometry. In this manner, any systematic difference between the expected and measured displacements could be used as a measure of the error in the sensitivity vector $\boldsymbol{K}$.

The experiment was conducted using a mechanically simpler setup for uniaxial stretching only of the target membrane. The speckle interferometer layout however was the same as that described for the full apparatus. The target material was a 10 mm × 10 mm patch of pericardium membrane which was attached along one edge with a rigidly fixed 10 mm wide clamp. The opposing edge was held by an identical clamp attached to a stage

driven by a micro-stepping motor which moved by approximately 55 nm per micro-step (see below).

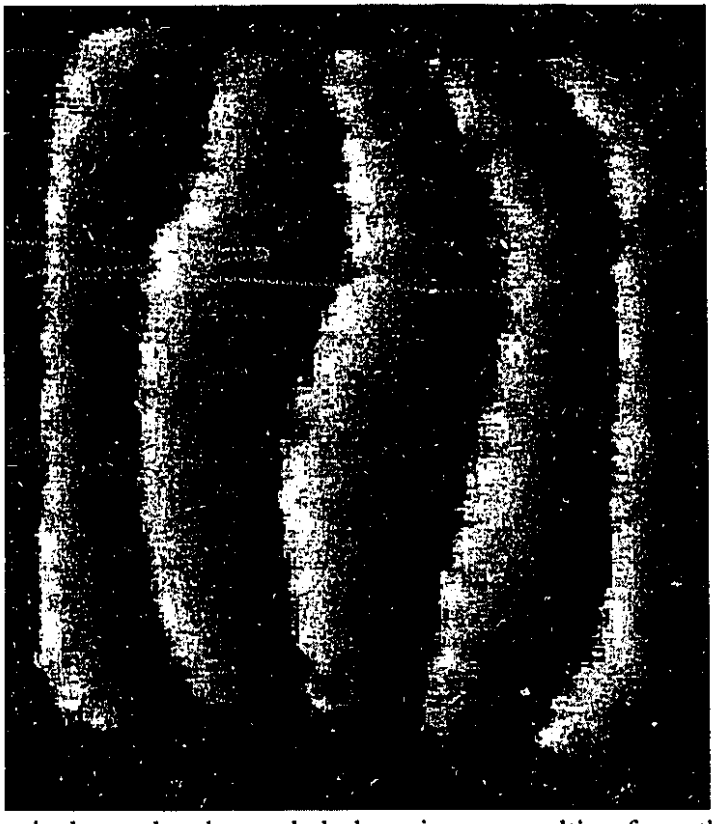

Figure 4.3: Typical gray level encoded phase image resulting from the subtraction of two phase-stepping images recorded before and after stretching. The target membrane was a 10 mm × 10 mm patch of pericardium stretched uniaxially with a micro-stepping motor by 100 micro-steps, or approximately 5.5 μm.

In the experiment, after initial pretensioning, the membrane was repeatedly stretched by a fixed distance of 100 micro-steps (5.5 μm), without reversing direction (so that the mechanical hysteresis of the stepping motor and the stage did not affect measurements). At the end of each 100 step sequence, the speckle images required by the phase-stepping algorithm were recorded and stored for later analysis.

At the end of the experiment, the phase images resulting from the phase-stepping calculations were subtracted in successive pairs. This process yielded a series of differential phase maps corresponding to the displacements of the membrane between each 100 step stretch, in the stretching direction. A typical result is shown in Figure 4.3, where the fixed

edge is on the left hand side and the moving edge on the right. In the Figure, the optical phase is gray level encoded, so that black pixels correspond to phase values of $-\pi$ radians and white pixels correspond to phase values of π radians. The abrupt dark to light transitions in the data are $-\pi$ to π phase discontinuities or "fringes".

According to the manufacturer, the stage lead screw had a pitch of 18 turns/in (1 in = 25.4 mm) and the micro-stepping drivers had a resolution of 25600 steps/revolution, thus resulting in an effective displacement resolution of 55 nm/step. Hence for 100 steps, the estimated applied displacement was 5.5 μm. From (4.6) above, at nominal values of ϕ = 19.3° and $\varphi = 0°$, the scaling factor between phase and displacement is 152 nm/rad, or 0.96 μm/fringe, since each fringe corresponds to 2π radians. Therefore, a displacement of 5.5 μm was expected to generate 5.76 fringes. The results from twenty-five 100 step stretch trials are shown in Figure 4.4 below. The number of fringes in each image was calculated by manually counting the number of phase discontinuities (fringe lines) in each differential phase image, along the horizontal line joining the clamp centers.

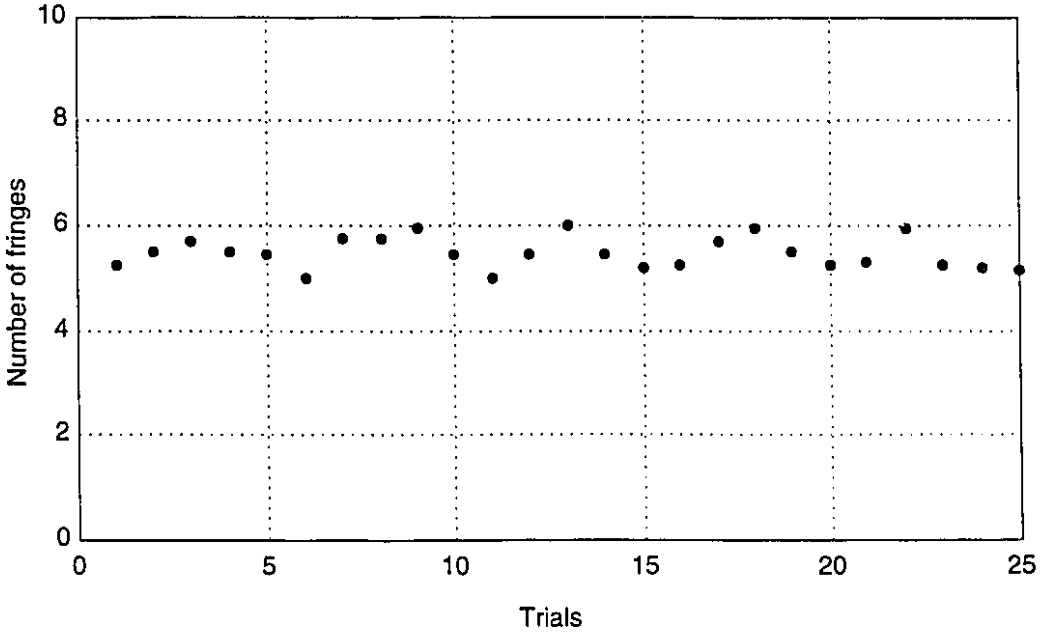

Figure 4.4: Plot showing the number of fringes in the subtraction results from images recorded before and after stretching of the target membrane by 100 micro-steps.

The mean number of fringes across the 25 trials of the experiment shown in Figure 4.4 was 5.49 fringes (standard deviation = 0.3), or 4.6% less than the theoretical value (5.76 fringes). Although the error in this experiment was slightly higher than expected

from theory (> 3%), it is still close enough to confirm the theoretical predictions. Note that this discrepancy is not altogether unexpected. Indeed, the stepping motors were driven open loop with only the manufacturer's specifications to rely on in order to estimate the true membrane displacements. The actual accuracy of the imposed displacements was thus unknown. Furthermore, as the stepping motors were mechanically very noisy, a relatively long time delay (5 s) was required after each step sequence to allow the membrane to stabilize before capturing the speckle images. It is conceivable that during this interval, the membrane had time to creep and relax somewhat.

More importantly however, this experiment convincingly demonstrated that speckle interferometry could indeed be successfully used in *transmission* with a *biological membrane* as a target material to measure full field displacements. Indeed, the experiment was an important validation exercise which confirmed that the optical phase measured using speckle interferometry with this apparatus is directly related to material displacements in the plane. As stated in Chapter 1, it is the first time to our knowledge that this type of measurement has been successfully made on biological tissue.

4.1.2 Unwanted path length changes

In any interferometer, processes other that the one of interest which give rise to relative optical path length changes between the interferometer arms are considered to be noise sources. Unwanted path length changes originate from three sources: changes in the laser wavelength at the source, changes in the index of refraction in the medium, and mechanical disturbances which cause true physical length changes in the interferometer. The origin and relative influence of all three noise sources are explored below.

4.1.2.1 Laser wavelength uncertainty

The center wavelength in vacuum λ_o for the HeNe laser source used in this apparatus is 632.8 nm. According to the manufacturer, the uncertainty in this value ($1{:}10^7$/°C or 0.00001%) is attributable mainly to laser cavity length changes caused by temperature fluctuations. From (4.6), any changes in the wavelength of the light will also cause an unwanted change in the scaling factor between displacement and phase, resulting in a error of 0.00001%/°C in the displacement computations. Note that the wavelength of the laser light in air λ is obtained by multiplying λ_o by the index of refraction of air n_a, which differs from unity by 2760×10^{-7} at 15°C, resulting in a nominal value of 633 nm.

4.1.2.2 Changes in the index of refraction

The phase difference between the two interferometer arms is a function of the *optical path length* difference between the two arms. The optical path length is defined as the geometric path (the true physical distance) multiplied by the index of refraction in the medium n_m. Hence any changes in the index of refraction in the medium along the two interferometer paths will cause a corresponding unwanted change in the phase of the interference pattern.

In the apparatus, the laser light propagated through four different media: air, glass, saline solution, and pericardium. However, the path length through the bath media (glass, saline solution, and pericardium) was very short relative to that in air. Furthermore, the two interfering light beams traversed the bath media together within a very small volume ($\sim 8\times10^{-6}$ m^3) compared to that in air (1m^3). Since the indices of refraction of glass, saline solution, and pericardium are not markedly different from that of air ($n_{glass} \approx 1.5$, $n_{saline\ solution} \approx n_{pericardium} \approx 1.3$), there is no great difference in the scaling of errors between the different media given similar error sources. Hence because of these factors, it is assumed here that unwanted changes in the optical path length due to index of refraction changes were dominated by effects in the air medium. Errors due to index of refraction changes in the bath media are thus ignored in the discussion below.

From Charette (1990) and Charette *et al.* (1992), it is known that changes in the index of refraction of air under normal laboratory conditions will be mainly influenced by the change in temperature (compared to changes in humidity, barometric pressure, and CO_2 concentration), where the scaling factor is: 10^{-5}/°C. Although it can be assumed that, in the experiments, temperature changes occurred on a slow time scale relative to the sampling frequency, the actual magnitude of the temperature variations in the apparatus enclosure were very difficult to predict. Indeed, the galvanometer heating pads (operating around 40 °C) acted as distributed heat sources and the optical table top acted as a large heat sink at room temperature (20 °C). Hence temperature differentials as large as 20 °C existed within the enclosure causing worst case index of refraction changes, and corresponding phase errors, of 0.02%. Note that the laser itself, often the most important source of heat in any interferometer, was enclosed in a custom build water cooled heat sink in order to reduce this effect.

4.1.2.3 True physical path length changes

True propagation length changes in the interferometer were caused by mechanical noise disturbances such as building vibrations, acoustic noise, and dimensional changes of the apparatus components due to temperature variations. Although the environmental enclosure and the optical table significantly attenuated this type of noise originating from the outside environment (Brenan *et al.*, 1992), the actual magnitude of the noise within the enclosure was difficult to estimate theoretically.

Mechanical noise components at frequencies near or higher than the time scale of the experimental measurements (5 s sampling interval, see Chapter 5) caused rapid path length changes in the interferometer during the sampling period and thus introduced a certain amount of "blurring" in the speckle pattern recording. This effect on the displacement measurements could not be measured directly however since it could not be decoupled from other noise sources. Is thought however that the environmental enclosure and the optical table suspension system reduced this noise type to very negligible proportions.

Low frequency mechanical noise such as slow building vibrations (<1 Hz) and temperature cycling effects also caused path length changes in the interferometer, but on a relatively slow time scale. The effect of this type of noise was to introduce a different phase offset between the interferometer arms, at each measurement. Hence *differential* phase measurements between two consecutive samples carried with them a global random phase offset due to low frequency mechanical noise. Although it was difficult to quantize theoretically, this effect could nevertheless be estimated experimentally, as described in the next section.

4.1.2.4 Experimental measurement of low frequency noise

A special experiment was run in order to assess the combined effect of all low frequency mechanical noise sources on the displacement measurements, over the time period corresponding to one sampling interval (5 s). These noise sources are: laser wavelength drift, index of refraction fluctuations, and low frequency mechanical noise. In the experiment, the target material was a thin polymer sheet which was rigidly mounted in the sample chamber of the interferometer. After the environmental isolation enclosure was lowered and the system had been allowed to thermally stabilize, a total of 25 optical phase maps were sampled using the phase-stepping process and recorded on disk, at 5 s intervals. After the experiment, the phase data sets were subtracted from one another in successive pairs, and the results were smoothed using a median filter (see Chapter 5 for a description of the median filter). The probability density function of a typical smoothed phase image is shown in Figure 4.5.

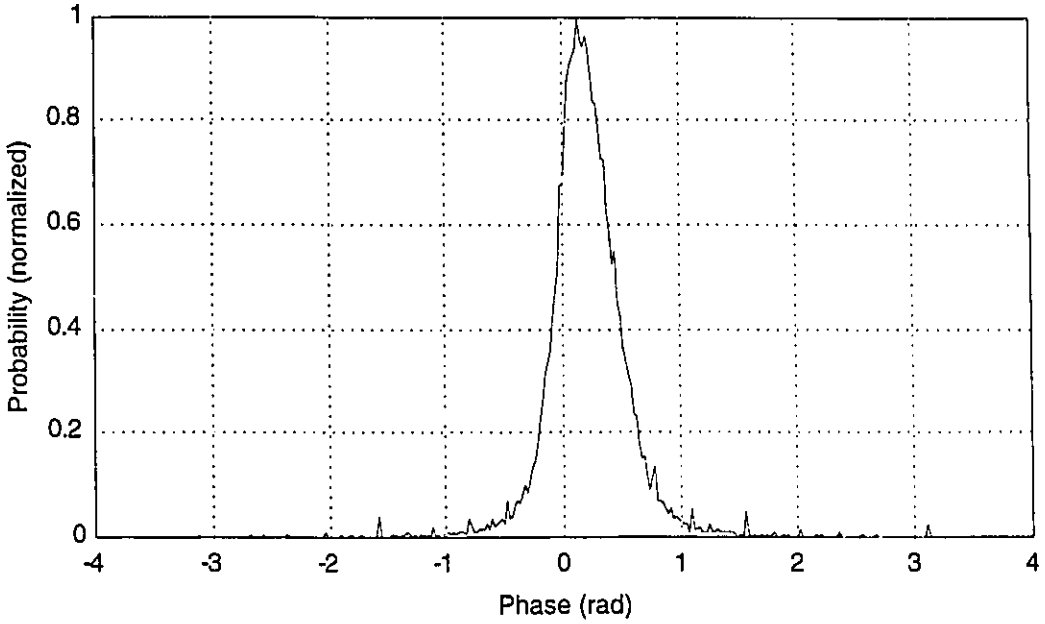

Figure 4.5: Probability density function of the phase data resulting from the subtraction of two phase images recorded at 5 s intervals from a fixed polymer sheet target. The data were filtered using a 5×5 median window.

Theoretically, each image resulting from a subtraction should have yielded an image with zero mean phase because of the absence of target displacement. The results of the 25 trials (see Figure 4.6) show significant deviations from zero however, due to random low frequency noise effects. The standard deviation σ (0.17 rad) of the mean phase values

is a measure of low frequency mechanical noise effects on the phase measurements, over a 5 s interval. Assuming the noise contributions to be statistically independent, the total noise on the phase estimates due to low frequency true physical path length changes across an experiment will be equal to $\sqrt{N}0.17$ rad, where N is the number of image samples.

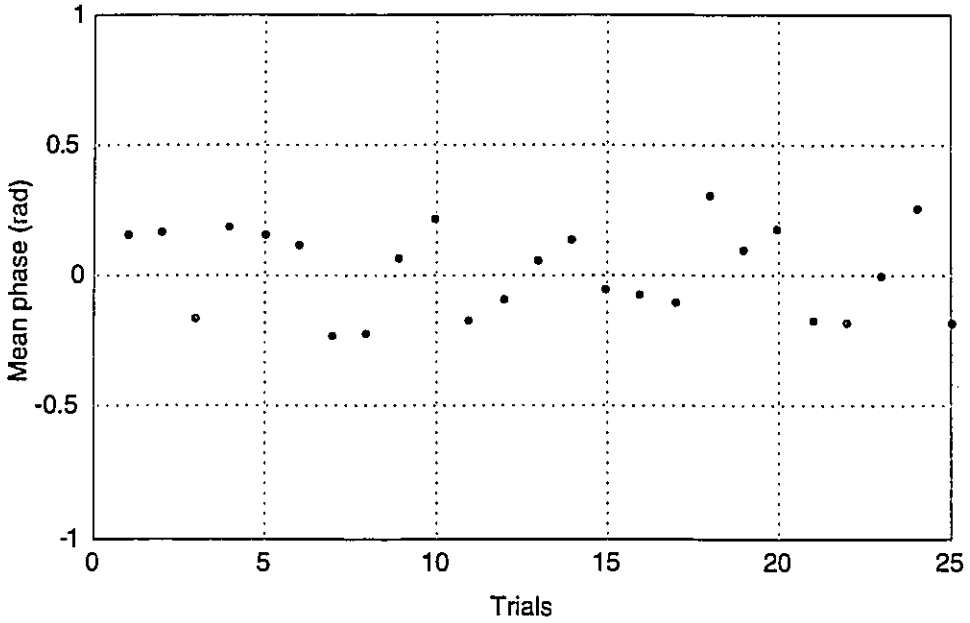

Figure 4.6: Plot of the mean phase values from 25 subtraction results between images acquired from a fixed target at 5 s intervals.

4.1.3 Phase estimation errors

As explained in Chapter 2, phase images corresponding to displacements in the plane along the e_1 and e_2 axes were generated using a phase-stepping algorithm from data sets containing two groups of four phase-shifted images. The error on the phase estimates thus depended on the sensitivity of the phase-stepping algorithm to the various noise sources involved in the phase-stepping process and the image acquisition.

In the following sections, the phase stepping mechanism is described in detail and the influence of the various noise components on the algorithm is evaluated. The procedure used to calibrate the phase-stepping mechanism is also described. Note that the noise sources affecting the phase estimation process can be separated into two categories: (1) the uncertainties in the phase-stepping mechanism proper (i.e.: errors in the imposed optical delay), and (2) the noise in the irradiance measurements.

4.1.3.1 Phase-stepping mechanism model

As mentioned in Section 3.2, the phase stepping optical delay in the apparatus was obtained by counter-rotating two glass windows in the beam path of one of the interferometer arms. This process is modeled mathematically below. From simple geometry, it can be shown that the *relative optical delay change*, α, for a light wave at wavelength λ in air passing through a glass plate of thickness t and index of refraction n_g that has been rotated by an angle θ from normal incidence is given by:

$$\alpha = \frac{2\pi t}{\lambda}\left\{\frac{n_g^2 - C^{0.5}\cos\theta - \sin^2\theta}{C^{0.5}} + (1 - n_g)\right\}, \tag{4.8}$$

where:

$$C = n_g^2 - \sin^2\theta. \tag{4.9}$$

Note that α indicates the optical delay *change* at angle θ from the delay through the glass plate when $\theta = 0^o$. By differentiating (4.8) with respect to θ, the incremental change in optical delay $\delta\alpha$ with angle $\delta\theta$ is obtained:

$$\partial\alpha = \frac{2\pi t}{\lambda}\left(\sin\theta - 0.5C^{-0.5}\sin 2\theta\right)\partial\theta. \tag{4.10}$$

Another parameter of interest in the distance s swept laterally by the laser beam across the glass plate due to rotation. Again, from simple geometry, it can be shown that the *change* in lateral sweep distance δs with rotation angle change $\delta\theta$ is given by:

$$\partial s = t\cos\theta\left\{C^{-0.5} + C^{-1.5}\sin^2\theta\right\}\partial\theta. \tag{4.11}$$

The two glass windows used in the apparatus were made of 30 mm diameter 6 mm thick optical grade BK7 glass. Note that both windows were angled at 45° from the laser beam path to direct secondary reflections outside the interferometer (see Figure 4.7).

4.1.3.2 Phase-stepping mechanism calibration

In order to calibrate the phase-stepping optical delay mechanism consisting of the two counter-rotating optical windows, the setup shown in Figure 4.7 was used. A

Michelson interferometer was formed by using mirrors M2 and M7 to reflect the laser light back towards the non-polarizing beamsplitter BS1. The optical interference resulting from the photo-mixing of both returning beams was sampled at a point by a small area detector close to the beamsplitter. Note that in order to get a good quality interference pattern with minimal amplitude modulation, the interferometer alignment had to be adjusted so that the spacing between the fringes at the detector was much wider than the detector area.

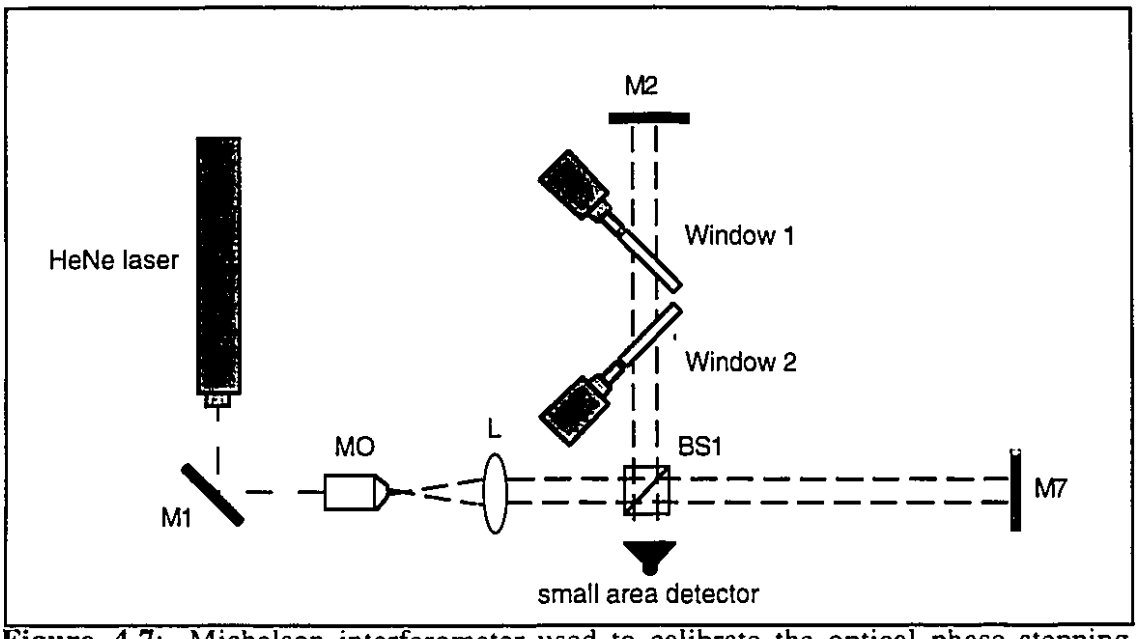

Figure 4.7: Michelson interferometer used to calibrate the optical phase stepping mechanism consisting of two counter rotating glass windows, mounted on the end of precision galvanometer shafts.

A typical result from a calibration experiment is plotted in Figure 4.8 which shows the normalized optical irradiance recorded at the detector for a linear change in equal but opposing rotation angle θ from normal incidence for both windows. Zero-crossings and extrema in the data were identified by the computer to generate a series of discrete sample pairs of window rotation angle and corresponding optical phase delay. The data pairs were then used to generate a least squares fitted 5^{th} order Chebychev model of the input-output relation of the phase-stepping mechanism, where the input is the desired phase delay and the output is the required window rotation (see Figure 4.9). The data (dots) and model (solid line) are shown in the Figure, as well as the theoretical curve (dashed line) generated with Equation 4.8.

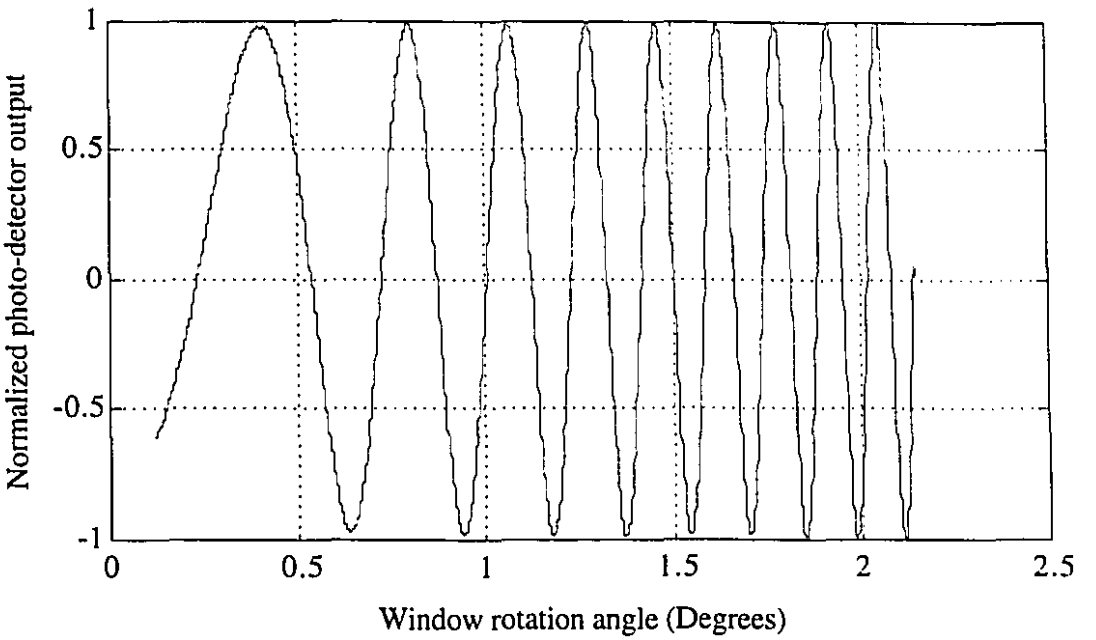

Figure 4.8: Typical result from a phase delay calibration experiment showing the normalized photo-current amplitude plotted against the window angle θ. Note that the steps in the curve are an artifact caused by the plotting routine.

The difference between the theoretical model and the calibration curves in Figure 4.9, and the fact that both curves do not start off at the origin in the plot, is attributable to the imperfect alignment symmetry of both windows in the beam path. Although this effect seems substantial from the plot, the actual angular discrepancies involved are very small. As a consequence however, the lateral shift of the light beam through the opposing glass windows will not be completely canceled out.

4.1.3.3 Phase-stepping mechanism errors

Errors in the optical delay α generated by the phase-shifting mechanism arose from two sources: (1) errors in the window rotation angle θ and (2) imperfections in the glass windows themselves. Both error types are studied in this section, starting with errors in the window angle.

Note that the relationship between window rotation angle θ and optical phase delay, α, is non-linear (as seen in Figure 4.9 and Equation 4.8). The effect of window angle errors on the phase delay must therefore be evaluated about a given operating point. As a

consequence of this non-linearity, operating points at large window angles require smaller window rotation changes for a given optical delay, but also suffer from increased sensitivity to noise due to the greater slope. In the experiments, the window angle operating point was around 1°, which from (4.10) corresponded to a slope of 8.55 rad phase delay ($\delta\alpha$) per degrees rotation ($\delta\theta$).

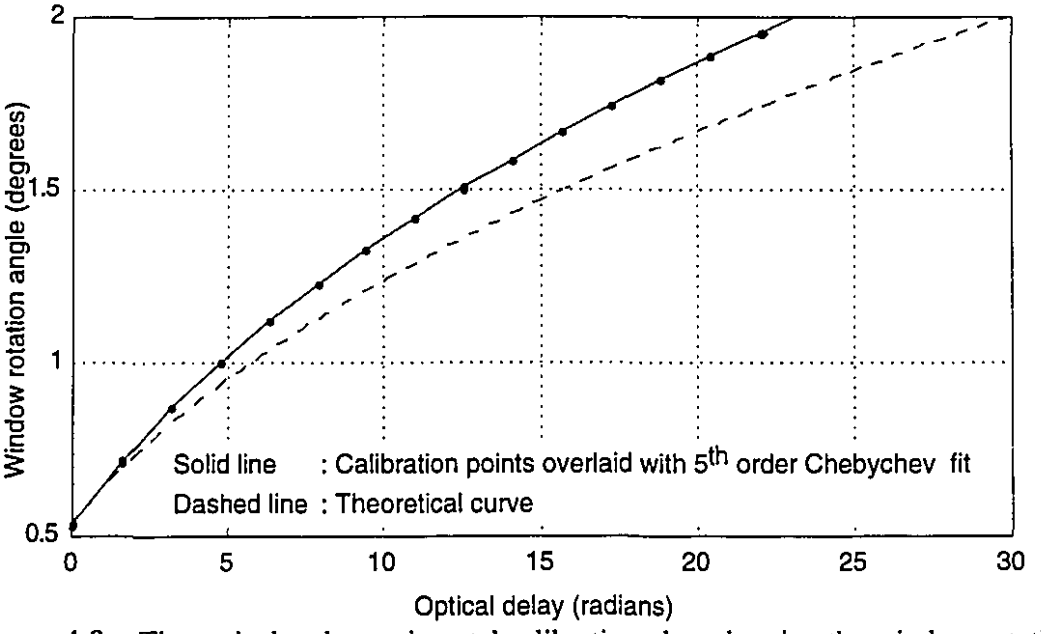

Figure 4.9: Theoretical and experimental calibration plots showing the window rotation angle as a function of the optical delay through the windows. A 5th order Chebychev polynomial fit is overlaid onto the experimental data points obtained from the zero crossings and extrema of a calibration curve such as the one shown in Figure 4.8.

Optical phase delay errors caused by uncertainties in the window angle θ arose from window angular accuracy and resolution. The angular resolution was limited by the root-mean-square (rms) error on window angle and is evaluated in this paragraph. The angular accuracy was limited by the window angle repeatability and is evaluated in the next paragraph. As explained in Chapter 2, the optical windows were mounted on the shafts of precision rotary actuators driven by external amplifier/controller cards (General Scanning AE1000). Measurements using a spectrum analyzer of the noise level on the shaft angle outputs of the amplifiers yielded a noise level of 40 μV_{rms}, in a 100 kHz bandwidth. Since the peak-to-peak swing of the output voltage was 10 V and the total rotational excursion of the shafts of the galvanometers was 50°, this corresponded to a level of

0.0002° *rms* noise. Hence from (4.10), this corresponds to an optical phase delay *resolution* through both windows of 0.003 rad *rms*, about an operating angle of 1°.

The angular position repeatability of the galvanometers (determined experimentally, by directing the laser beam at a small target 5m away) was measured to be better than 0.005°. From (4.10), this corresponds to a peak optical phase delay *accuracy* of 0.086 rad about an angle of 1°. Hence the dominant error on the window angle θ was that due to the finite accuracy (0.086 rad peak).

The second source of errors in the optical delay, α, generated by the phase-shifting mechanism was due to imperfections in the glass windows themselves. According to the manufacturer, the optical windows suffered from two types of imperfections: wavefront distortion ($\lambda/10$ maximum) and deviations from parallelism (1 arc minute maximum). These imperfections in turn caused two types of error: first, the optical delay through the glass varied slightly between any two points across the face of the window for a given rotation angle, and second, the optical delay at a point through the glass varied from one time to the next as the laser beam traversed slightly different paths through the imperfections, due to the finite window rotation angle accuracy.

Since the first type of noise (error between two points) was dependent only on the fixed spatial distribution of the window imperfections, it was effectively constant and was nulled at each point in the image subtraction process. The second type of noise (error at a point) however changed within the bounds allowed by the window position accuracy (0.005°) and is thus studied in more detail. According to (4.11), a 0.005° incremental change in window angle $\delta\theta$ about an operating point of 1° caused a lateral sweep δs of 0.5 μm across the window face. For the purposes of error calculation, both wavefront distortion and parallelism deviation imperfections were assumed to vary linearly across the window area, with 10 and 2.9×10^3 "radians optical delay error" per "meter of lateral sweep" equivalent slopes respectively. Hence, the phase error at a point due to a 0.5 μm lateral shift across both window faces was 0.003 rad, due to parallelism imperfections.

Therefore from the above discussion, it is clear that optical phase delay errors in the phase stepping process were dominated by the finite window angular accuracy (0.086 rad peak) which were much larger than the errors due to window imperfections

(0.003 rad peak). It must be emphasized however that the angular accuracy measurement was limited by the finite propagation distance (5 m) in the experiment. In actual fact, the window angular accuracy may be much higher.

Finally, since this type of error is not systematic, noise contributions across samples can be assumed to be statistically independent. The total noise for the sum of N samples due to the finite window angular accuracy will thus follow a $\sqrt{N}$ dependence. However, the theoretical analysis only allowed the computation of the peak error value, not the variance σ^2. Hence a very rough estimate of the total noise for N samples is equal to $\sqrt{N}0.086$ rad. This is an exaggerated error estimate since the correct expression for the standard deviation of the sum of N statistically independent noise contributions with identical variances is equal to $\sqrt{N}\sigma$.

4.1.3.4 Errors in the irradiance measurements

As mentioned at the beginning of Section 4.1.3, the second source of error in the phase estimation process was the uncertainty associated with the image acquisition, i.e.: the errors on individual speckle irradiance measurements. Such errors arose from three sources: polarization leakage, CCD sampling errors, and A/D digitization errors. The effects of all three are addressed below.

As explained in Chapter 3, polarizing beamsplitters were used to direct the light selectively in the e_1e_3 or e_2e_3 planes at any one time. The polarization extinction ratio of the beamsplitters was finite however and highly angle dependent, so that some light leakage occurred between planes. The interference of the main laser light beams with the secondary leakage beams thus appeared as a noise modulation on the main speckle field.

In order to evaluate the amount of polarization leakage, the following experiment was run: the LCR was adjusted so that the laser light was directed into the e_1e_3 plane. The light reflected off mirrors M3 and M5 was blocked (see Figure 3.1). The speckle pattern recorded by the CCD camera was thus formed by the interference of the light from the main beam reflected off mirror M4 with the leakage light from mirror M6. Using the phase-stepping process, four images were recorded from a fixed target and processed according to the 4-step algorithm to generate the corresponding phase and modulation images. The normalized modulation probability density function (histogram) is shown in Figure 4.10,

and the corresponding probability distribution function (integration of the histogram) is shown in Figure 4.11.

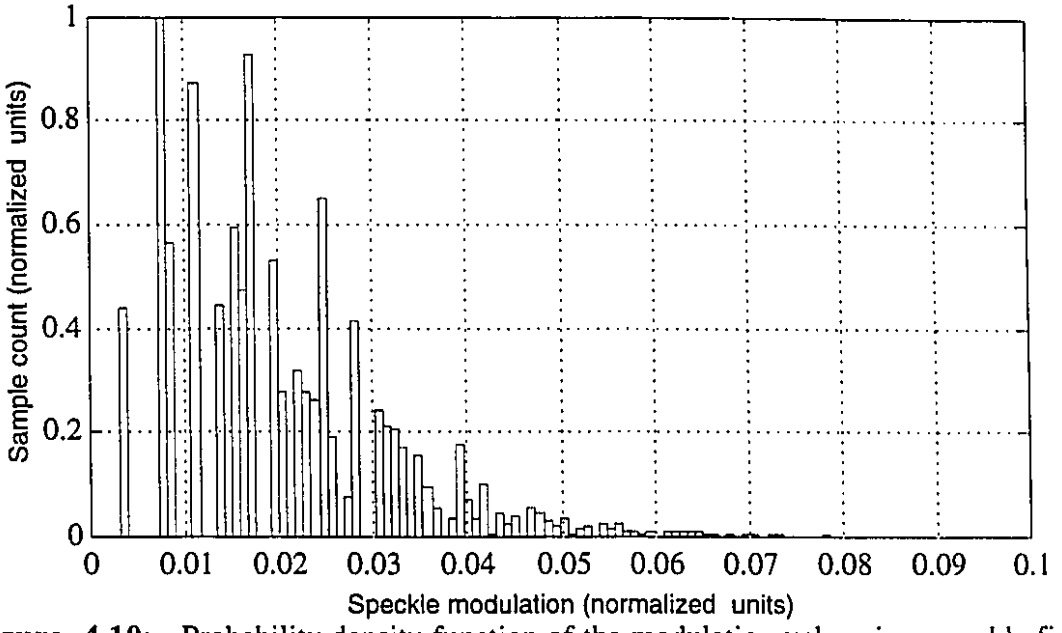

Figure 4.10: Probability density function of the modulation values in a speckle field resulting from the photo-mixing of a single main beam and a secondary polarization leakage beam.

In Figure 4.10, the speckle modulation values are normalized with respect to the largest modulation value that can occur in the speckle pattern recorded by the CCD camera. In practice, the laser power and camera gain are adjusted so that this corresponds to half the CCD dynamic range, in order to obtain the best possible resolution on irradiance measurements. In Figure 4.11, the probability distribution function of the speckle modulation values is shown. As seen from the Figure, over 99% of the speckle modulation values in the image resulting from the interference of the main beam with a secondary leakage beam are under 6% of the largest possible modulation value (see the dashed line in Figure 4.11).

Note that the probability density shown in Figure 4.10 is expected to have roughly the same shape as that for the normal case of interference between two main beams. Hence, it is reasonable to conclude that interference with the polarization leakage beams will cause an average error of 6% in the speckle irradiance measurements.

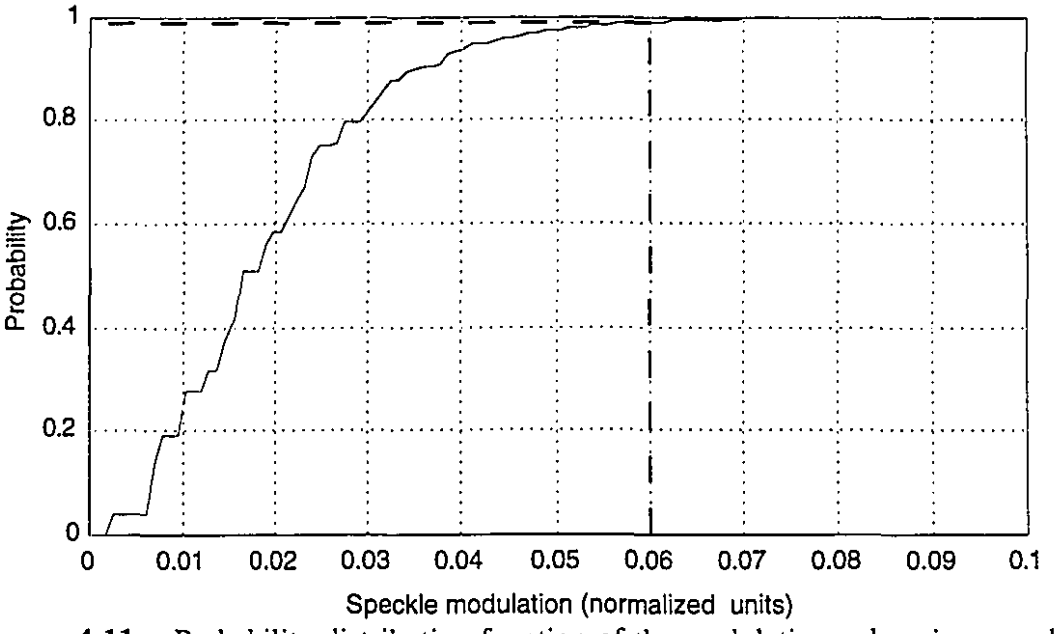

Figure 4.11: Probability distribution function of the modulation values in a speckle field resulting from the photo-mixing of a single main beam and a secondary polarization leakage beam. The dashed line indicates that 99% of the data values are under 6% of the largest possible modulation value.

The second and third types of errors affecting speckle irradiance measurements are those associated with sampling and digitization. According to Thompson (1988), the dominant sources of error in a CCD image sensor are due to shot noise (1% peak-to-peak at low light levels, 0.1%pp at saturation) and non-linearity effects (less 1% peak-to-peak). In the case of digitization, the analog video signal from the CCD is digitized by a 6 bit A/D converter in the frame grabber board. A conservative estimation of the measurement uncertainty in an A/D is to assume 1 bit of non-linearity and 1 bit of noise. Hence 2 bits of total uncertainty out of 6 bits of dynamic range amounts to a total uncertainty of 6.3%pp, which largely dominates over that attributable to the CCD (2%pp).

Hence from the discussion above, it can be concluded that the total error on irradiance measurements will be in the neighborhood of 6%pp, due mainly to polarization leakage and digitization errors. In order to quantify the impact of this error on the phase stepping algorithm, the expression for the step irradiance measurements I_i in (2.27) is reformulated as:

$$I_i = \left[1 + \cos(\theta + \alpha_i)\right](1 \pm \tau), \tag{4.12}$$

where θ is the random speckle phase that must be identified, α_i is the phase step, τ represents the worst case error on irradiance measurements as derived above (i.e.: $\tau = 0.06/2 = 0.03$), and the background and modulation irradiance values have been normalized to 1. By using (4.12) to express I_i in the formulation for the general 4-step method given in Table 2.1.e and using the extreme values of τ to maximize the difference between the numerator and denominator in the argument of the arc tangent function, the worst case error, e, in the estimation of the phase θ is given by:

$$e = \theta - \tan^{-1}\left\{\frac{(1+\tau)}{(1-\tau)}\tan\theta\right\}, \tag{4.13}$$

where, for $\tau << 1$, Equation (4.13) can be approximated by:

$$e = \tau \sin\theta. \tag{4.14}$$

Hence e is a function of the phase angle θ estimated by the phase stepping process. This error is plotted against all values of θ in the $[-\pi,\pi]$ interval in Figure 4.12 below.

According to one of the basic assumptions of the statistics of speckle, all values of phase θ in the $[-\pi,\pi]$ interval are equally likely, and the phase of all speckles are statistically independent (see Chapter 2). Hence, since the error e is a function of the speckle phase θ, and since the plot of Figure 4.12 gives values of e for all phase values θ in the $[-\pi,\pi]$ interval, then all error values shown in Figure 4.12 are also equally likely. Therefore, since it is reasonable to assume that the errors, e, on irradiance measurements at each pixel are statistically independent across samples, this error also follows a $\sqrt{N}$

profile, where N is the number of samples. Hence the total noise on the phase estimates due to the uncertainty in the irradiance measurements will be equal to $\sqrt{N}\sigma$, where $\sigma = \tau/\sqrt{2}$, which is equal to 0.02 rad when $\tau = 0.03$.

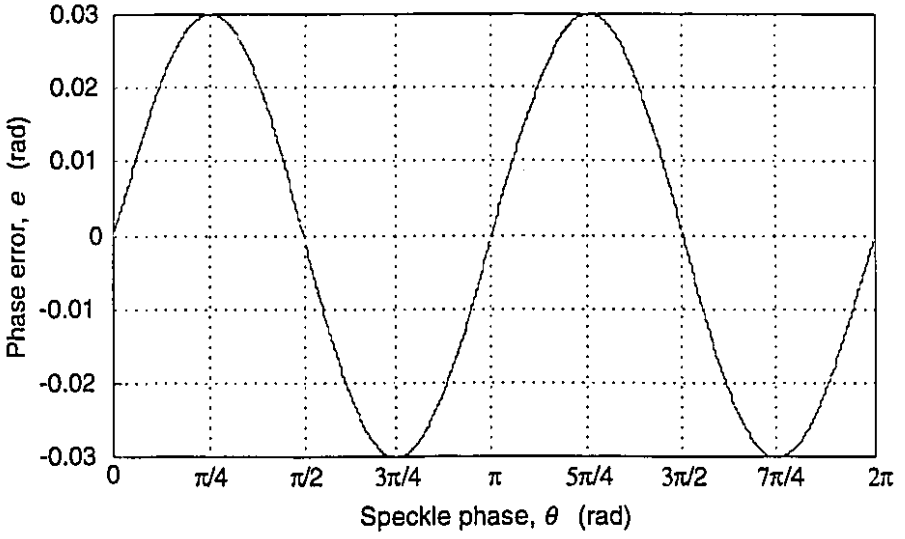

Figure 4.12: Plot of the error e on the speckle phase, θ, at all phase values in the $[-\pi, \pi]$ interval, for a 6%pp uncertainty on the irradiance measurements.

4.1.4 Total error in the displacement measurements

The first conclusion to be drawn from the above error analysis is that with the exception of the errors due to the uncertainty in the sensitivity vector $\boldsymbol{K}$, all other errors scale as $\sqrt{N}$, where N is the number of sample images. Hence in order to minimize the total uncertainty on the final measurements, N must be minimized. To achieve this, the sensitivity of the system must be set as low as possible in order to maximize the displacements per sample. This in turn is accomplished by reducing ϕ, the beam angle of incidence, in order to minimize the scale factor between displacement and optical phase.

In order to compare quantitatively the various noise contributions described in the previous sections, an average number of N images for a typical experiment must be assumed. For the discussion below, N=400 (see experimental results in Chapter 5). Phase error values are converted to displacements using (2.25). Finally, as the displacement sensitivity vector error is expressed as a percentage of total displacement, a typical displacement at maximum extension must be assumed. For the discussion below, a maximum displacement of 1 mm is assumed (see experimental results in Chapter 5).

Hence at N=400 and at a maximum displacement of 1mm, the magnitudes in percentage of all error sources described above are:

(1)	Phase to displacement mapping errors (uncertainty on K)	5.5%
(2)	Low frequency unwanted path length changes:	0.5%
(3.1)	Phase estimation errors due to phase stepping mechanism errors	0.3%
(3.2)	Phase estimation errors due to irradiance measurement errors:	0.1%

Therefore it is expected that the measurement uncertainty on the final displacement estimates will be largely dominated by the error in the sensitivity vector K at 5.5%. Note that the numbering of the error contributions above refers to the different error categories as defined in Section 4.1 and Figure 4.1.

4.2 Force measurement calibration and error analysis

As described in Chapter 3, the forces exerted by the actuators via the linkages were determined indirectly by measuring the AE1000 amplifier voltage outputs which are proportional to the current through the motor coils. In order the determine the relation between applied force and output voltage from the AE1000 amplifiers, the apparatus shown in Figure 4.13 was used.

Each of the 13 stretching galvanometers was calibrated in turn using the apparatus shown in the Figure. The actuators were mounted rigidly at the base of the calibration apparatus and the hook at the end of the linkage was connected to a precision strain gauge force transducer (Omega LCC200). The position command input to the AE1000 was driven over the full positive range using a UDAC 20 bit D/A. The resulting applied force measured by the strain gauge as well as the AE1000 force voltage output were recorded with two EMAP 16 bit A/Ds. A typical result is shown in Figure 4.14. As seen from the plot, the relation between developed force and output voltage was highly linear and could hence be described by a single slope parameter specific to each galvanometer.

Having obtained the scaling parameters to convert the AE1000 output voltage into units of force (N), the galvanometers also had to be calibrated for net force output. Indeed, the galvanometers incorporate an internal torsion bar which acts as a restoring force which

opposes motion. Hence in order to measure the net force applied by the actuators, the forces required to overcome the torsion bar had to be subtracted out. Note that this effect did not come into play in the calibration procedure of Figure 4.14 because the restoring force mechanism does not exert any torque at a shaft angle of 0°. Since the linkages can be considered inextensible, the galvo shafts were effectively constrained at 0° in that procedure.

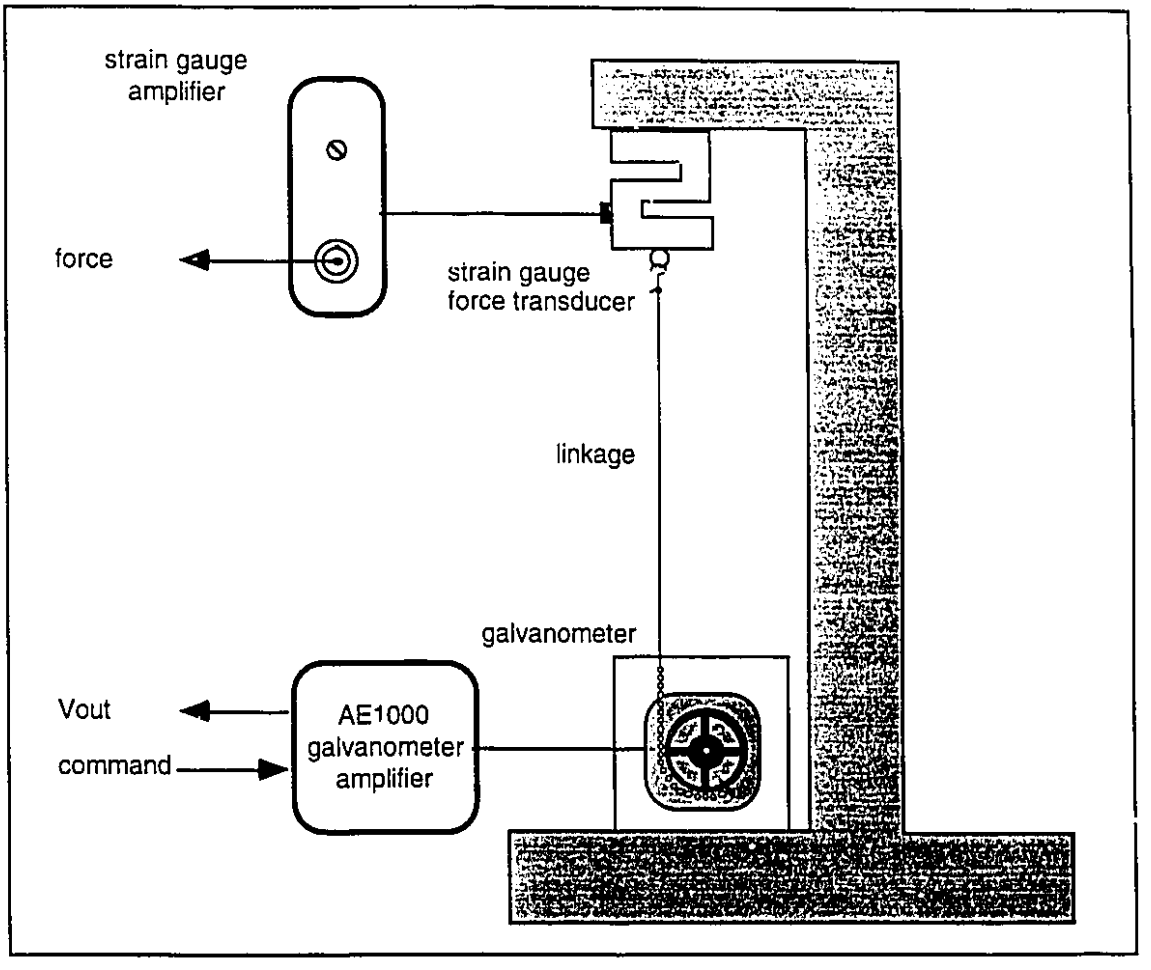

Figure 4.13: Block diagram of the apparatus used to measure the relation between applied force and output voltage for the AE1000 amplifiers coupled to the G350DT galvanometers.

In order to estimate the torque exerted by the torsion bars, the following experiment was carried out: the 13 stretch galvanometers were rotated simultaneous over their entire motion ranges (±25°) without any external load, and the resulting force output voltages were recorded. A typical result for one actuator is shown in Figure 4.15, where the output

voltages were scaled to units of force using the first calibration procedure shown in Figure 4.14.

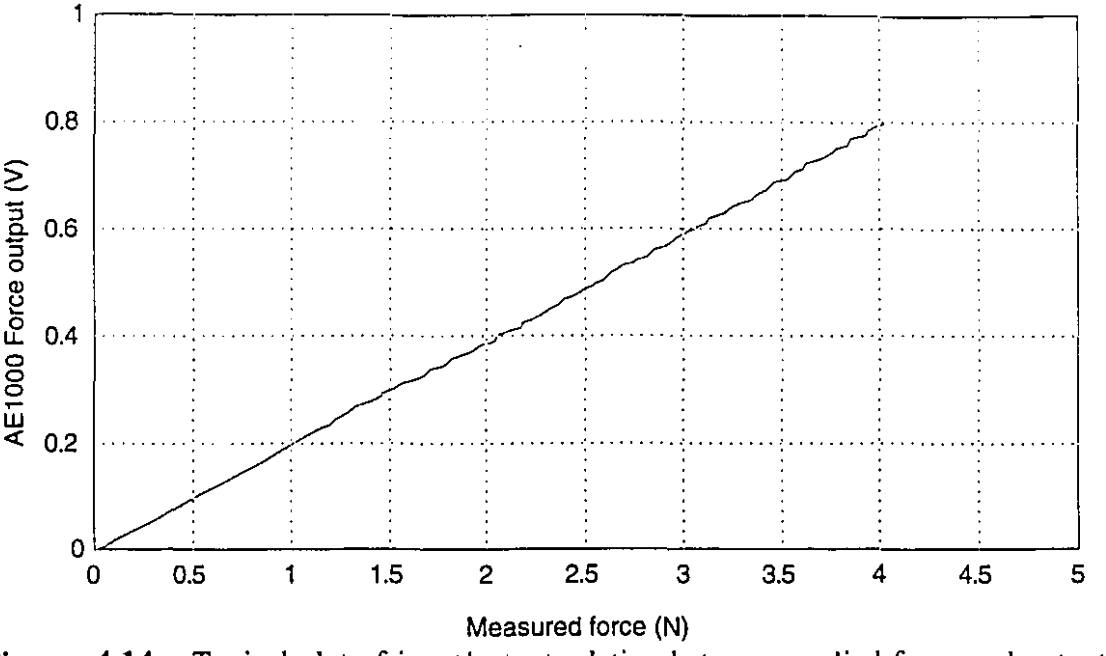

Figure 4.14: Typical plot of input/output relation between applied force and output voltage for the AE1000 amplifiers coupled to the G350DT galvanometers.

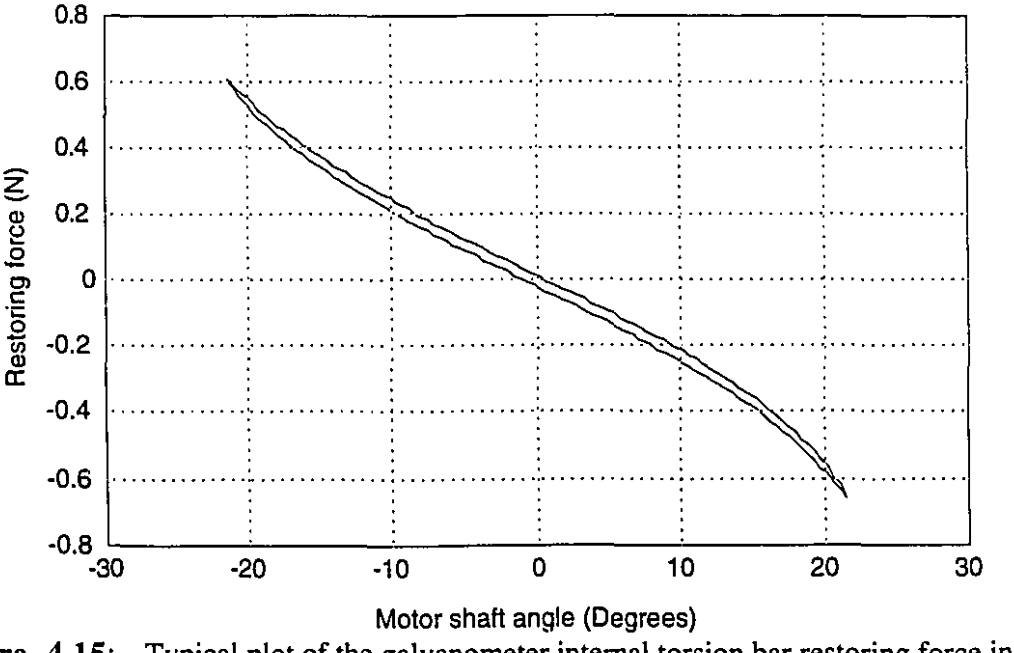

Figure 4.15: Typical plot of the galvanometer internal torsion bar restoring force in the motor mechanism plotted against the motor shaft angle. The small hysteresis due to magnetic and mechanical effects is clearly visible.

The plot in Figure 4.15 clearly shows the small hysteresis inherent in the restoring force mechanism, which is possibly due to both magnetic and mechanical effects. In this application, hysteresis is a highly undesirable feature because the actual magnitude of this effect depends on the past history of the signal. Since the actuators in the apparatus were controlled by analog servo loops in the AE1000 amplifiers, there was no direct experimental control over the actuator motions other than specifying a desired final shaft position, and hence no control over the "motion history".

Furthermore, it is reasonable to assume that the servo loops controlling the pulling actuators competed against each other until a final mechanical equilibrium state was reached. In this case, each actuator would go through a number of overshoot/undershoot cycles before finally settling to an equilibrium position. This behavior would cause the instantaneous I/O relation between motor shaft angle and restoring force to "flip" back and forth between the upper and lower curves in the hysteresis plot shown in Figure 4.15. Therefore at a given shaft angle, the entire range of forces within the area of the hysteresis envelope comprised an ensemble of possible restoring force values at that angle, depending on the motion history of each individual actuator. In light of this, the only possible course of action was to fit a curve through the center of the hysteresis area to model the restoring force, where the uncertainty on the model was the width of the hysteresis area at every point.

An experimental test was conducted in order to verify the restoring force models. In the test, the galvanometers were driven as they would be in a normal experiment for a complete uni-directional stretch of a target membrane, as described in Chapter 5. The force voltage outputs from the AE1000 amplifiers were recorded and scaled to units of force (N) according to the individual slopes calculated from plots like the one given in Figure 4.14. The force values were then corrected by subtracting the restoring forces predicted by the individual models (one per actuator) and plotted in Figure 4.16. The numerical indices in the plot indicate the finite element mesh node indices of each pulling actuator, as defined in Figure 6.1. Note that the angular excursions of each actuator are different, since one point on the membrane boundary is fixed by the clamp.

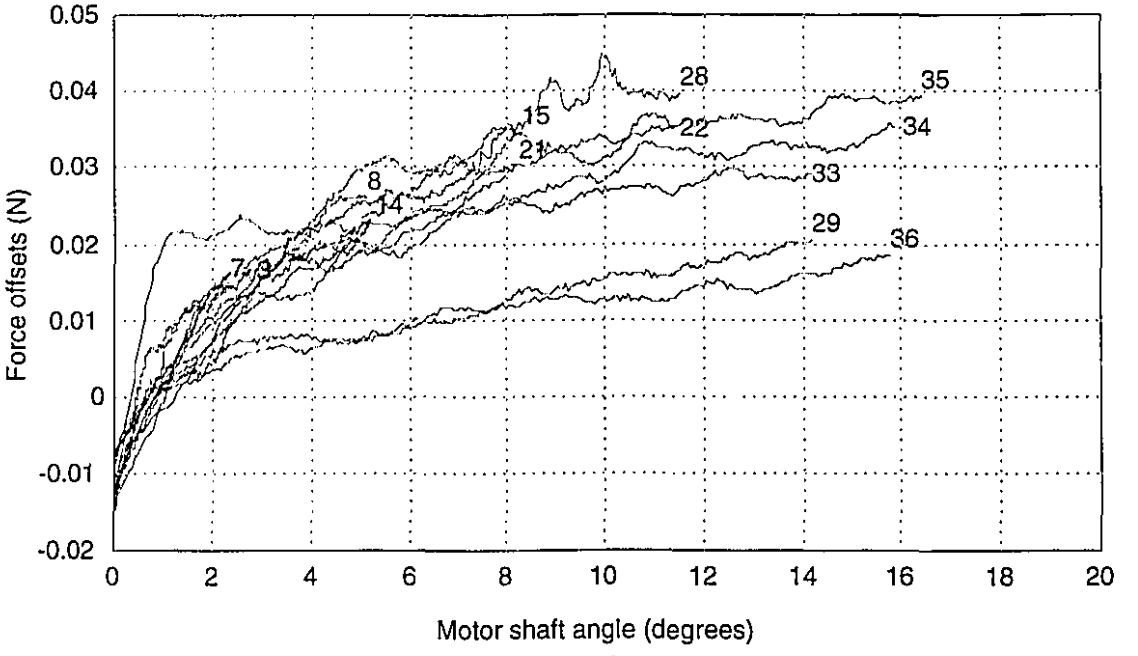

Figure 4.16: Plot showing the force residuals at each pulling actuator between the forces predicted by the model and the actual force measurements from the AE1000 outputs. The plot indicates the accuracy to which forces in the system could be measured. The numerical indices in the plot indicate the finite element mesh node indices of each pulling actuator, as defined in Figure 6.1.

As can be seen from the figure, all the residuals (differences between predicted and measured force) are lower than 50 mN. This value was thus used as a worst case noise level in the force measurements.

Chapter 5

Experimental Procedure, Raw Data Processing and Phase Unwrapping

This chapter describes the experimental procedure and the analysis of the displacement data which lays the groundwork for the finite element modeling (described in the next chapter). The first section describes the individual steps involved in the preparation and running of an experiment. In the next sections, the first stage of the speckle image analysis is described in which the raw images are processed according to the phase unwrapping algorithm to generate optical phase maps in the $[-\pi,\pi]$ range and then unwrapped to generate continuous phase maps. Finally, the last section presents force measurement results from a typical experiment.

5.1 Experimental protocol

The objective of the experiments was to stretch the target biological membrane over a large range of strain while measuring the applied forces and the resulting surface displacements in a full field manner. Ideally, the applied strains would range from an unstretched "reference" state up to large strains close to the physiological maximum.

5.1.1 Experimental constraints

There are a number of practical issues that imposed certain constraints on the different parameters under direct experimental control such as applied forces, material displacements, and maximum strain. These constraints in effect dictated the range over which these parameters were allowed to vary during an experiment. These constraints and their influence on the experimental protocol are explored in this section.

5.1.1.1 Quasi-static displacements

Because of the high spatial frequency content inherent to speckle patterns, it is crucial that the surface under test be stationary on the interferometric scale while the speckle field is being recorded. Otherwise, individual speckles in the pattern will not be completely resolved and the displacement information will be either degraded or lost. For static testing this presents no problem as the only requirement is that the material remain stable during the experiment. For a moving target however, this means that the motion must be "frozen" with a pulsed laser source and a fast gated camera. Alternatively, as in this application, displacements can be forced to occur in discrete steps interspaced with stationary periods, during which the speckle patterns are recorded. This is referred to as *quasi-static* displacements.

Phase-stepping techniques bring in an added twist to the problem in that several images of the target in a given state have to be captured. If the target motion is highly repeatable, as in vibration analysis, then each separate phase-stepped image may be acquired in a different oscillation period using a pulsed laser. For non-repeatable motion, as in transient analysis, the phase-stepped images must be acquired sequentially on a time scale very much faster than that of the target motion.

For testing of inert "robust" materials, the ideal method of measuring transient displacements using phase-stepped speckle interferometry is based on the use of a pulsed laser source. In this application however, the material under test is a highly compliant living biological membrane. For such a material, a pulsed laser may introduce additional unwanted problems such as tissue heating, vibrations due to acoustic effects and photon momentum, and ablation. Indeed, because of the transmission arrangement of this design, a relatively high power pulsed laser source would be required to offset the light losses from scattering and absorption through the target material.

Therefore, the most appropriate course of action for this first prototype was to use a low power (10 mW) continuous laser source with quasi-static displacements of the target. Hence in the experiments, displacements and forces were recorded and stored at each discrete stretch step. At the end of an experiment, the complete target motion was reconstructed from the discrete data sequence.

5.1.1.2 Maximum displacement per stretch step

Speckle decorrelation issues explained in the Section 2.3.1.1 set a practical upper bound to the largest target displacements that can be permitted between any two successive membrane stretch steps. For reasons explained below, a limit of 10 fringes was used as rough measure of the largest allowable displacement in any image. This corresponds to a maximum incremental displacement step of approximately 10 μm, or roughly $1/10^{th}$ of the decorrelation distance.

Although 10 fringes is a somewhat conservative number, it ensured that the fringe patterns were always easily resolved and could thus be successfully analyzed by the automatic analysis procedure explained later in this chapter. Indeed, as the fringe density increases, the "sharpness" of the fringe discontinuity gradients starts to erode because of speckle decorrelation. This effect makes automatic analysis more difficult. Hence although the target motion had to be broken up into a comparatively large number of steps, the resulting data sets were completely analyzed by the computer, without human intervention. Completely automated analysis is normally quite difficult to achieve in practice.

5.1.1.3 Displacement control

In classical stress/strain experiments, the input variable is normally applied force and the output variable is the resulting displacement or strain. In this application however, because of the requirements for a stable speckle pattern during recording, it is the applied *displacement* at the tether points that was the parameter under direct experimental control. The measured quantities therefore were the forces required to produce the tether point displacements and the resulting point-wise membrane displacements at all surface points. Indeed, under force control, a material may be continuously moving thus rendering the sampling of speckle fields impossible without the use of a pulsed laser and a fast gated camera.

5.1.1.4 Maximum strain

In the experiments, the target membrane was stretched up to a maximum of about 15% strain. There is evidence in the literature that the pericardium may experience even larger strains *in-vivo*, but the measurements recorded beyond this level of strain in this project were of questionable validity. Indeed, beyond 15% strain, pronounced ripping

occurred at the tether points which permanently damaged the membrane and hindered the formation of a stable speckle pattern. Furthermore, large strain concentrations were observed in the neighborhood of the tether points, possibly causing the membrane to buckle. The forces required to achieve such high strains were close to the actuator torque limits and the controlling analog servo loops had a tendency to go unstable. Therefore, 15% strain was used as a practical maximum in the experiments.

5.1.2 Experimental procedure

As explained in the previous sections. the experimental procedure was dictated to a certain extent by practical limits on certain experimental variables. The complete procedure can be summarized in the following lines. During an experiment, the membrane was stretched approximately uniformly in discrete steps from a reference "unstrained state" up to a maximum close to 15% strain. The unstrained state was defined as the membrane state for which the applied forces were just sufficient to take up the slack in the linkages. At each stretch step, the membrane diameter was increased by a maximum of 10 μm. When the target had stabilized, the eight speckle images required by the phase-stepping algorithm (4 per axis) were sampled sequentially, along with the applied forces and other parameters such as bath temperature. Details of the complete procedure are explained below.

5.1.2.1 Sample preparation

Unaltered fresh canine pericardium samples obtained from dogs which had been destroyed following experiments from other laboratories were used in the experiments described here. The samples were first carefully cleaned of fat and connective tissue using blunt instruments. Circular patches 15mm in diameter were cut from the membrane. A 10 mm diameter circle of 13 tether holes was clearly marked on the patch using a custom made punch. The patch was then mounted in the batch by attaching it with the fish hooks in the punch-marked holes.

Fine cleaning of the samples was critical to the success of an experiment, since any residual connective tissue or damaged tissue bits gently "swayed" to and fro in the liquid, due to minute mechanical noise. Although the phenomenon was not observable under white light, the motion was easily picked up by the interferometer and prevented the formation of stable speckle patterns.

The bath was filled was saline solution which had been previously degassed using an ultrasonic cleaner and a vacuum pump. The degassing was required because the heating action of the galvanometer heat pads caused gas bubbles to form inside the bath. The bubbles attached themselves to the glass window inner surfaces as well as to the membrane. Brownian motion and mechanical noise caused microscopic vibrations of the gas bubbles. This motion inside the interferometer workspace generated a high level of optical noise caused by diffraction of the laser light through the moving bubbles and prevented the formation of a stable speckle pattern. Obviously, the liquid had to be free of any foreign particles since the net effect was the same as the presence of gas bubbles.

Note that a glass window was required at the top surface of the bath. Indeed, if the laser light was allowed to go through an open air/water interface, the evaporation of the water at the interface as well as microscopic ripples on the surface would cause diffraction noise which precluded the formation of a stable speckle pattern.

5.1.2.2 Running an experiment

As explained above, the complete membrane stretch for an experiment was broken down into discrete steps, each one not exceeding displacements of 10 μm. However, because of the hole enlargement and ripping that occurred at the tether points, the actual change in membrane diameter even for a known applied stretch was highly variable. As a consequence, the number of stretch steps needed to reach the maximum strain (15%) was also highly variable. Typical experiments required in the neighborhood of 400 steps for one full membrane extension to 15% strain.

In order to minimize errors caused by thermal drift, the data acquisition time at each step had to be reduced as much as possible. For this reason, the raw data were recorded on computer disk as the experiment progressed, and only after the experiment was completed was the complete analysis undertaken. At each step, the eight 480×480×16 color images compressed to 480×480×8 (by keeping only the red component of color) were recorded, along with a small amount of data for forces and other parameters, for a total of about 2 Mbytes per step.

Each step required about 5 s execution time including sampling, saving to disk, and a 1.5 s delay to allow the membrane to settle before speckle pattern recording. Thus a

complete 400 step experiment generated about 0.8 Gbytes of raw data and ran for about 40 minutes. The major time bottleneck in the data acquisition speed was the time to acquire the eight images. Indeed although the frame grabber board could sample images 30 times per second, the data transfer rate between it and the host computer was limited to roughly 3 images per second.

Before starting an experimental run, the 13 galvanometers were carefully pretensioned "manually" to take up the slack in the linkages, using the XVG control program D/A manual interface. This membrane state was thereafter considered the "zero strain" state. Finally, the environmental enclosure was then lowered and the system was allowed to stabilize mechanically and thermally for about 30 minutes before starting an experimental run. At the end of the experiment, the phase-stepping algorithm was used to generate optical phase encoded displacement maps from the raw data sets, as explained in the next section.

During the experiments, images of the membrane under normal or "white" light were recorded every 50 stretch steps. This procedure occurred under computer control by blocking the laser light with the shutter and activating the white light source. The white light images where required for 4 reasons:

1) to verify periodically the integrity of the membrane during the experiment.

2) to provide visual measurements of hook and marker positions which were later compared to the finite element model predictions.

3) to define manually the membrane contour for the phase unwrapping.

4) to determine the orientation of the collagen fibers. This was required in the definition of the material law in the parameter estimation stage.

Note finally that, as mentioned in Chapter 1, the pericardium has a inner smooth side (serous pericardium) and a rough fibrous outer side (fibrous pericardium). In the experiments, the pericardium membrane was mounted with the fibrous side up so that the fiber orientation was clearly visible from the white light images.

5.2 Phase-stepping

The phase-stepping method used in the apparatus was the popular 4-step method shown in Table 2.1.e, with discrete optical phase delays in multiples of $\pi/2$. At each mechanical stretch step after the membrane had settled, four images were digitized sequentially in time first for the e_1e_3 plane. Between each image capture, the two glass windows in one of the interferometer arms were counter-rotated to produce the correct optical delay between the two arms, causing the speckle irradiance at each pixel to change as in Equation (2.27). Note that during rotation, the window angular velocity followed a triangular profile in order to minimize phase noise caused by "ringing" at the end of the trajectory, due to the relatively large inertia of the windows.

The plane of incidence of the laser beams onto the membrane was then shifted using the LCR and the process was repeated for the e_2e_3 plane. Hence a total of eight images were captured at each stretch step. Each set of four images is referred to as a "raw data set" in the discussion which follows. As explained in the next paragraph, the raw data sets were used by the phase-stepping algorithm in post-processing to generate "processed data sets", each one consisting of two new images: i.e.: a phase and a modulation image.

In each four image raw data set, the optical phase θ_{xy} and modulation r_{xy} were computed at every point xy with:

$$\theta_{xy} = \tan^{-1}\left\{\frac{I_4(x,y) - I_2(x,y)}{I_1(x,y) - I_3(x,y)}\right\}, \tag{5.1}$$

$$r_{xy} = \sqrt{\left[I_4(x,y) - I_2(x,y)\right]^2 + \left[I_1(x,y) - I_3(x,y)\right]^2}, \tag{5.2}$$

where $I_k(x,y)$ $(k = 1...4)$ is the measured irradiance at point xy in the k^{th} image. Since the digitized irradiance samples could only assume any one of 2^6 discrete values, both phase θ_{xy} and modulation r_{xy} values were actually determined with a lookup table that had been pre-computed using (5.1) and (5.2) with all possible values of irradiance. This process was much faster than solving (5.1) and (5.2) explicitly at each point.

A typical processed data set resulting from the phase stepping computation described above on a raw data set is shown in Plate IV. This plate gives a gray level rendering of the modulation r_{xy} (also known as the speckle *magnitude*) and phase θ_{xy} components of the speckle field across the entire target surface. Note that the raw data set consisting of four *scalar* valued images has been transformed into a *complex* processed data set which contains complete information about the speckle field at every point. The target material used to generate the data sets was a 10 mm diameter canine pericardium membrane. The lateral spatial resolution in the images is approximately 50 μm.

Note also from the phase histogram that all values of phase in the $[-\pi,\pi]$ interval are approximately equally likely, as predicted by theory. The spikes in the phase histogram are due to numerical roundoff and quantization errors in the arctan function. The largest spike at the origin is due to the large number of points of low modulation that have been discarded and set to zero (see Section 5.5.2 on phase unwrapping).

5.3 Incremental displacements

The second stage in the post-processing analysis was to subtract the phase images in successive pairs, to obtain incremental phase change maps. Indeed, one of the characteristics of speckle is that each point in the field carries with it a random phase offset. By subtracting phase images from two successive stretch steps, the random phase offsets are subtracted out and the phase differences then correspond to the relative material displacements between steps.

A typical image pair resulting from the subtraction of processed data sets is shown in Plate V (a). The two images are full field optical phase difference maps corresponding to displacements in the e_1 and e_2 axes in the plane. The abrupt dark to light transitions are the $-\pi$ to π phase discontinuities or "fringe lines". As stated earlier, each fringe line represents an approximate 1 μm in-plane relative displacement. Note that the continuous gray level change from black to white between the discontinuities represents the gradual phase change over the $[-\pi,\pi]$ interval between fringes. This is completely different from the correlation fringes which have a binary or "fringe/no fringe" appearance.

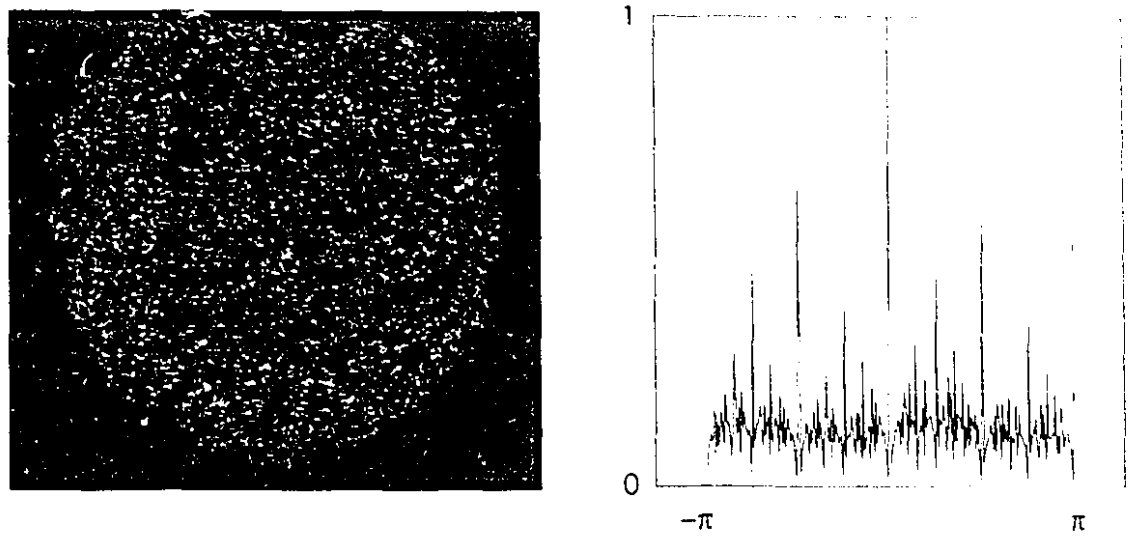

(a) Image and normalized histogram of speckle phase wrapped in the [-π,π] interval (Black pixels correspond to -π rads and white pixels correspond to π rads)

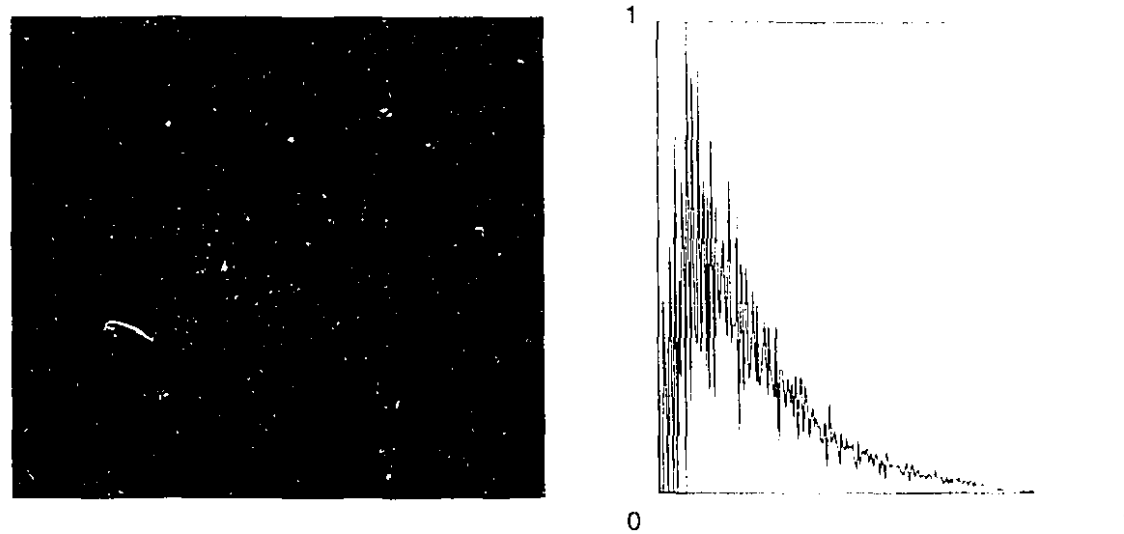

(b) Image and normalized histogram of speckle magnitude. (Black pixels correspond to values of 0 and white pixels correspond to values of 1).

PLATE IV : Typical phase and magnitude images of a speckle field computed with the standard 4-step phase-stepping method, using equal steps in multiples of π/2.

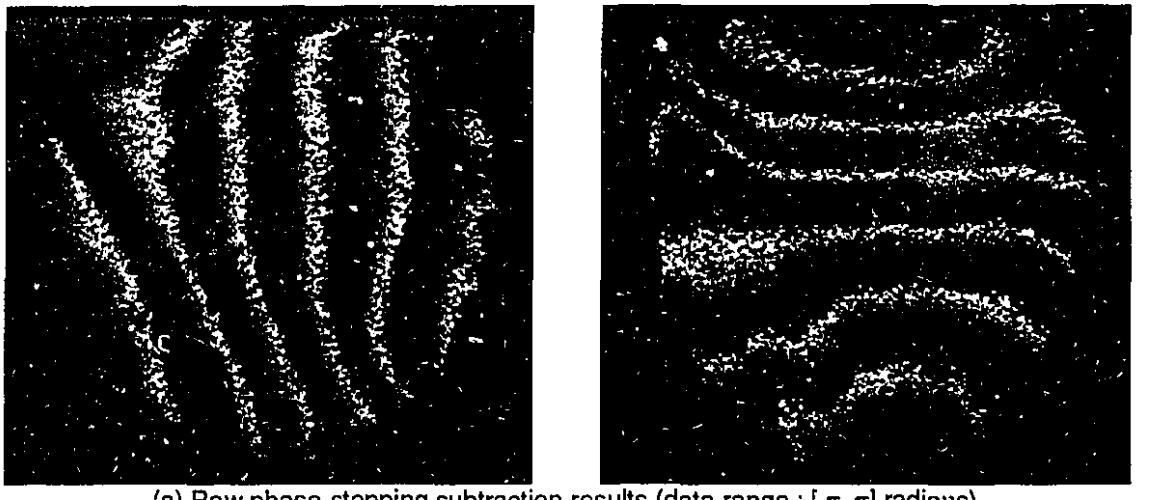

(a) Raw phase-stepping subtraction results (data range : [-π, π] radians)

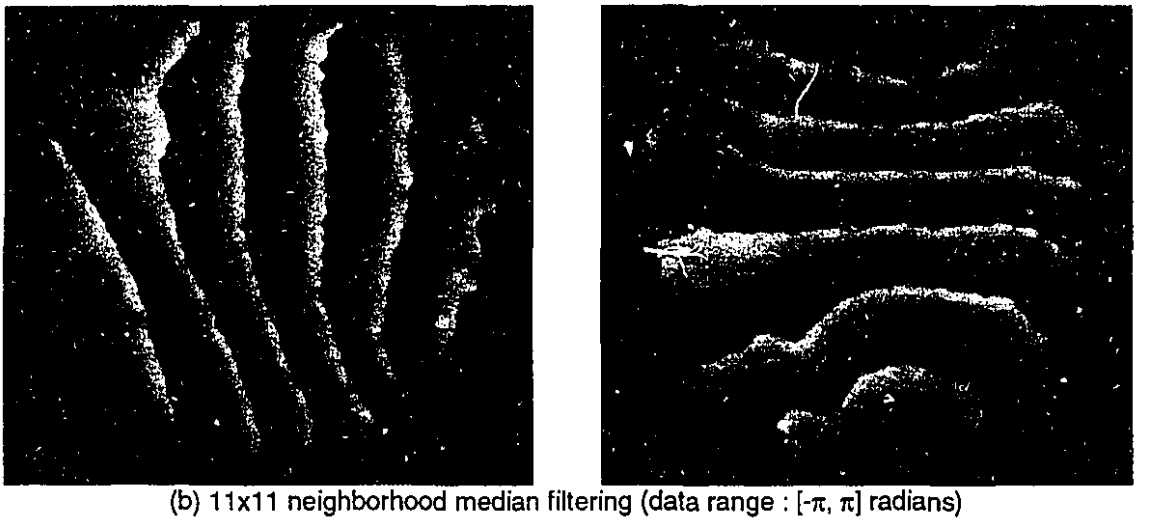

(b) 11x11 neighborhood median filtering (data range : [-π, π] radians)

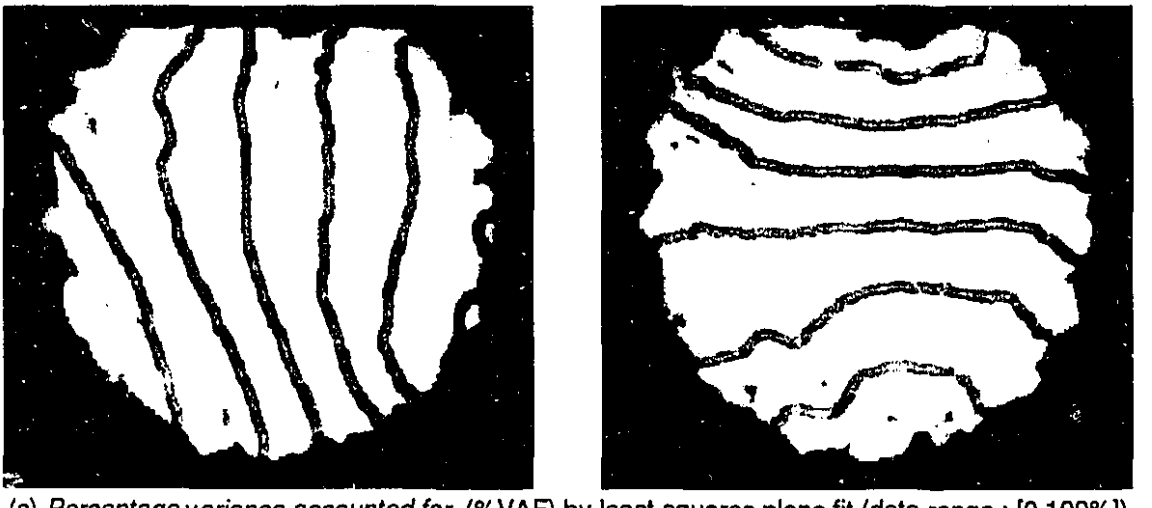

(c) *Percentage variance accounted for* (%VAF) by least squares plane fit (data range : [0,100%])

PLATE V : Typical results for the first 3 stages of the phase unwrapping process on data sets from both axes in the plane. The target material was a 10mm diameter pericardium membrane. In all images, black pixels correspond to minimum values and white pixels correspond to maximum values.

5.4 Filtering

As can be seen from the data sets in Plate V (a), speckle images are inherently noisy and a preliminary filtering step is often applied to the data to facilitate the subsequent phase unwrapping. With a few notable exceptions though, most filtering techniques recommended in the literature for use with speckle images are mainly applicable to correlation fringes. These techniques, such as *contrast enhancement* (Varman and Wykes, 1982), *squaring* and *binarizing* (Ganesan *et al.*, 1989) and others are geared towards enhancing fringe boundaries or assisting the segmentation of the image into fringe and non-fringe areas. These operations are highly non-linear as they seek to emphasize the fringe locations at the cost of distorting or simply destroying any information between the fringes. In phase-stepping images however, valuable information exists between the fringes. Indeed the fringes are merely discontinuities in the data, which are valid at every point.

However, linear filtering techniques such as neighborhood averaging or lowpass filtering in the frequency domain (Gonzalez and Woods, 1992) generally preserve the structure of the image data and reduce speckle noise, at the cost of reduced spatial resolution. In order for the filtering to reduce the speckle noise by an appreciable amount however, the high spatial frequencies which contribute to the sharpness of the fringe transitions are also diminished. For example, in one dimension, phase stepping fringes have a "sawtooth" profile corrupted with high frequency noise (speckles). By applying a lowpass filter to remove the noise, the vertical discontinuities in the sawtooth are dulled and rounded. Hence not only does this distort the data in the fringe neighborhoods, but algorithms which rely on sharp edges to locate fringes are adversely affected.

However, when the fringe density is moderate and the speckle size is very small, the spatial frequencies of speckles and fringes can be fairly well separated in the frequency domain. In this case, spatial frequency domain filters can be helpful. Indeed Kerr *et al.* (1989) present impressive results of speckle noise reduction by using a hand drawn optimal mask for frequency domain filtering. They further improve the quality of the image by tailoring the filter to eliminate the DC component and any low frequency trend resulting from uneven illumination or target reflectivity.

5.4.1 Median filtering

A filter which has met which great success in speckle metrology is the non-linear *median* filter. This technique is a so-called *neighborhood* or *kernel* filter as each pixel in the image is replaced by a function of the neighboring pixels. In the median filter, all pixel values in an $N \times N$ neighborhood about a central pixel are sorted in non-decreasing order. The center pixel value is replaced with the median of the sorted array, i.e.: the value at index $N^2/2$. Frieden (1991) presents an interesting study of the properties and statistics of a length N one-dimensional median filter, which readily extends to two dimensions. Some properties of this filter are:

(1) Random fluctuations over constant regions are reduced.

(2) Edge gradients are passed unaltered.

(3) Features which consist of a point spread function which extends over $(N+1)/2$ points or less across a constant background are obliterated.

(4) Features which are monotonic over N points or more are passed unaltered.

Properties (1) and (2) are particularly relevant in the case of phase-stepped speckle images, since it means that the median filter reduces speckle noise while keeping the fringe gradients unaltered. For this reason, this filtering method was the only one chosen as a preliminary processing step before the phase-unwrapping. A typical result is shown in Plate V (b) which resulted from the application of an 11×11 median filter to the images in Plate V (a).

The appropriate size of the filter neighborhood was chosen by considering two competing criteria, namely the noise reduction power versus the preservation of fringe integrity. Indeed, small kernels (e.g., 4×4) had a mild effect on the noise while leaving the fringe gradients largely unaffected. Larger kernels (e.g., 20×20) had a dramatic noise reduction effect but caused erosion of the fringe gradients. To provide an objective rating of the noise reduction power of various kernel sizes, a test experiment was conducted where two phase stepping data sets where acquired from a fixed target and subtracted. The experiment thus yielded a null result, or a mild offset due to thermal drift, overlaid with speckle noise. The standard deviation (SD) of the filtered data was used as measure of filter noise reduction.

It was found that the SD of the filtered data dropped off rapidly for small kernels but leveled out at about 1/4 of the raw data SD, for kernel sizes of about 11×11. Neighborhood size increases beyond this point produced steadily improving but less dramatic results. Hence 11×11 was chosen as an optimal kernel size, with the constraint that image features (namely the inter-fringe interval) had to be kept larger than twice the kernel width, or 22 pixels. This criterion set a practical upper limit for the fringe density of about 22 fringes/image in a 480 pixel frame. In practice, it was found that fringe gradients started to show signs of degradation at half this number, so that the 10 fringes/image limit arising from correlation issues explained earlier was ideal for this kernel size.

5.5 Phase unwrapping

The final stage in the analysis of the displacement data prior to the finite element modeling, is the unwrapping of the phase from the $[-\pi,\pi]$ interval to the $[-\infty,\infty]$ interval. This problem is found in many areas such as classical interferometry, holography, Moiré interferometry, synthetic aperture radar interferometry, and of course speckle interferometry.

Surprisingly, even though phase-unwrapping of two dimensional data sets has been and still is a very active area of ongoing research (as demonstrated by the recent references quoted below), there exists, as of yet, no completely automatic solution for general applications with high noise content. Several methods have been proposed in the literature and they are surveyed in this section. Their respective deficiencies are pointed out.

Therefore, in the course of this project, a novel method of phase-unwrapping was developed. It was designed specifically for the case of noisy speckle images with arbitrary fringe patterns and it is described below. Unlike existing methods, it is sufficiently robust to render the analysis of speckle images completely automatic.

5.5.1 Review of current methods

The classical method of phase unwrapping is simply an extension of the basic one-dimensional idea. Horizontal lines in an image are unwrapped separately by scanning pixels from beginning to end. Along any one line, a running offset is added to each pixel. The offset is incremented or decremented by 2π whenever the difference between two

successive pixels exceeds a threshold such as $\pm\pi$. Once all horizontal lines have been unwrapped, they are connected vertically by unwrapping along a single column to determine any 2π offsets between vertical lines.

This method is only suited to noise free data sets however, such as in classical interferometric curvature and flatness testing of specular optical elements with smooth wavefronts. Indeed any noise in the image which would either cause a 2π discontinuity to be missed or a spurious one to be created generates an error which will propagate through the unwrapping process. Hence local errors become global ones. Moreover, the errors will be path dependent, as the direction of error propagation depends on the unwrapping order, path and direction. The classical method is normally also limited to simple shapes, although modifications can be made to accommodate more complex geometries (Stetson, 1992).

Current unwrapping methods vary in their degree of operator independence and most require some degree of human assistance at various stages in the procedure. Few methods claim to be completely automatic. Most current methods of phase unwrapping fall into one of two categories:

I- Methods which detect the position of edges or abrupt phase discontinuities (fringe lines) in the images and use this information to calculate the running phase offsets with the classical unwrapping method.

II- Methods which seek to identify and isolate areas in the image which would cause propagating errors and exclude them from the unwrapping process. The unwrapping can then proceed along any arbitrary path. These methods ultimately seek to make the unwrapping unique and path independent.

Standard image processing edge detection methods (Gonzales and Woods, 1992) have been used in applications based on type I. More advanced general edge detection algorithms have also been used such as the "Canny optimal edge filter" proposed by Canny (1986) or a modification of the Canny filter for ramp edges proposed by Petro and Kittler (1991).

Several other "custom" varieties of type I methods have been proposed in the literature with differing ways of tracking fringes. Button *et al.* (1985) proposed a method to identify correlation fringes by moving along the path of minimum irradiance, starting with a manually specified initial point and direction. Krishnaswany (1991) proposed a slightly more advanced method where fringe lines are followed by tracking points which maximize

the second derivative of the direction normal. Sirkis *et al.* (1992) employed a simple edge following algorithm which relied on the image having been previously binarized. Ramesh and Pramod (1992) proposed a fringe thinning algorithm to generate a skeleton image used to identify manually the fringe order. Finally Lin *et al.* (1994) proposed a method of edge detection by convolving the image with standard gradient masks, and subsequently linking edge segments together to form complete fringe skeletons. They also proposed a method of least squares fitting of various basis functions to identify fringe lines, after the image had been segmented into subregions containing one fringe each. They did not however demonstrate a convincing method of segmenting the image.

In early experiments in this project, it was found that phase unwrapping algorithms based on type I methods worked well only with very low noise levels and as such were not particularly well suited to speckle images. Indeed, the edge following algorithms will track most of the fringes with varying degrees of success, but edges will inevitably be fragmented by the slightest noise in the image. Automatically linking edge fragments into continuous edges is then a difficult procedure which is quite prone to error. Any gap in the fringe lines that has been left open, as well as spuriously created edges, then cause global errors in the unwrapping process. Generally, edge detection based methods are not fully automatic and usually involve a fair amount of customization and tinkering with particular data sets.

On the other hand, the type II phase-unwrapping methods are more robust as they are based on an underlying physical property of the data sets. The assumption here is that the phase unwrapping result must be path independent and that any integration along an arbitrary closed path in the image must yield zero. The basic concept of a "residue" is defined in this context as the result of integrating the phase along a closed path of four neighboring pixels arranged in a 2×2 square. Non-zero residues are termed "positive" or "negative" depending on the sign of the resulting integration. It can be shown (Goldstein *et al.*, 1988) that integration along an arbitrary closed path containing a single non-zero residue produces a global inconsistency in the unwrapping. It can also be shown that if a path contains an equal number of positive and negative residues, no inconsistencies result.

The objective is then to prevent phase unwrapping paths from segmenting the image into regions which contain unequal numbers of positive and negative residues. Goldstein *et al.* (1988) and more recently Huntley (1989) achieved this by defining "branch cuts"

linking positive and negative residues, which any unwrapping path was then forbidden to cross. The problem then became that of finding the optimal network of branch cuts between residues. Bone (1991) produced an improved algorithm which produces a mask of invalid pixels based on second differences in the locally unwrapped phase, instead of branch cuts. In both cases, the phase unwrapping then follows in a "flood fill" manner (Foley *et al.*, 1990).

Another type II unwrapping method proposed by Ghiglia *et al.* (1987) uses a cellular automata to unwrap the phase once invalid pixels in non-zero residues are masked out. This technique however is computationally very intensive and basically achieves the same results as those mentioned above (Bone, 1991). The authors cite the results of an experiment conducted on a synthetic noise-free data set which required 710 iterations of the automata across the entire image to unwrap the phase!

Type II methods, although much superior to type I methods, still seem to perform poorly in the presence of high levels of noise. Indeed, Lin *et al.* (1994) concede that there are so many branch cuts generated for noisy data sets with the method proposed by Goldstein (1988) that the results become unusable. Bone (1991) states that his method can tolerate a 2:1 signal-to-noise ratio, where the noise level is at most half the fringe amplitude. This is certainly not the case for raw speckle data. If pre-filtering is applied to the speckle data in order to reduce sufficiently the noise, the fringe gradients are also slightly reduced in the process. Unfortunately, type II methods rely on infinitely sharp phase discontinuities. Hence any form of filtering that adversely affects the fringe gradients will cause the type II unwrapping algorithms to fail. Note that in practice, although the median filter is the least damaging to edge gradients in an image, some erosion of the gradients will nevertheless occur for any practical kernel size. In the experiments, even the slight degradation of edge gradients by median filtering was found to impair the operation of type II algorithms.

Huntley and Saldner (1993) proposed a "temporal" rather than spatial unwrapping method. The idea here is that surface displacements of the target are constrained in such a way that no fringe discontinuities appear in any one image. This is achieved by breaking down the measurements into a series of incremental displacement images, instead of one single sample that might contain discontinuities. The phase is then unwrapped "through time" at each pixel individually in the image sequence. Hence phase unwrapping errors do

not propagate to neighboring pixels. This method is not practical for large displacements however since incremental displacements must be constrained to less than the fringe sensitivity. In the present application for example, a 1.5 mm displacement would require 1500 individual steps, with a total of 12000 images captured for the complete phase stepping process.

Finally, Gierloff (1987) proposed an interesting method of phase unwrapping by regions. In this method, the image is segmented into separate regions which contain no phase discontinuities. The regions are then phase shifted with respect to each other to eliminate the phase discontinuities. Unfortunately, this method also relies on infinitely sharp edge gradients and seemed to fail even in mildly difficult situations. The author states further that the failures are somewhat surprising and that their causes are not well understood.

5.5.2 Novel phase unwrapping method for images with a high noise content

As explained above, no current unwrapping method appears to be well suited to automatically unwrapping phase-stepped speckle images. An attempt was hence made in this work at developing a new robust method of phase unwrapping. Although the method is conceptually similar to that proposed by Gierloff (1987), it proceeds entirely differently and was developed completely independently.

As with Gierloff (1987), the method described here is also based on segmenting the image into areas between fringes and then computing the phase offset between the disjoint areas. Both methods use reverse logic in the sense that they seek not to identify fringes, but to locate regions without fringes, on the assumption that this is an easier task. In the Gierloff (1987) method, image segmentation is based on a simple system of thresholds, where pixels in an image are assigned to specific regions by comparing their value to that of their immediate neighbors. As stated above, the successful application of this algorithm relies on infinitely sharp fringe gradients and low levels of noise. However, both conditions are difficult to achieve with speckle images. In the method proposed here, as explained below, the segmentation algorithm is much more robust and well suited to speckle images.

The proposed unwrapping method can be summarized in the following 5 steps, which are explained in more detail afterwards:

I- A new image is generated from a phase subtraction image where for each pixel in the image, a plane is locally fitted using least squares to a $k \times k$ neighborhood centered on the pixel. The *percentage variance accounted for* (%VAF, see Equation 5.9) by the fit is stored at the center pixel location.

II- Using the histogram of the %VAF data set, a threshold is computed to binarize the image into pixels where the plane fit is good (most of the image) and where the fit is poor (the phase discontinuities, theoretically, and high noise areas in the image).

III- All disjoint regions in the image where the fit is good are flood filled with a distinct index value. The regions are then expanded uniformly until they touch and all pixels where the fit was poor are covered.

IV- The relative offsets between regions sharing a common border are calculated by taking the average value from samples taken at regular intervals along the border.

V- Absolute offsets are calculated for all regions in the image by building a stack of regions and traversing it in order of decreasing region size.

VI- The original phase image is unwrapped by adding to it the absolute offset image generated in step V.

As stated above, the fundamental concept behind this method is the identification of contiguous areas which are *not on or close to a fringe*. Hence when locally fitting planes to the data, the fit will be good in regions where there are no phase discontinuities present in the domain, and poor elsewhere. The assumption here is that the curvature due to true phase gradients in the data is much lower than that due to phase discontinuities. This assumption is valid if the fringe density is moderate, if there are no true discontinuities in the target (such as a step profile or a hole), and if any filtering applied to the data does not unduly reduce the discontinuity gradients. Unlike existing phase unwrapping methods, this new method is fairly tolerant of edge gradients that have been moderately degraded by filtering.

Note that for this process to work, the fitting domain must be wider than the distance over which a phase discontinuity goes from its minimum to its maximum value. Theoretically this distance should be zero, but due to finite instrument bandwidth and filtering artifacts, this distance is in fact finite.

A plane can be described by all points v (x,y,z) which satisfy:

$$\bar{n} \bullet \bar{v} = d \quad or \quad n_x x + n_y y + n_z z = d, \tag{5.3}$$

where $n(n_x,n_y,n_z)$ is a unit vector normal to the plane and d is the distance from the origin to the plane in the normal direction. With a simple change of variable in (5.3), the plane model can be expressed more conveniently as:

$$\hat{z} = u_1 + u_2 x + u_3 y, \tag{5.4}$$

where the u_k (i =1...3) are the model parameters and $\hat{z}$ is the model estimate of the actual data value z. The plane model is fitted to data values in a $k \times k$ domain centered on pixel p_{ij} by the method of *weighted least squares* (Press *et al.*, 1992). The model is determined by minimizing R_{ij}, the weighted sum of squared residuals $(z - \hat{z})^2$, with respect to the model parameters:

$$\frac{dR_{ij}}{du_n} = 0, \quad n = 1...3, \tag{5.5}$$

where:

$$R_{ij} = \sum_{x=-\frac{k}{2}}^{\frac{k}{2}} \sum_{y=-\frac{k}{2}}^{\frac{k}{2}} \left(z_{i+x,j+y} - \hat{z}_{i+x,j+y} \right)^2 w_{i+x,j+y}, \tag{5.6}$$

and where the w are the data weights which are defined below.

The minimization yields a set of 3 simultaneous equations in the model parameters, the so-called *normal* equations:

$$\underbrace{\begin{bmatrix} \Sigma w & \Sigma xw & \Sigma yw \\ \Sigma xw & \Sigma x^2 w & \Sigma xyw \\ \Sigma yw & \Sigma xyw & \Sigma y^2 w \end{bmatrix}}_{A} \underbrace{\begin{bmatrix} u_1 \\ u_2 \\ u_3 \end{bmatrix}}_{u} = \underbrace{\begin{bmatrix} \Sigma zw \\ \Sigma xzw \\ \Sigma yzw \end{bmatrix}}_{f}, \tag{5.7}$$

where the summing indices have been omitted for purposes of clarity. Henceforth, the tensor summing convention will be used, where summation over repeated indices in any

term is implied. The normal equations matrix system can thus be expressed more succinctly as:

$$A_{mn}u_n = f_m, \quad n = 1...3, \quad m = 1...3. \tag{5.8}$$

Once the model parameters have been estimated, the *percentage variance accounted for* $\%VAF_{ij}$ is used as a measure of goodness of fit:

$$\%VAF_{ij} = 100\left(1 - \frac{(z_{lm} - \hat{z}_{lm})^2 w_{lm}}{z_{vw}{}^2 w_{vw}}\right). \tag{5.9}$$

Hence in the first step of the phase-unwrapping process, an image is generated by computing the goodness of fit measure $\%VAF_{ij}$ at every point p_{ij} in the image, for a local plane fit over a $k \times k$ square domain centered on p_{ij}. Note that the fitting occurs on $k \times k$ square domains centered at every pixel in the image, i.e.: the domains overlap, they are not tiled.

Initially, the speckle modulation values r_{ij} computed with (5.2) were used as the weights w. As mentioned above, the phase and modulation were determined at each point in the image with a lookup table, which was pre-calculated using (5.1) and (5.2). Lookup table entries for which (5.2) yielded modulation values at or below the frame grabber A/D noise level (i.e.: points of low modulation) were simply set to zero. Similarly, pixels for which any one of the four irradiance samples I_k was equal to the frame grabber A/D maximum value were considered to be saturated. Lookup table entries for such points were also set to zero. Therefore, points of low modulation and saturated points were excluded from the fitting process by having zero weight.

Subsequent analysis experiments were performed slightly differently by applying the plane fitting process to a median filtered data set, as opposed to the raw phase data. In this case, since the data had undergone a non-linear transformation, the weighting method as described above was no longer appropriate, and hence the weights were simply set to 1 as in the method of *regular* or *uniform* least squares. As a result, the fitting process was sped up considerably. Indeed, the matrix A now became identical for each domain and could thus be precomputed. Moreover, because of the equal weights, six out of the nine components in the matrix were equal to zero.

Not only was this variant of the plane fitting process faster, but it also surprisingly yielded better segmentation results than the weighted least squares approach. Results of the plane fitting process on the median filtered data of Plate V (b) are shown in Plate V (c). In the images, the $\%VAF_{ij}$ values at every point are gray level encoded (i.e.: black pixels correspond to 0% VAF, whereas white pixels correspond to 100% VAF).

Once a %VAF image had been generated, it was binarized to values of 0 or 1 with a threshold determined by using the histogram of the data, as shown in Figure 5.1. The objective was to segment the image into areas where the local plane fit was "good" and areas where the local plane fit was "poor". The threshold was set to the value marking the beginning of the steep rise at the end of the probability density function (in this case 95%), on the assumption that most of the pixels in the image were not on or near a fringe. Results of the binarization process are shown in Plate VI (d).

The main type of errors which occurred in the steps described above were referred to as "bridges", where noise in the data caused erroneous links between regions that should have been disjoint. In this case, the subsequent analysis steps in the algorithm would fail by coalescing both regions into a single one. This problem was however simple enough to fix. Experiments showed that such false "bridges" where always much thinner than the inter-fringe interval width, for moderate fringe densities. The bridges could thus be eliminated by using the binary morphological operation of *opening*, where the image was first *eroded* and then *expanded* by a circular structuring element (see Dougherty (1992) or Gonzales and Woods (1992), for a description of morphological image processing). In later experiments with this apparatus however, the quality of the data was such that this correction process was not required.

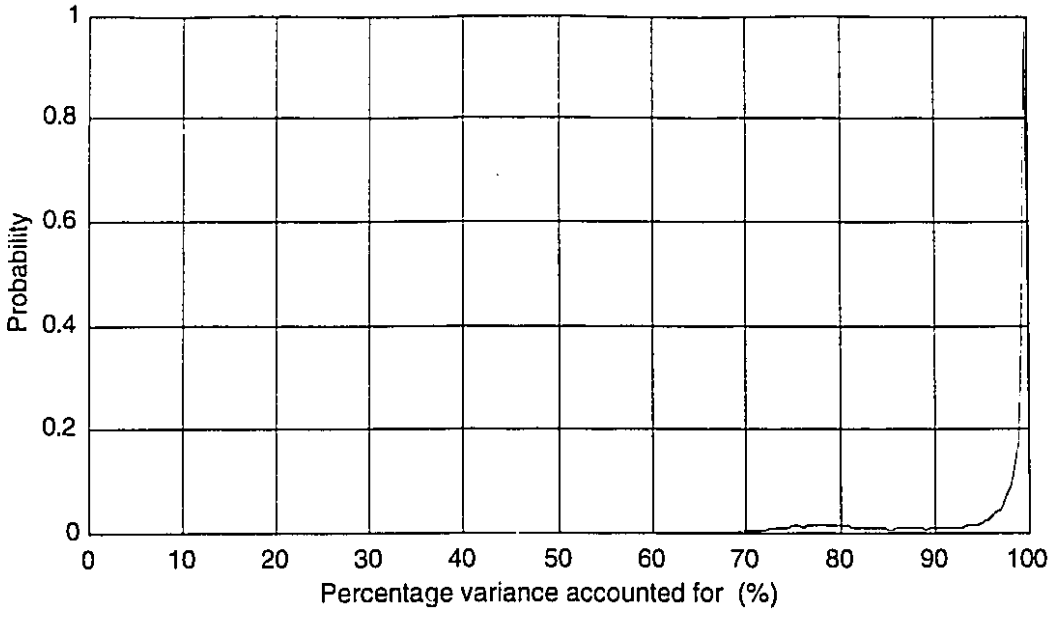

Figure 5.1: Probability density function of the *percentage variance accounted for* (%VAF) by the local fitting of plane models to the median filtered phase-stepping subtraction data.

After the images were binarized, all disjoint non-zero regions were tabulated and identified with a unique index. This process was accomplished by scanning the image by line and whenever a pixel with a value of 1 was encountered, it was used as the seed for a flood fill operation (Foley *et al.*, 1990) with a new unique index. Once all non-zero regions had been indexed, they were expanded until they touched and all zero pixels were covered. A simple method of expansion was used where regions were expanded cyclically adding in turn a one pixel deep layer in the four cardinal directions, until there were no zero pixels left.

The image generated by the filling and expanding process described above was used as a template to identify inter-fringe regions in the median filtered phase images. The assumption here was that the region boundaries would now correspond closely to the fringe lines. The relative phase offsets between all regions sharing common boundaries were then calculated using a process described in Figure 5.2.

(d) Binarized %VAF data sets (data range : 0 or 1)

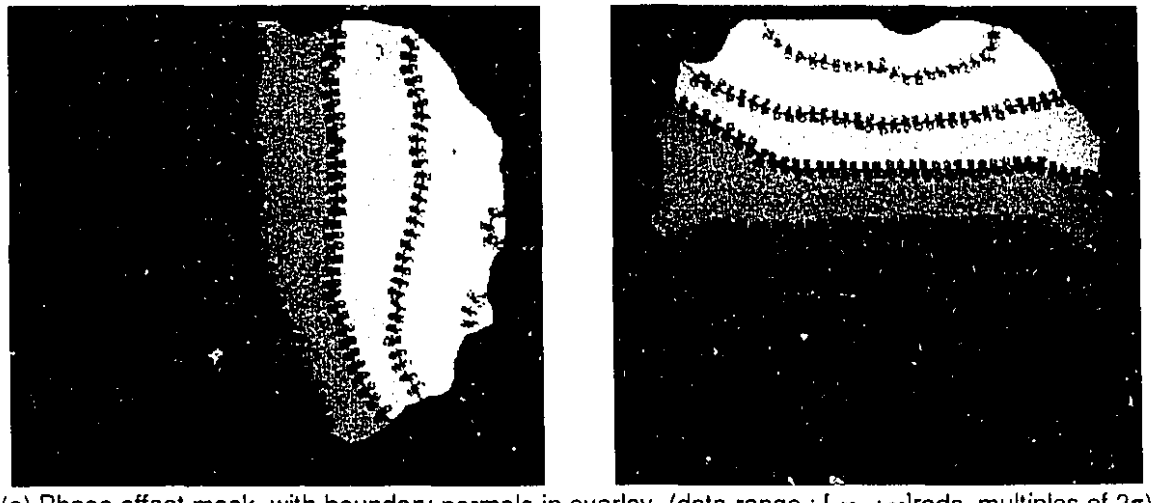

(e) Phase offset mask, with boundary normals in overlay (data range : [-∞, +∞]rads, multiples of 2π)

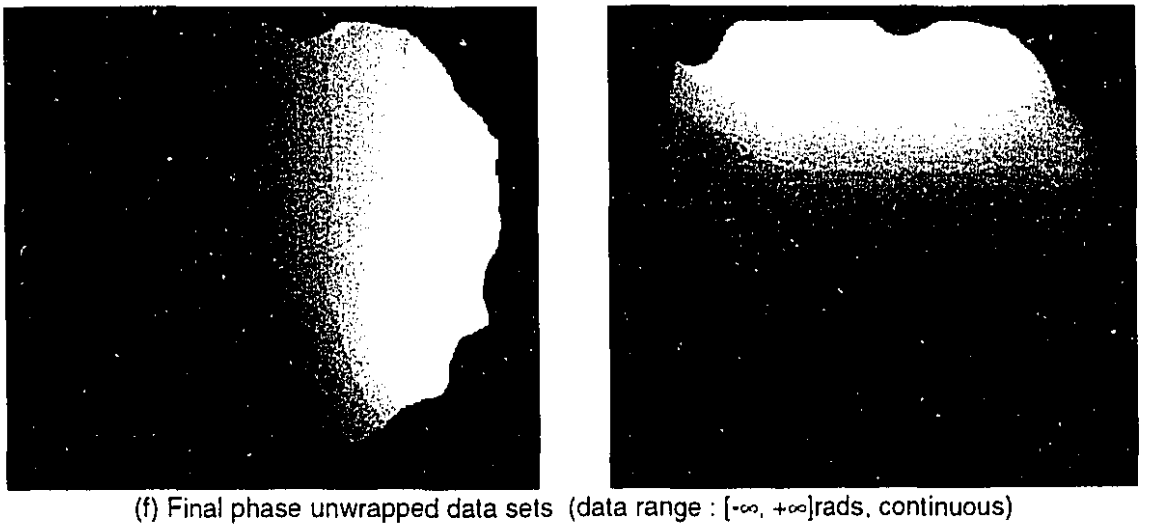

(f) Final phase unwrapped data sets (data range : [-∞, +∞]rads, continuous)

PLATE VI : Typical results for the last 3 stages of the phase unwrapping process on data sets from both axes in the plane. The target material was a 10mm diameter pericardium membrane. In all images, black pixels correspond to minimum values and white pixels correspond to maximum values.

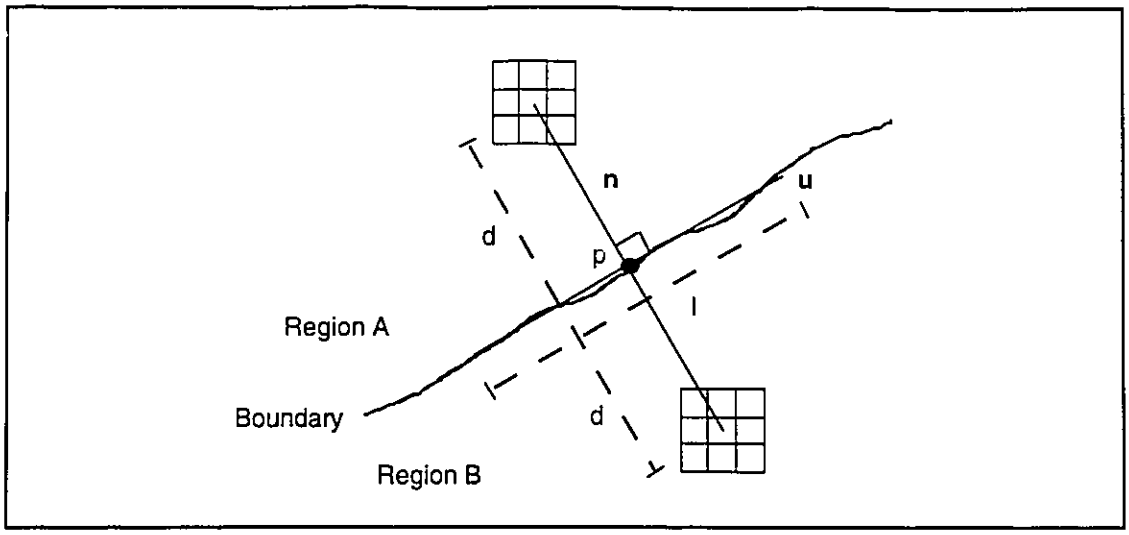

Figure 5.2: Relative phase offset between two regions calculated from the difference of the average phase values in 3×3 square areas at equal distances on either sides of the boundary.

The relative phase offset between two regions sharing a common boundary was determined by considering the average of phase differences at regularly spaced points, p, at intervals, l, along the length of the boundary (see Figure 5.2). To calculate each phase difference sample at p, a straight line, $\boldsymbol{u}$, was locally fitted to the boundary using least squares, and the corresponding normal, $\boldsymbol{n}$, through p was determined. The local phase difference was calculated by subtracting the average phase values in 3×3 square neighborhoods, at equal distances, d, from p along the normal.

The reason for using the elaborate system shown in Figure 5.2 over the more conventional method of simply averaging the difference between pixel values on either side of a boundary is the following: when discontinuity gradients are not infinitely sharp (because of filtering artifacts for example), the pixel values in the immediate vicinity of the boundary many actually be quite similar. Using the system described in Figure 5.2 however eliminates this problem as any "rounded edges" are circumvented by adjusting the parameter d accordingly. Hence this system is immune (within practical limits) to fringe degradation by filtering and is hence much more robust that conventional methods which rely on infinitely sharp gradients.

The average offset, o, (taken from many samples p at intervals l) between any two regions was compared to a threshold, t, and one of three actions was taken:

(1) $o >= t$: Relative offset = 2π.

(2) $o <= -t$: Relative offset = -2π.

(3) $-t < o < t$: Combine both regions.

Hence either a relative $\pm 2\pi$ offset was assigned to the boundary, or the regions were considered to have been erroneously segmented, perhaps as a result of high local noise, and were thus recombined. Optimal values for the parameters l, d and t were determined manually with early experimental results and subsequently "hard coded" into the analysis program. The values were dependent on maximum fringe density, the distance over which the phase discontinuities went from minimum to maximum, and any artifacts caused by filtering. Since these properties were fixed across experiments once the analysis process had been debugged and validated, the l, d and t parameters were effectively considered constants.

After relative offsets had been determined for all inter-region boundaries, absolute offsets were assigned to each region by using an algorithm based on a region stack. Starting with the largest region in the image (which had its offset arbitrarily set to zero), the absolute offsets for all its neighbors were set and they were pushed onto the stack. The largest region on the stack was then popped and all its unmarked neighbors were pushed onto the stack, after their absolute offsets had been set. The process continued, with consistency checks at each step, until the absolute offsets for all regions had been determined. It was found that traversing the stack in order of decreasing region size reduced the likelihood of inconsistencies appearing in the process, as the pieces of falsely segmented regions were smaller on average and were traversed last.

This stage terminated by generating an "offset mask image", where each region was flood filled again, but this time with the value corresponding to its absolute phase offset, in multiples of 2π. The results of this process are shown Plate VI(e), where the region indices and the boundary normals used in the phase difference computation are shown as an overlay.

The final stage in the unwrapping process was simply to add the offset images to the median filtered phase images, as shown in Plate VI(f). Note that artifacts at the fringe lines due to median filtering edge degradation can be seen in the unwrapped images. The artifacts did not need to be removed by an additional filtering operation since they were naturally smoothed out in the least squares fitting of the finite element model, described in Chapter 6. The fringe lines identified by the unwrapping process are shown overlaid onto the raw and median filtered data sets in Plate VII (a) and (b). It can be seen from the images that the fringe lines correspond well to the phase discontinuities, except at a few places near the boundaries where the noise is particularly severe.

It must be stressed again that this entire procedure is fully automatic and executes without operator intervention. This situation is rarely achieved in practice if at all with existing algorithms. Given the large number of images involved in a typical experiment, the success of the automation process was critical to the practical usability of this method.

Note finally that the five steps in the phase unwrapping procedure outlined above were performed on image pixels within a defined contour. Indeed, as the membrane was circular and the CCD field of view was rectangular, there were many pixels contained in the image which were outside the membrane boundary. In order to keep total processing time to a minimum, non-membrane pixels were excluded from the unwrapping procedure by the object contour.

Initially, the object contour was defined automatically by the analysis program for each image using morphological operations. Although this process was highly successful, it was also very time consuming. The phase unwrapping analysis time was reduced substantially by pre-defining the contour manually. This process was actually much simpler than it sounds. Indeed, since the apparatus was sensitive to minute displacements in the target membrane, the pixel area covered by the membrane image changed very little between each stretch step. As a result, a contour which was defined from a particular membrane image was still valid for computations in several images afterwards.

Hence, the strategy adopted here was to pre-define manually a set of membrane contours increasing in size, by tracing the membrane outline in the white light images with a mouse. Since the white light images where captured every 50 stretch steps, thisinvolved tracing six to eight membrane contours by hand, a fairly quick and easy task.

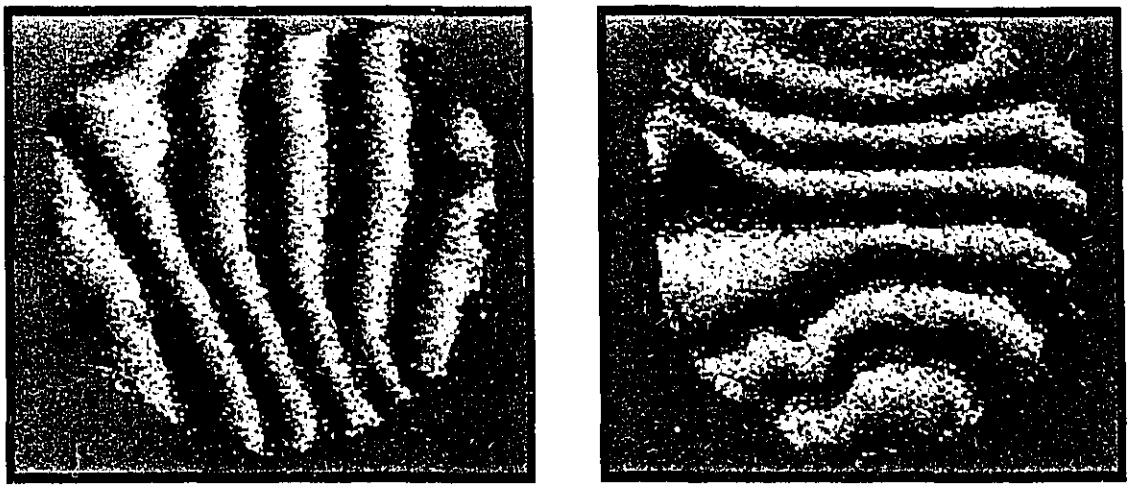

(a) Raw phase-stepping subtraction data, with fringe lines in overlay (data range : [-π, π] radians)

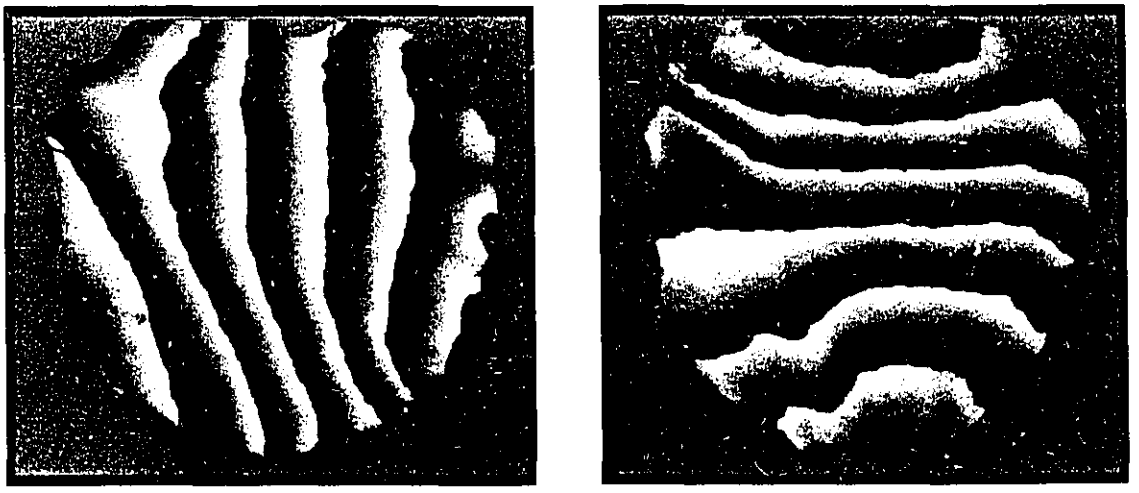

(b) Median filtered data, with fringe lines shown in overlay (data range : [-π, π] radians)

PLATE VII : Typical results for the first 2 stages of the phase unwrapping process on data sets from both axes in the plane. The phase discontinuities (fringes) computed in the subsequent unwrapping stages are shown as an overlay. In all images, black pixels correspond to minimum values and white pixels correspond to maximum values.

The contour definitions were then loaded by the XVG program, prior to the analysis. It must be emphasized however that given sufficiently powerful computer resources, this process would also have been completely automated.

The phase unwrapping process for one phase difference image ran for about 4 minutes on average, on an IBM RISC/System 6000 workstation with 16 megabytes of RAM (the running time was highly dependent on the amount of available memory). The XVG control program also included functionality which enabled it to distribute the processing workload on other workstations across the network. Hence for a typical experiment yielding roughly 400 image pairs, the total running time on 10 workstations (executing 40 Mflops each) in parallel was about 5 hours.

5.6 Force measurements

Forces applied at the tether points by the pulling actuators were determined indirectly from measurements of the AE1000 force voltage outputs, at each stretch step in the experiments. A typical force measurement result is shown in Figure 5.3 below.

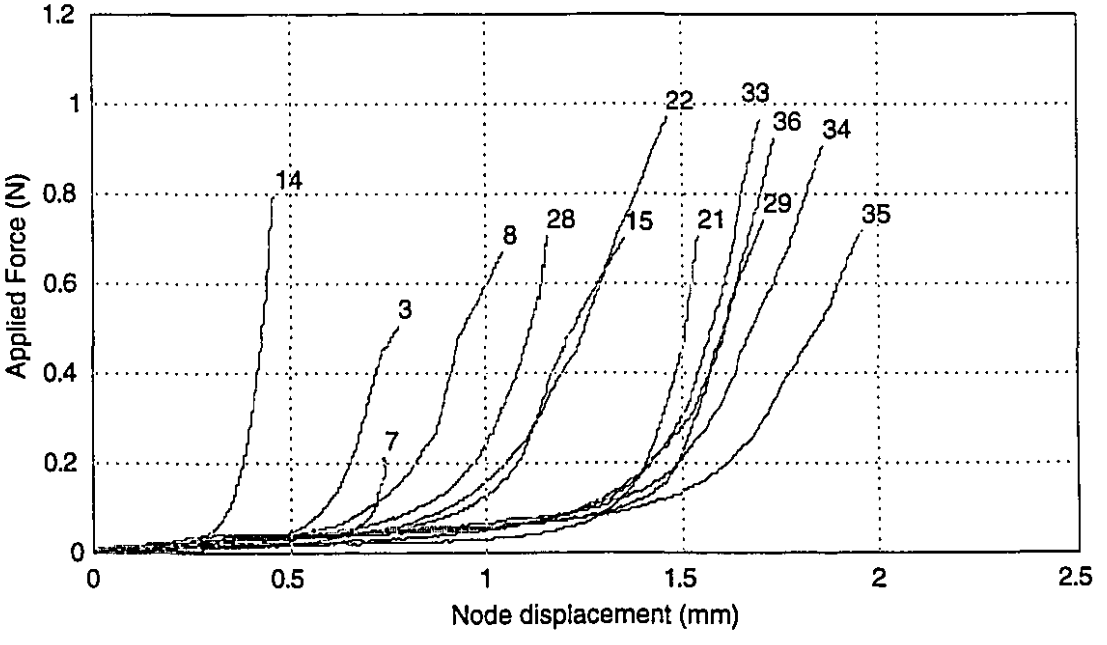

Figure 5.3: Typical plot of applied forces at the 13 tether points around the membrane for a complete stretch experiment. The numerical indices in the plot refer to the finite element mesh boundary node indices, as shown in Figure 6.1.

Raw voltage measurements from the amplifier outputs were scaled to units of force and corrected for restoring force offsets using the calibration procedure results explained in Section 4.2. Note that the curves corresponding to each of the 13 tether points are identified by their respective finite element node indices, as defined in Figure 6.1. Recall that the noise level on the force measurements was 50 mN, as explained in Section 4.2.

Chapter 6

Finite Element Modeling and Analysis

This chapter describes the various steps in the finite element modeling and analysis of the experimental data. The first sections explain the basics of the finite element method and describe how it is used for distributed representation of the experimental displacement data. The finite element data representation is then employed to calculate the full finite strain tensor field across the entire membrane surface, at various stretch states. Finally, results are presented where the finite element method is used for distributed parameter estimation in order to characterize and quantify the membrane material properties.

6.1 Finite element data representation

One of the most challenging aspects of this project was to develop an appropriate method of analyzing the large volume of data generated by the experiments. The experimental data contains information about the magnitude, direction, and spatial distribution of the displacement field, and hence reflects the *distributed* characteristics of the material under investigation. Furthermore, not only do the data contain intricately detailed information from each stretch step, but also the data set ensemble from the entire experiment must somehow also be coherently linked into one consistent sequence through time. Indeed, the data acquisition is only half the problem since even the best quality data is of limited use if there are no methods of drawing useful conclusions from it.

It would seem logical then to make use in the analysis of the premier numerical analysis tool for *distributed* or *continuum* modeling: the *finite element method* (Zienkiewicz and Morgan, 1983). Normally, the finite element method is used to solve problems numerically over multi-dimensional domains of arbitrarily complex geometries, subject to known boundary conditions. Such problems generally do not have analytical solutions. In

such cases, the finite element method is used to *predict* or *model* the behavior of a material based on known constitutive laws and directly measurable boundary conditions. In this application however, the constitutive laws of the material under test are unknown. Indeed, the objective of the experiments is to characterize and quantify them.

The idea of combining the finite element method with a full field measurement technique such as speckle interferometry, holography, photo-elasticity or Moiré methods is not new (Kobayashi, 1983). This is not surprising since they would seem to be tailor made for each other: the speckle interferometry gathers the continuum data and the finite element method is then used to perform the continuum analysis. In most applications to date however, both techniques are actually used separately. Generally, the outcome of an experiment measured using a full field measurement technique is compared to the theoretical predictions from a finite element model, in order either to validate the model or to give credence to the measurement technique.

In a few rare cases, as in the work by Weathers *et al.* (1985) and Matthys *et al.* (1986), speckle interferometry and the finite element method have been truly combined to simplify a complex finite element analysis problem. In both applications, the objective was to accurately model a small region within a larger body. Since the boundary conditions required to define the problem on the subregion of interest were not directly measurable, speckle interferometry was used to estimate them. These measurements were then used as the boundary conditions to a high density mesh defined over the smaller region of interest. In this type of application as well, known constitutive laws are used.

Recently, Hunter *et al.* (1992) have augmented the mathematical framework of the finite element method to facilitate numerically efficient *distributed parameter estimation*, in the context of electrical and mechanical modeling of cardiac tissue. In traditional parameter estimation, the experimenter seeks to model the input/output relation between a number of discrete inputs and outputs from a system under investigation. The process is often iterative, where a model of a given form is postulated along with a set of initial parameter values. The iterative refinement continues by minimizing some objective function, until the model predictions match the observed system outputs to within a satisfactory tolerance.

In *distributed* parameter estimation, the inputs and outputs are not discrete but form *continua* (the stress and strain fields). Furthermore, the input/output relation may change

spatially, when the material is inhomogeneous. Finally, as in traditional parameter estimation problems, the system may be non-linear and time-varying. Hence distributed parameter estimation is very challenging and powerful specialized tools are required.

Although the idea of distributed parameter estimation using finite elements is not entirely new (Kobayashi, 1983), the novel work by Hunter *et al.* (1992) significantly improves the numerical efficiency and stability of the process. Indeed, current methods involve solving a boundary value problem at each refinement iteration, over the entire mesh.

By fitting a finite element field description to the observed material deformations as proposed by Hunter *et al.* (1992), the predicted boundary forces are obtained directly from the constitutive law, without the need to solve a boundary value problem. The iterative refinement process thus seeks to minimize the discrepancy between the predicted and observed boundary forces by adjusting the model parameters, a significantly simpler task. Once a model has been generated from the experimental data using finite element-based parameter estimation techniques, the data from one experiment can be quantitatively compared to that from other experiments on other samples, and comparisons with known materials can be made. Mechanical behavior under conditions other than the ones which arose in the experiments can also be predicted.

6.1.1 The finite element mesh

The first step in analyzing data in the context of the finite element method is to represent the data in the appropriate analytic form, so that it can then be "cranked through" the finite element mathematical machine. The basic tool used to represent the material geometry and field is the *mesh* (see Figure 6.1), where the body is divided up into a series of connected *elements*. Each individual element is defined by its *nodes* at the element corners, where adjacent elements share common nodes.

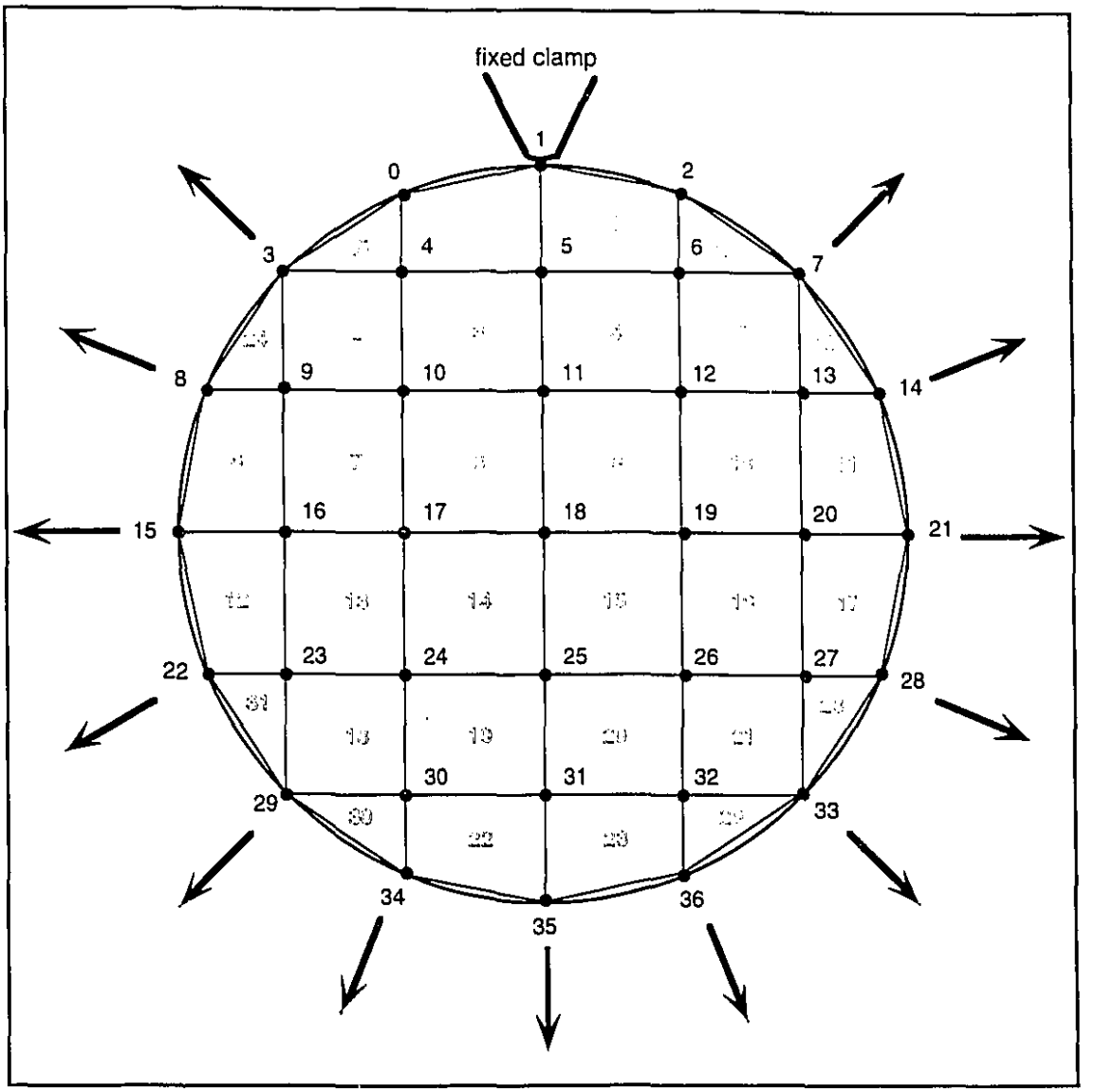

Figure 6.1: Finite element mesh layout. The element indices are shown in outlined characters whilst the node indices are shown in regular characters. The arrows indicate the directions of applied forces.

Each node in the mesh carries with it the geometric coordinates of the body at that point, as well as any field values which are defined over the mesh, such as temperature, electric or magnetic field, etc. The field and geometry values within the elements are interpolated from the values at the nodes. The interpolating functions can be of arbitrarily high order, depending on the complexity of the field or geometry, and the degree of accuracy required of the model. Generally, the degree of accuracy of the model can be

increased by either refining the mesh or by using higher order basis functions, with different tradeoffs in both cases (Zienkiewicz and Morgan, 1983).

Although the finite element method can be used to solve problems in multiple dimensions, only the two dimensional or planar case will be discussed here, since the problem under consideration is that of planar elasticity. The most common planar element shapes are the triangle and the rectangle. Both are used in the mesh in Figure 6.1, with linear interpolation basis functions defined below.

6.1.1.1 Linear triangle elements

This type of interpolation is based on mapping an arbitrary triangular area in the plane defined by the three points (x_1,y_1), (x_2,y_2) and (x_3,y_3) into a 1×1 square area in normalized (ξ_1,ξ_2) element coordinate space (see Figure 6.2).

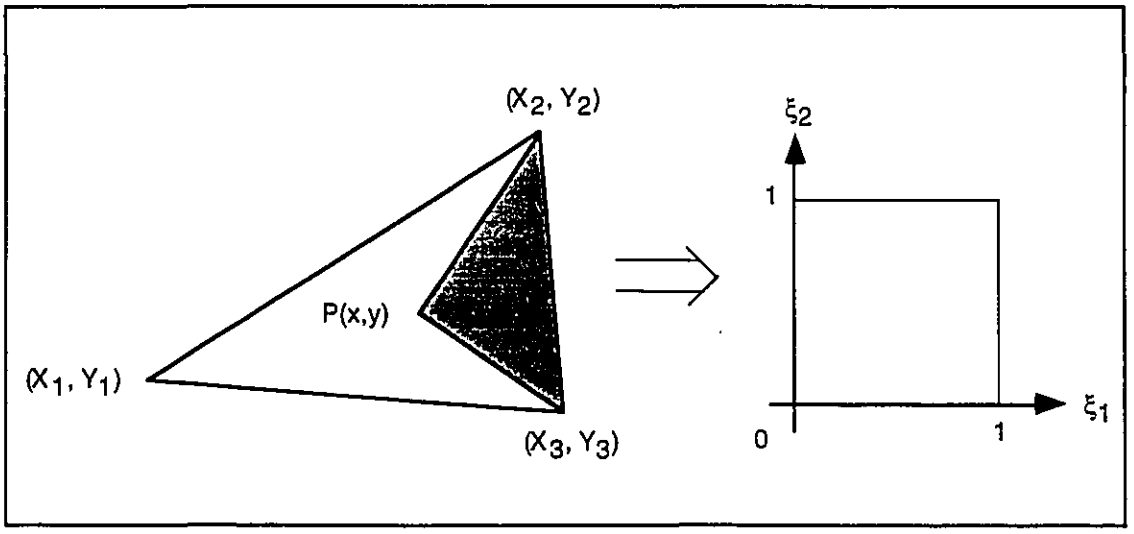

Figure 6.2: Linear triangle element interpolation.

The interpolated geometrical coordinates $(\hat{x},\hat{y})$ of a point (x,y) within the element are expressed in terms of the basis functions $\Psi_i(\xi_1,\xi_2)$ and the nodal coordinates (x_i,y_i), i=1...3, as follows:

$$\begin{aligned}\hat{x} &= x_1\Psi_1(\xi_1,\xi_2)+x_2\Psi_2(\xi_1,\xi_2)+x_3\Psi_3(\xi_1,\xi_2)\\ \hat{y} &= y_1\Psi_1(\xi_1,\xi_2)+y_2\Psi_2(\xi_1,\xi_2)+y_3\Psi_3(\xi_1,\xi_2),\end{aligned} \tag{6.1}$$

where the basis functions $\Psi_i(\xi_1,\xi_2)$ are defined as:

$$\begin{aligned}\Psi_1(\xi_1,\xi_2) &= \xi_1\\ \Psi_2(\xi_1,\xi_2) &= \xi_2\\ \Psi_3(\xi_1,\xi_2) &= 1-\xi_1-\xi_2.\end{aligned} \tag{6.2}$$

The element coordinates (ξ_1,ξ_2) of a point *(x,y)* inside the triangular element can be determined by calculating ratios of triangles (see Figure 6.2):

$$\begin{aligned}\xi_1 &= \frac{areaP23}{area123} = \frac{\begin{vmatrix}1 & x & y\\ 1 & x_2 & y_2\\ 1 & x_3 & y_3\end{vmatrix}}{2\Delta}\\ \xi_2 &= \frac{areaP13}{area123} = \frac{\begin{vmatrix}1 & x & y\\ 1 & x_1 & y_1\\ 1 & x_3 & y_3\end{vmatrix}}{2\Delta},\end{aligned} \tag{6.3}$$

where Δ is the area of the element:

$$\Delta = \frac{1}{2}\begin{vmatrix}1 & x_1 & y_1\\ 1 & x_2 & y_2\\ 1 & x_3 & y_3\end{vmatrix}. \tag{6.4}$$

6.1.1.2 Bilinear rectangle elements

This type of interpolation is based on mapping an arbitrary 4-sided polygon in the plane defined by the four points (x_1,y_1), (x_2,y_2), (x_3,y_3) and (x_4,y_4) into a 1×1 square area in normalized (ξ_1,ξ_2) element coordinate space (see Figure 6.3).

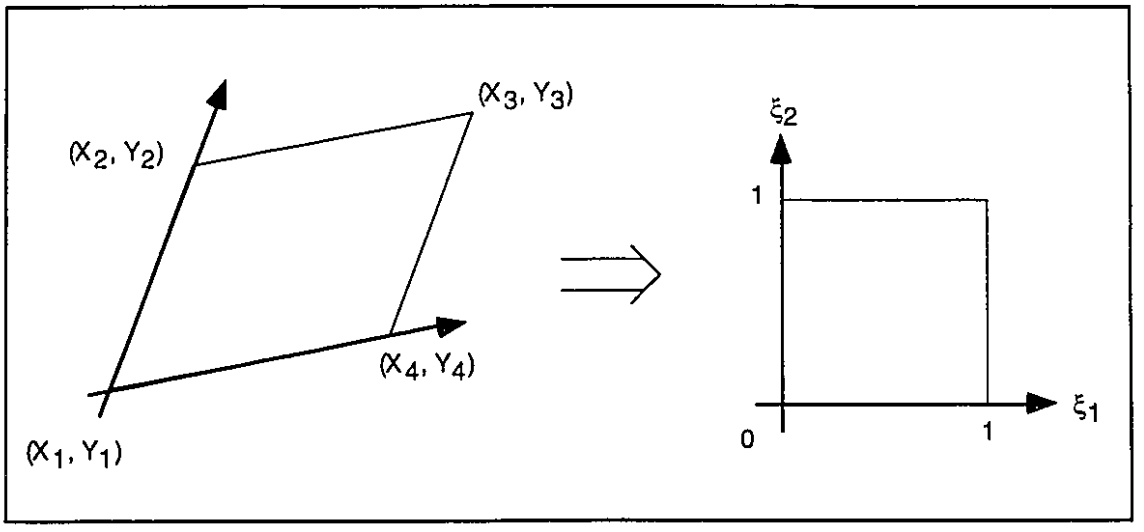

Figure 6.3: Bilinear rectangle element interpolation.

The interpolated geometrical coordinates $(\hat{x},\hat{y})$ of a point (x,y) within the element can then be expressed in terms of the basis functions $\Psi_i(\xi_1,\xi_2)$ and the nodal coordinates (x_i,y_i), i=1...4, as follows:

$$\begin{aligned}\hat{x} &= x_1\Psi_1(\xi_1,\xi_2)+x_2\Psi_2(\xi_1,\xi_2)+x_3\Psi_3(\xi_1,\xi_2)+x_4\Psi_4(\xi_1,\xi_2)\\ \hat{y} &= y_1\Psi_1(\xi_1,\xi_2)+y_2\Psi_2(\xi_1,\xi_2)+y_3\Psi_3(\xi_1,\xi_2)+y_4\Psi_4(\xi_1,\xi_2),\end{aligned} \tag{6.5}$$

where the basis functions $\Psi_i(\xi_1,\xi_2)$ are defined as:

$$\begin{aligned}\Psi_1(\xi_1,\xi_2) &= (1-\xi_1)(1-\xi_2)\\ \Psi_2(\xi_1,\xi_2) &= (1-\xi_1)\xi_2\\ \Psi_3(\xi_1,\xi_2) &= \xi_1\xi_2\\ \Psi_4(\xi_1,\xi_2) &= \xi_1(1-\xi_2)\end{aligned} \tag{6.6}$$

The element coordinates (ξ_1, ξ_2) of a point (x,y) inside the element can be calculated by inverting (6.5), where a quadratic equation in either parameter is generated:

$$a(x,y)\xi_1^2 + b(x,y)\xi_1 + c(x,y) = 0, \tag{6.7}$$

where:

$$\begin{aligned} a(x,y) &= (x_1 - x_2 + x_3 - x_4)(-y_1 + y_4) - (-x_1 + x_4)(y_1 - y_2 + y_3 - y_4) \\ b(x,y) &= (x - x_1)(y_1 - y_2 + y_3 - y_4) - (x_1 - x_2 + x_3 - x_4)(y - y_1) \\ &\quad + (-x_1 + x_2)(-y_1 + y_4) - (-x_1 + x_4)(-y_1 + y_2) \\ c(x,y) &= (x - x_1)(-y_1 + y_2) - (-x_1 + x_2)(y - y_1) \end{aligned}$$

Only one of the two roots of (6.7) will lie in the interval [0,1], giving the correct values for ξ_1. The corresponding value for ξ_2 can be found by back substitution into (6.5).

6.1.2 Data fitting

The basic idea behind representing the experimentally measured membrane displacements with finite elements is to track the positions of a finite set of predefined material points on the membrane (the nodes), throughout the deformations. The displacements of any other point on the membrane can then be interpolated from this finite set of tracked points. The order of the interpolation and the number of tracked material points are selected such that the displacements of all other membrane points can be interpolated to a satisfactory degree of accuracy.

The finite element mesh is first defined from an initial data set, using some user-specified material points as the nodes. The computer then uses the incremental displacement data sets at each stretch step to update the mesh definition and thus follow the selected material point locations through the entire membrane deformation. From the individual displacements at the nodes, all others displacements can be then interpolated and useful information such as strain may be determined analytically.

6.1.2.1 Initial mesh definition

A natural choice of fixed material points to track are the hook tether locations where forces are applied to the membrane. Not only are the locations of these points required for defining boundary conditions at the time of analysis, but they are also easy to track visually. Hence, the model predictions may be verified throughout the experiment by comparing the predicted boundary node positions to the actual hook locations shown in the video recording of the experiment. Another natural choice for a tracked material point is the tip of the clamp that provides a fixed reference point for the speckle image processing.

The mesh used in the experiments is shown in Figure 6.1, where the tether points and the clamp tip define most of the mesh boundary nodes. The internal nodes are defined arbitrarily by laying down a grid connecting the boundary nodes. The initial mesh definition is accomplished in two steps. First the tether point locations are specified by hand with a mouse, based on the image of the membrane in its reference state. Then the computer calculates the internal node locations automatically. Note that there are two free boundary nodes which are required for symmetry purposes. They are defined by hand arbitrarily. As seen in Figure 6.1, there are 24 rectangular elements and 8 triangular elements in the mesh for a total of 37 nodes.

6.1.2.2 Deformed mesh fitting

The e_1 and e_2 displacement data sets obtained in the experiments are used to update incrementally the mesh from the initial reference state definition, up to the state of maximum extension. The mesh updating process from one step to the next is based on the idea of fitting to the mesh a *nodal displacement field* which best represents the data. For a particular stretch step, the point-wise displacement measurements obtained from the phase-unwrapping process are considered as an ensemble of field samples. The objective is then to determine the set of field values at the nodes which best fits the ensemble of field samples. Note that the e_1 and e_2 displacement fields are fitted separately. The discussion below explains the procedure for the e_1 field, but the process is identical for both axes. In the end, the separately fitted e_1 and e_2 displacement fields are used jointly to update the mesh node coordinates.

The method for calculating the optimal displacement field values Δu_i at the nodes is based on minimizing the sum of squared residuals between the experimentally measured field samples δu_k and the corresponding interpolated field estimates $\delta \hat{u}_k$. Generally in finite element problems such as in heat conduction or electric field distribution, the object geometry and the field may be interpolated with different basis functions. Often, the geometry is interpolated with a low order basis function, whereas the field may be interpolated with a higher order basis function. In finite elasticity problems however, the field (displacement) is actually a change in the object geometry, so that both are interpolated with the same basis functions. Hence in this case, the displacement field estimates $\delta \hat{u}_k$ are interpolated from the nodal field values Δu_i, in a similar manner to (6.1) and (6.5) :

$$\delta \hat{u}_k = \Delta u_i \Psi_i\left(\xi_1\Big|_{\delta u_k}, \xi_2\Big|_{\delta u_k}\right), \tag{6.8}$$

and where the basis functions $\Psi_i(\xi_1, \xi_2)$ are either given by (6.2) or (6.6) depending on the element type. The vertical bars next to the ξ_i indicate that they correspond to the element coordinates of sample δu_k.

The sum of squared residuals, r_u, between the measured field samples and interpolated estimates is expressed as:

$$\begin{aligned} r_u &= \sum_{k}^{all\ samples} \left[\delta u_k - \delta \hat{u}_k\right]^2 \\ &= \sum_{k}^{all\ samples} \left[\delta u_k - \Delta u_i \Psi_i\left(\xi_1\Big|_{\delta u_k}, \xi_2\Big|_{\delta u_k}\right)\right]^2 . \end{aligned} \tag{6.9}$$

The only unknown quantities in (6.9) are the desired field values at the nodes Δu_i. Hence by minimizing (6.9) with respect to the unknowns, the optimal nodal displacement field values are obtained, in the least squares sense. By differentiating r_u with respect to the unknowns and setting the resulting expressions to zero, a set of simultaneous equations is obtained which can be solved to obtain the optimal nodal field values.

In an identical fashion, the sum of squared residuals r_v for displacements in the e_2 axis in the plane is given by:

$$r_v = \sum_{k}^{all\ samples} \left[\delta v_k - \Delta v_i \Psi_i \left(\xi_1 \middle| \delta v_k , \xi_2 \middle| \delta v_k \right) \right]^2 . \tag{6.10}$$

Hence by differentiating (6.9) and (6.10), two independent systems of simultaneous equations are obtained, which are solved for the nodal displacement field values in the two orthogonal axes in the plane. The current mesh nodal coordinates are then updated by incrementing them by the fitted displacement field values. Since there are 37 nodes in the mesh, two 37×37 square matrix systems must be solved at each stretch step to update the mesh nodal coordinates. Note that since each sample estimate is interpolated as a function only of the nodal field values at the corners of the element in which the sample resides, the matrix systems are sparse. Hence, although not used here, the equations can be solved with more efficient sparse or band matrix numerical techniques.

6.1.2.3 Element coordinate calculations

As explained in the previous section, the mesh nodal coordinates are updated following each stretch step in the finite element analysis. As a consequence of this, the element coordinates of *all samples* will also change at each step. This occurs because the samples are taken at a fixed grid in space (the CCD camera sensing element grid) which is stationary with respect to the deforming membrane and finite element mesh. In effect, the membrane displacements are discretely sampled at a different set of material points at each stretch step. Hence the element coordinates (ξ_1, ξ_2) for all samples within the membrane boundary must be recomputed for the data at each stretch step, to set up properly the sum of squared residuals matrix systems.

The first step in this process is to identify to which element each sample belongs. Indeed, as the mesh deforms, elements will sweep across the fixed sampling grid and individual samples will end up in different elements at different stages. Because the elements are arbitrary 4-sided polygons and triangles, the identification of the correct element for each sample is not a straightforward procedure. The system used here is the following: an image of the mesh is drawn into memory where each element is rendered as a

filled polygon with a distinct color. The color index at each (x,y) location in the image thus identifies the correct element for the individual samples. The second step in the process is then to calculate the element coordinates ξ_1,ξ_2 within the correct element for each sample, using (6.3) or (6.7) depending on the element type.

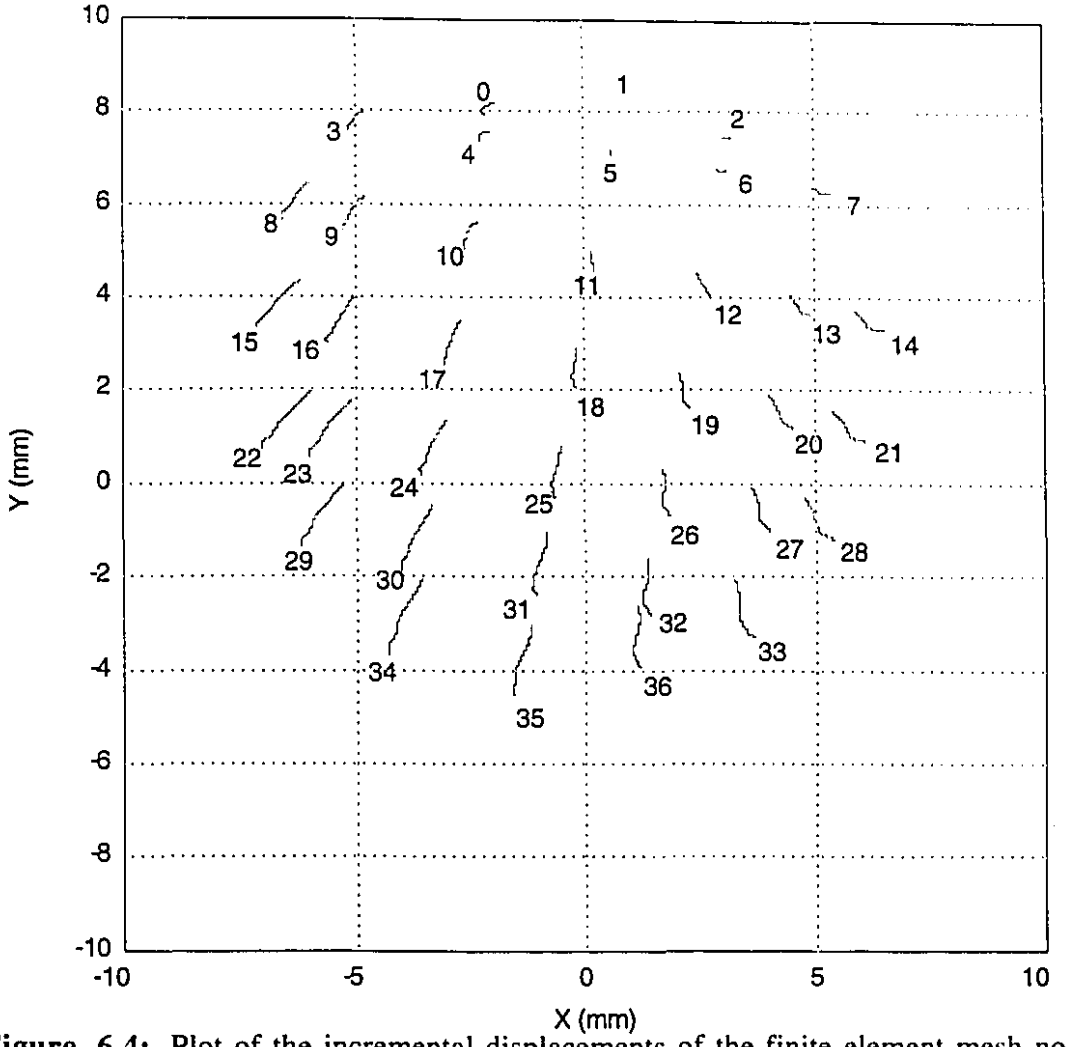

Figure 6.4: Plot of the incremental displacements of the finite element mesh nodes throughout the 450 stretch steps of experiment I, on a canine pericardium membrane.

6.1.2.4 Data fitting experimental results

The results of the data fitting and mesh update procedure described above are shown in Figures 6.4 and 6.5 for two typical canine pericardium experiments. The figures show composite plots of all nodal displacements throughout the experiments, from the reference state to the state of maximum extension. Recall that every set of incremental node

coordinate updates (450 for experiment I and 350 for experiment II) was obtained by solving two 37×37 matrix systems. At each step, the number of usable samples in each data set was fairly large: up to 10^5 samples/image in the case of data sets close the maximum extension.

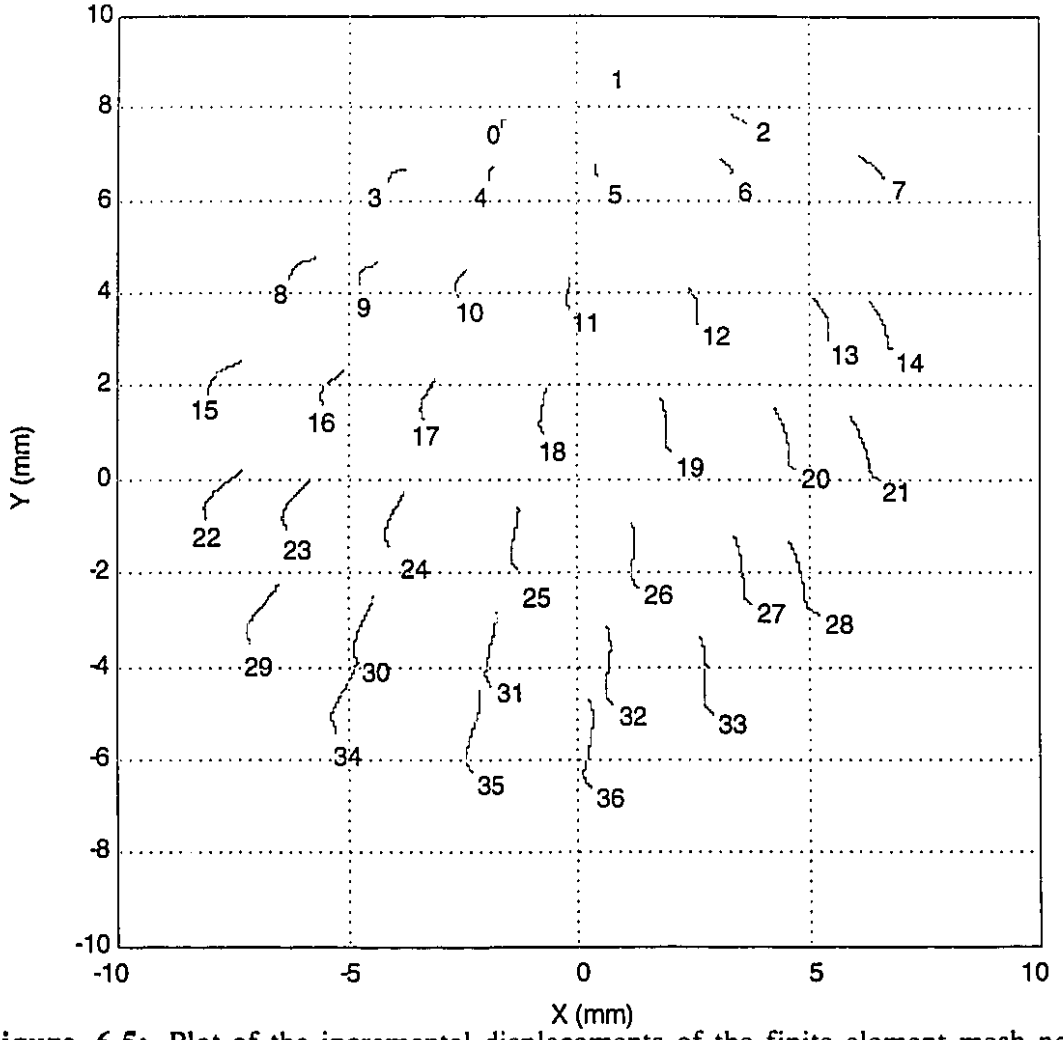

Figure 6.5: Plot of the incremental displacements of the finite element mesh node, throughout the 350 stretch steps of experiment II, on a canine pericardium membrane.

As explained later in this chapter, the distributed parameter estimation portion of the data analysis was performed at the University of Auckland by Dr. Peter Hunter, using the CMISS finite element analysis program. A typical result of the data representation with finite elements computed with CMISS in shown in Figure 6.6, where the initial and final meshes are overlaid, for the data of experiment II.

The reference and maximally stretched finite element meshes for both experiments are shown in Plates VIII and IX, where they are overlaid on top of the corresponding normal light or "white light" images. As explained above, the initial meshes shown in Plates VIII (a) and IX (a) were partially defined manually, by marking the tether points with a mouse. Note the position of the clamp (the roughly triangular shaped object at the top/center of the images) and the 13 hooks (the shiny objects in the periphery).

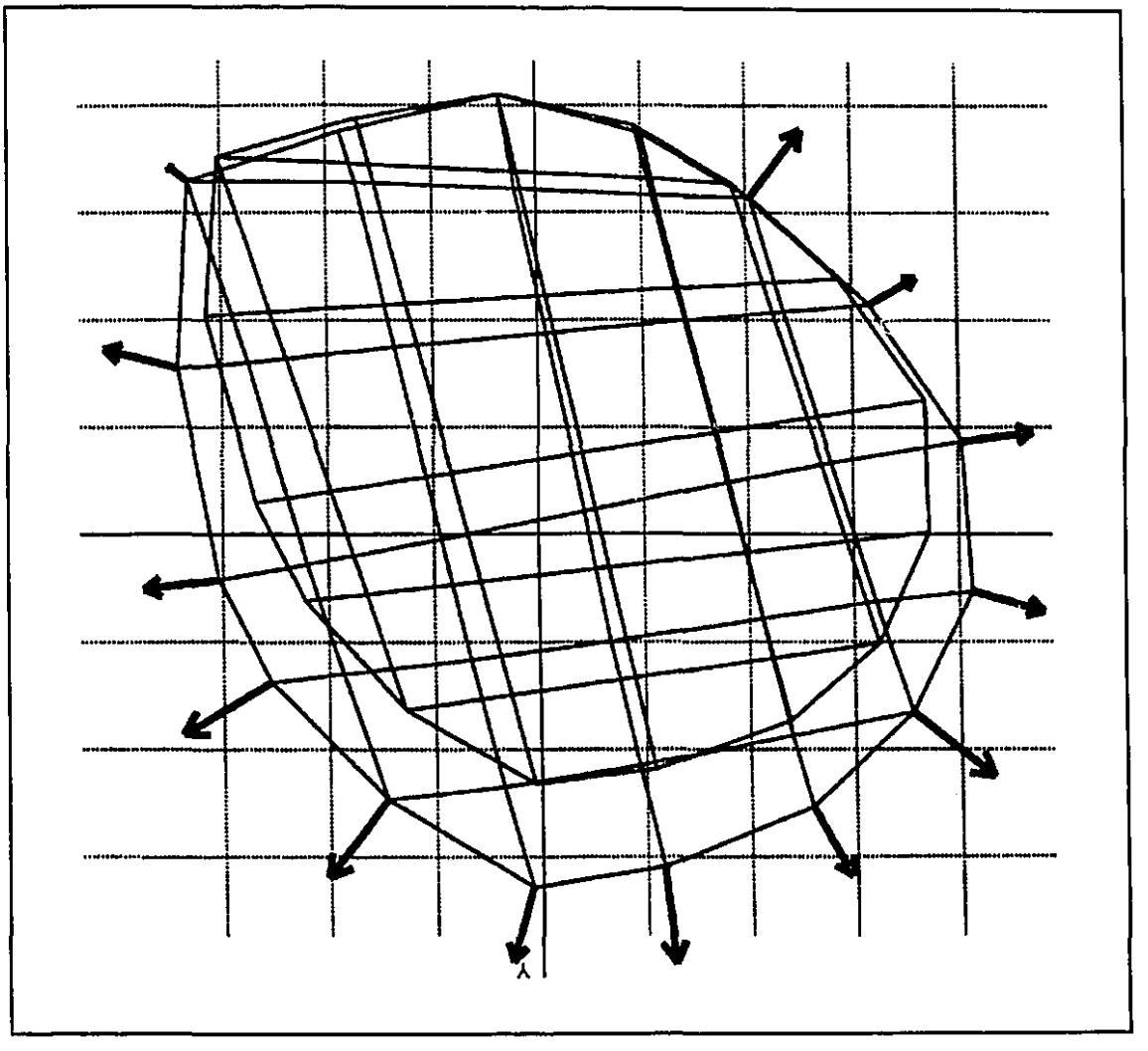

Figure 6.6: Overlaid plots of the initial and maximally stretched finite element meshes for experiment II. Courtesy of Dr. Peter Hunter, University of Auckland, New Zealand.

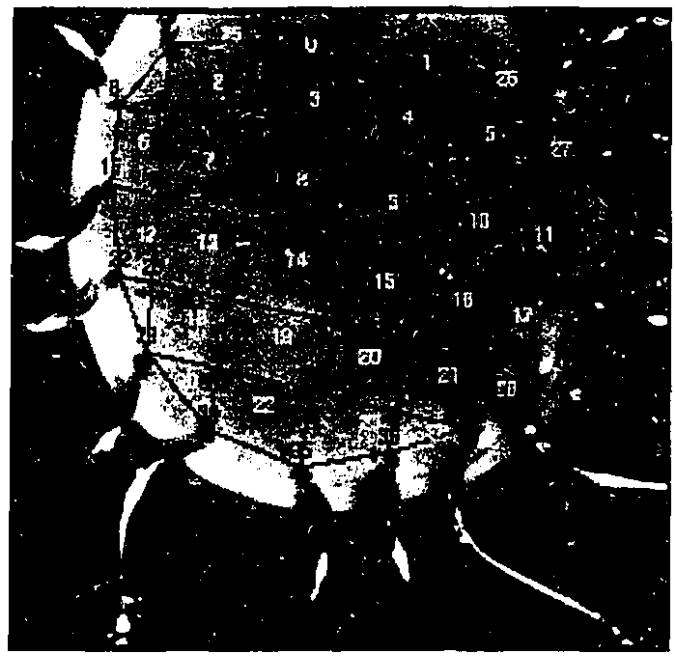

(a) Unstretched initial state. The roughly circular region inside the hooks has a diameter of approximately 10 mm.

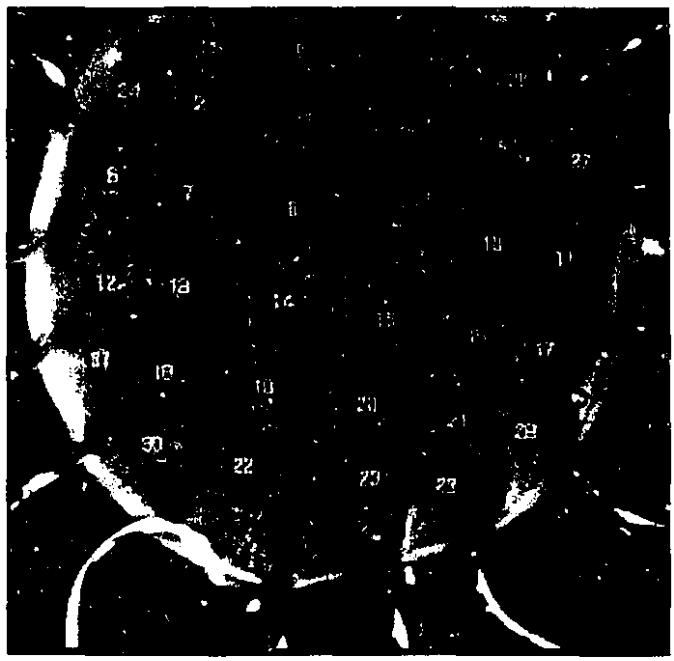

(b) Maximum extension, after 450 discrete stretch steps.

PLATE VIII : White light images of the pericardium membrane from experiment I at minimum and maximum extension. The fitted finite element meshes are shown as overlays.

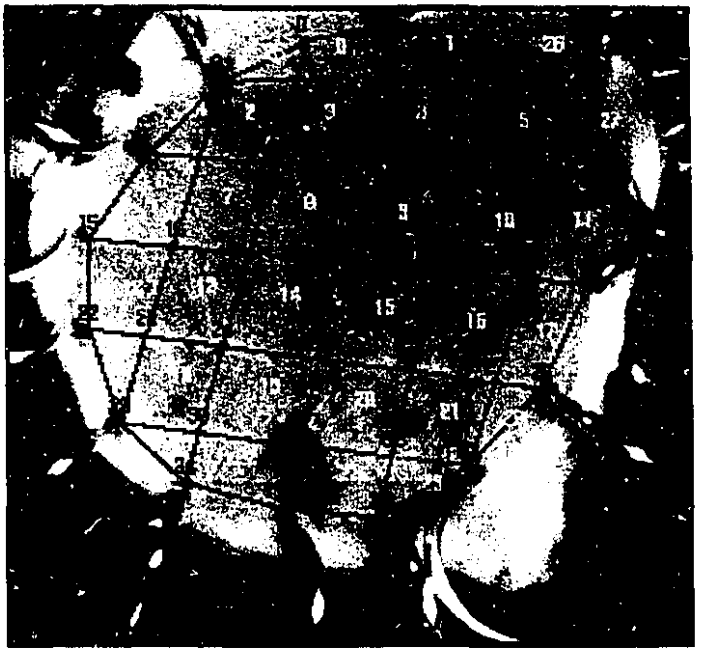

(a) Unstretched initial state. The roughly circular region inside the hooks has a diameter of approximately 10 mm.

(b) Maximum extension, after 350 discrete stretch steps.

PLATE IX: White light images of the pericardium membrane from experiment II at minimum and maximum extensions. The fitted finite element meshes are shown as overlays.

It can be seen from the images in Plates VIII and IX that substantial ripping occurred around certain tether points. This significantly hindered the calculation of accurate displacement estimates in the neighborhood of these boundary nodes. Indeed, not only did the ripping holes reduce the number of available samples around the tether points, but the data samples that were available were of questionable reliability because of the damaged tissue. In order to minimize the effect of this problem, the boundary mesh nodes at the tether points were actually defined as the membrane points just inside the ripping holes.

Although this solution was sufficient at small and medium deformations, it was only partially successful at the larger strains, as seen in Plates VIII (b) and IX (b), where some boundary mesh nodes are slightly off from their expected positions. It must be emphasized however that the membrane in both experiments was stretched to beyond 1.3 times its original size, by 13 point loads. This is a worst case scenario in that the strains are close to the point of unrecoverable damage to the tissue and the large forces required are applied at single points without any kind of local stress relief. It is conceivable that had the applied load been distributed more uniformly, this problem might not have occurred.

6.1.2.5 Markers

In any case, a more appropriate measure of the finite element representation of the data was required. For this purpose, a number of membrane surface features clearly visible in the white light images and well away from the tether points were used as markers. The first step in the verification procedure was to manually determine the marker displacements with a mouse from the eight white light images covering the entire stretch experiment, at intervals of 50 stretch steps.

In the second step of the verification procedure, the marker initial locations were again identified from the reference state white light image with a mouse. These coordinates were used as starting locations for calculating predicted paths using the finite element representation. Hence, the element coordinates (ξ_1, ξ_2) of each marker starting location were calculated. These fixed element coordinates were then used with (6.5) to interpolate the markers paths at each stretch step, as a function of the changing nodal coordinates x_i, y_i, (i = 1...4). Figure 6.7 shows a typical result, where the stars (*) represent the marker path determined manually and the solid line is the finite element prediction.

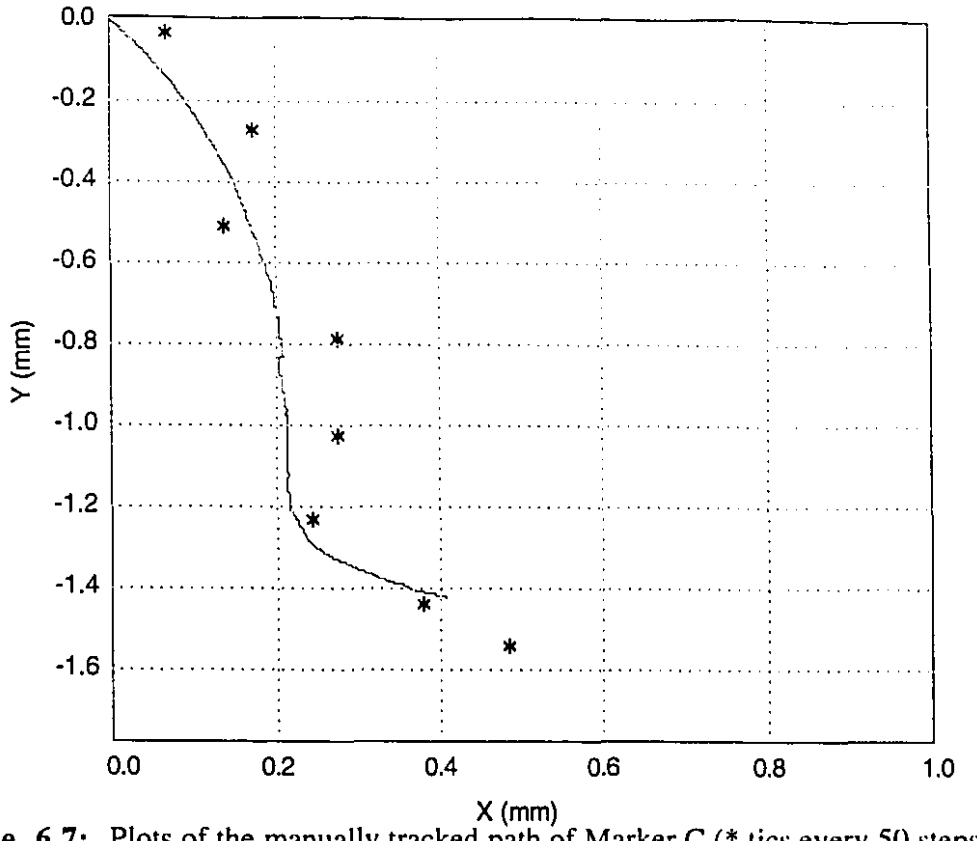

Figure 6.7: Plots of the manually tracked path of Marker C (* tics every 50 steps) and the finite element path estimate for the 350 steps of experiment II.

Note that there was a significant amount of error involved in manually identifying the position of a marker on the membrane with a mouse. This can be seen in Figure 6.7 by the fact that the manually determined trajectory and the predicted path do not start off from the same point. Indeed, the reason for not using the same starting location in both steps of the verification procedure was to test the accuracy of repeated manual identification of the same material point. The difference between the starting points is thus a measure of the error involved in manually identifying a marker position: about 2 pixels on average. Note also that as the membrane stretched, the surface features used as markers did also, and hence became more diffuse and difficult to track visually. The manual error at maximum stretch is thus slightly greater than that at the reference state.

The average error between the predicted and manually tracked paths of the markers was determined by first calculating the absolute value of the endpoint differences between the actual and predicted trajectories for each marker. These values were then corrected for manual errors by subtracting from them their respective start point offsets. The resulting

values were then expressed as percentages of the total distance moved by each marker. This came to about 2.5% on average, which is well within the theoretically predicted accuracy of the method (5.5%), calculated in chapter 4.

6.1.2.6 Goodness of fit of the linear model

As stated at the beginning of this chapter, the basis functions used to interpolate the field values inside the elements can be of any order. The trade-off is one of computational speed and ease of implementation versus accuracy of the fit. Hence, for an optimal system, the objective is to select a basis function of the lowest possible order that still satisfies the accuracy requirements for the application.

The technique described in this thesis incorporates several different subsystems (optics, mechanics, phase-unwrapping, finite element analysis, etc.), each fairly unique and complex in its own right. It was felt that in order for this first integration of all these complex parts to have a reasonable chance of success, the different sub-systems should not be initially implemented in their most complex and powerful form. For example in the experiments, the target membrane was always stretched in a roughly uniform manner, thus generating fairly simple and well behaved displacement fields. In light of this, low-order bilinear basis functions were selected, for ease of implementation reasons.

Indeed, when higher-order basis functions such as bicubic Hermite polynomials (Wait and Mitchell, 1985) are used, there is no analytical solution for determining the sample element coordinates. Non-linear iterative methods such as Newton-Raphson must be used, at each sample. Although this presents no conceptual problem, it does increase the computer processing time significantly. For example, initial tests were run using both bilinear and bicubic Hermite basis functions to interpolate the displacement fields. Although there was only a marginal improvement in the accuracy of the fit with the Hermite basis functions, the processing time on the IBM RISC System/6000 workstations went from an average 15 s/image in the bilinear case to 120 s/image in the bicubic case. In future implementations of the technique, when strain fields of arbitrary complexity will be imposed on the target membrane, it is expected that higher-order basis functions will be required.

In order to assess the general goodness of fit of the bilinear rectangle and linear triangle models, the *percentage variance accounted for* (*%VAF*) by the models was calculated separately for each element at each stretch step:

$$\%VAF = 100\left(1 - \frac{\sum_{all\ samples}(\partial u - \partial \hat{u})^2}{\sum_{all\ samples}\partial u^2}\right). \tag{6.11}$$

The *%VAF* values were also used to flag any situation where the fit was locally misbehaving, such as if the membrane suddenly ripped at a particular tether point or if one of the actuators went momentarily unstable. A typical result is shown in Figure 6.8, which presents a plot of the *%VAF* for by the bilinear model of element #22, across the 450 stretch steps of experiment I.

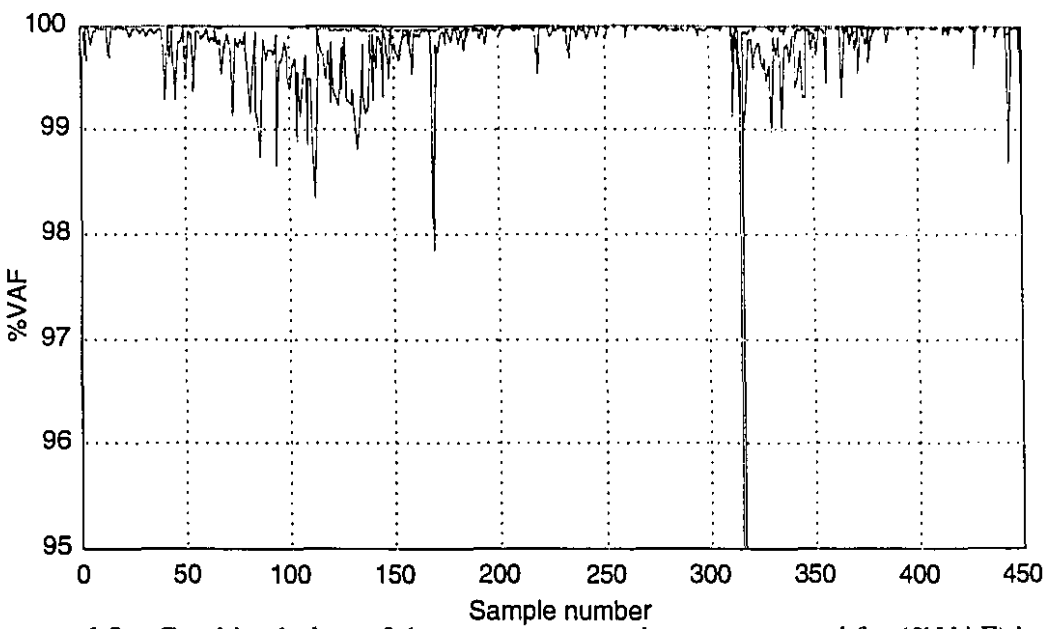

Figure 6.8: Combined plots of the *percentage variance accounted for* (%VAF) by the bilinear basis functions in the finite element model for both the x and y displacement fields at mesh element 21, across all 450 steps of experiment I.

As can be seen from the plot, most of the values are above 99%, hence the bilinear model representation is excellent. Note also that the *%VAF* dips to a low value at sample #320. This situation occurred because the actuator pulling at node #33 temporarily went

unstable, blurring out the speckle pattern in the lower right portion of the membrane. This behavior happened on rare occasions because the AE1000 amplifier analog servo-loops were designed to control galvanometers driving a fixed inertial load. In this application however, the apparent inertia seen by the actuator increases as the forces applied to the membrane increase, thus causing certain servo loops operating near tolerance to go unstable. The *%VAF* calculations however were an effective and successful way of checking for such occurrences. Since this was a rare phenomenon (less than one occurrence per experiment on average), the problem was solved simply omitting the low *%VAF* data sets from the mesh node update process.

A combined "worst case" *%VAF* plot is shown in Figure 6.9 where plots of the *%VAF* values for all elements across all stretch steps for experiment I are overlaid. As seen from the figure, the great majority of values are above 95%, with the exception of sample #320, thus confirming the appropriateness of the linear model for uniform stretches.

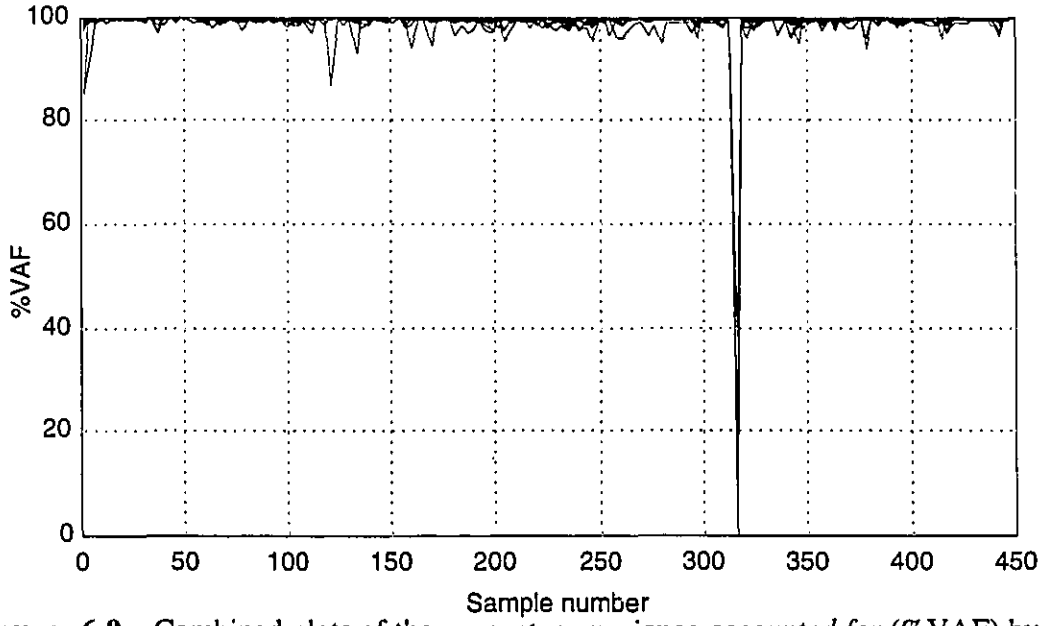

Figure 6.9: Combined plots of the *percentage variance accounted for* (%VAF) by the linear basis functions in the finite element model for both the x and y displacement fields at each of the 32 mesh elements, across all 450 steps of experiment I.

6.2 Strain computations

The real quantity of interest that is sought from the experimental data is the *strain*, which is a measure of the deformation of the body. Although the notion of stress is a conceptually straightforward one (force per unit area), that of strain is not. Indeed there are many different formulations of strain in use and many more which are also theoretically acceptable. The basic concept behind most common measures of strain is the change in the squared length of a line element dL^2 in a body between two deformation states. Although it might seem intuitively more appropriate to consider the change in length of a line element as opposed the squared length, the latter is easier work with mathematically, as Pythagoras's theorem can be brought to bear.

The strain formulation used in the analysis here is based on the *deformation gradient tensor*, F_{iM}, (Atkins and Fox, 1980; Spencer, 1980). The derivations below are given initially for a general n dimensional coordinate space, where the X_M (M=1...n) are the material point coordinates in the undeformed state and the x_i (i=1...n) are the corresponding material point coordinates in the deformed state. In this notation, a line element, dL, in the undeformed state is represented by its components dX_M, and the corresponding deformed line element, dl, by its components dx_i. At the end of this section, the expression for strain in two dimensional Cartesian coordinates is given.

The deformation gradient tensor, F_{iM}, expresses the change in the deformed material coordinates with respect to the undeformed coordinates, and is defined as:

$$F_{iM} = \frac{\partial x_i}{\partial X_M}. \tag{6.12}$$

The deformed material line element components dx_i can then be expressed as a function of the undeformed material line element components dX_M using the deformation gradient tensor components:

$$dx_i = F_{iM} dX_M. \tag{6.13}$$

Note that for a rigid body motion without deformation, it can be shown (Spencer, 1980) that the deformation gradient tensor has the following property:

$$\boldsymbol{F}^{\boldsymbol{T}}\boldsymbol{F} = \boldsymbol{I} \quad \text{or} \quad F_{iN}F_{iM} = \delta_{NM}, \tag{6.14}$$

where δ_{NM} is the Kronecker delta function and I is the identity matrix. The *Lagrangian strain tensor*, $\boldsymbol{e}$, is then defined as:

$$\mathbf{e} = \frac{1}{2}\left(\mathbf{F}^{\mathbf{T}}\mathbf{F} - \mathbf{I}\right)$$

or

$$e_{NM} = \frac{1}{2}\left(F_{iN}F_{iM} - \delta_{NM}\right) = \frac{1}{2}\left(\delta_{ij}\frac{\partial x_i}{\partial X_N}\frac{\partial x_j}{\partial X_M} - \delta_{NM}\right). \tag{6.15}$$

Note that from (6.14), in the case of a rigid body motion without deformation, e_{NM} will be equal to zero. From (6.13) and (6.15), the change in the squared length of a line element dL^2 in the undeformed state to dl^2 in the deformed state is equal to:

$$dl^2 - dL^2 = dx_i dx_i - dX_M dX_M = e_{MN}dX_M dX_N. \tag{6.16}$$

In order to determine the strain, the deformation gradient tensor components must first be calculated. In the context of finite elements, the link between the undeformed X_i and the deformed coordinates x_i are the element coordinates ξ_i, which *remain constant* for any material point throughout the deformation. Using the chain rule for differentiation, the deformation gradient tensor components can be expressed as:

$$F_{iM} = \frac{\partial x_i}{\partial X_M} = \frac{\partial x_i}{\partial \xi_k}\frac{\partial \xi_k}{\partial X_M}, \tag{6.17}$$

where the value of the $\frac{\partial x_i}{\partial \xi_k}$ terms in (6.17) are obtained by differentiating the $x_i(\xi_k)$ interpolation equations, such as (6.1) and (6.5).

The Jacobian of the coordinate transformation is used to compute the value of the $\frac{\partial \xi_k}{\partial X_M}$ terms in (6.17) as:

$$\frac{\partial \xi_i}{\partial X_M} = \left[\frac{\partial X_M}{\partial \xi_i}\right]^{-1}, \tag{6.18}$$

where the Jacobian elements are obtained by differentiating the $X_M(\xi_k)$ interpolation equations, also given by (6.1) and (6.5).

For a finite elasticity problem in the plane, $i = j = 2$. Using Cartesian coordinates, where $X_1=X$, $X_2=Y$ and $x_1=x$, $x_2=y$, the strain tensor, $\boldsymbol{e}$, at a point can be expressed as:

$$\mathbf{e} = \frac{1}{2}\left\{\begin{bmatrix} \frac{\partial x}{\partial X} & \frac{\partial y}{\partial X} \\ \frac{\partial x}{\partial Y} & \frac{\partial y}{\partial Y} \end{bmatrix}\begin{bmatrix} \frac{\partial x}{\partial X} & \frac{\partial x}{\partial Y} \\ \frac{\partial y}{\partial X} & \frac{\partial y}{\partial Y} \end{bmatrix} - \begin{bmatrix} 1 & 0 \\ 0 & 1 \end{bmatrix}\right\}, \tag{6.19}$$

$$= \frac{1}{2}\begin{bmatrix} \left(\frac{\partial x}{\partial X}\right)^2 + \left(\frac{\partial y}{\partial X}\right)^2 - 1 & \left(\frac{\partial x}{\partial X}\right)\left(\frac{\partial x}{\partial Y}\right) + \left(\frac{\partial y}{\partial X}\right)\left(\frac{\partial y}{\partial Y}\right) \\ \left(\frac{\partial x}{\partial X}\right)\left(\frac{\partial x}{\partial Y}\right) + \left(\frac{\partial y}{\partial X}\right)\left(\frac{\partial y}{\partial Y}\right) & \left(\frac{\partial x}{\partial Y}\right)^2 + \left(\frac{\partial y}{\partial Y}\right)^2 - 1 \end{bmatrix}, \tag{6.20}$$

$$= \begin{bmatrix} e_{xx} & e_{xy} \\ e_{yx} & e_{yy} \end{bmatrix}. \tag{6.21}$$

Note that the strain tensor is symmetric, so that $e_{xy} = e_{yx}$. The diagonal elements, e_{xx} and e_{yy}, are known as the *normal* strains, whereas the off-diagonal elements, e_{xy} and e_{yx}, are know as the *shear* strains. The deformation tensor components in (6.20) above are calculated using (6.17), where each partial derivative is either directly calculated from the derivatives of the interpolation equations, or from the coordinate transformation matrix.

Note that although (6.20) is computed at every point in the image where the strain tensor is required, the tensor deformation components in the formula are determined analytically from expressions that are derived only once using the procedure described above and then "hardcoded" into the analysis program. To calculate the strain at a given sample point, the only required input values are the deformed (x_i, y_i) and undeformed (X_M, Y_M) nodal coordinates for the element containing that particular sample, as well as the sample element coordinates, (ξ_1, ξ_2). They are introduced into the strain computation subroutine which yields the strain tensor components.

Finally, as second-order tensors are awkward quantities to render in two dimensional images, the *principal strains* are usually displayed instead. Since the strain tensor is symmetric, it is known from matrix theory that there exists a coordinate system rotation through an angle, θ, that will diagonalize the tensor, where the shear components will be equal to zero. The new coordinate axes resulting from this rotation are referred to as the *principal axes* and the normal strain components of the diagonalized tensor are referred to as the *principal strains*. The required angle, θ, is given by (Fung, 1977):

$$\theta = \frac{1}{2}\tan^{-1}\left(\frac{2e_{xy}}{e_{xx} - e_{yy}}\right), \tag{6.22}$$

and the principal strain values, e_{max} and e_{min}, are given by:

$$e_{\min}^{\max} = \frac{e_{xx} + e_{yy}}{2} \pm \sqrt{\left(\frac{e_{xx} - e_{yy}}{2}\right)^2 + e_{xy}^2}. \tag{6.23}$$

Lagrangian strain computation results for the pericardium membranes of experiments I and II at the state of maximum extension are shown in plates X and XI, along with the corresponding finite element meshes. The principal axes are shown as small crosses at selected locations inside each element, where the length of the lines is proportional to the magnitude of the principal strains. In plates X (b) and XI (b), the background gray level in the images is proportional to the maximum principal strain, e_{max}, at each point. The largest strains in the membranes are approximately 0.24 for experiment I and 0.26 for experiment II.

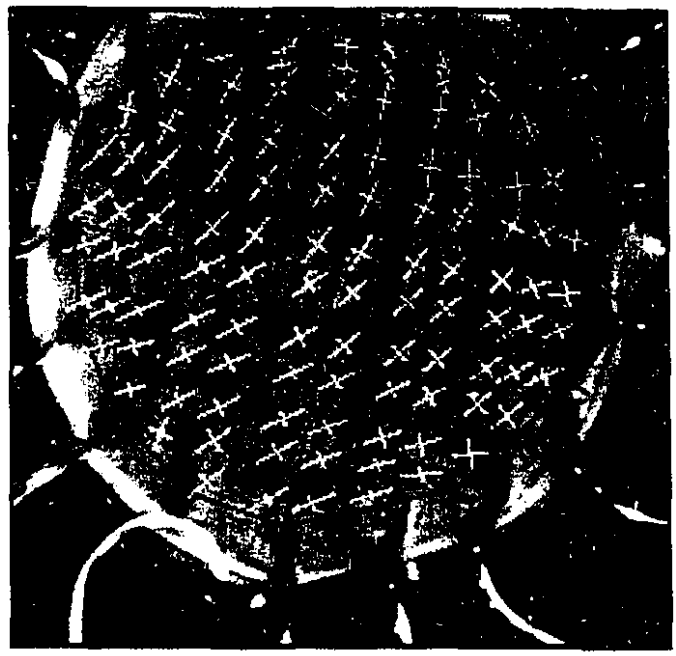

(a) White light image of the pericardium membrane in the fully stretched state, with the principal strains shown at the Gauss points.

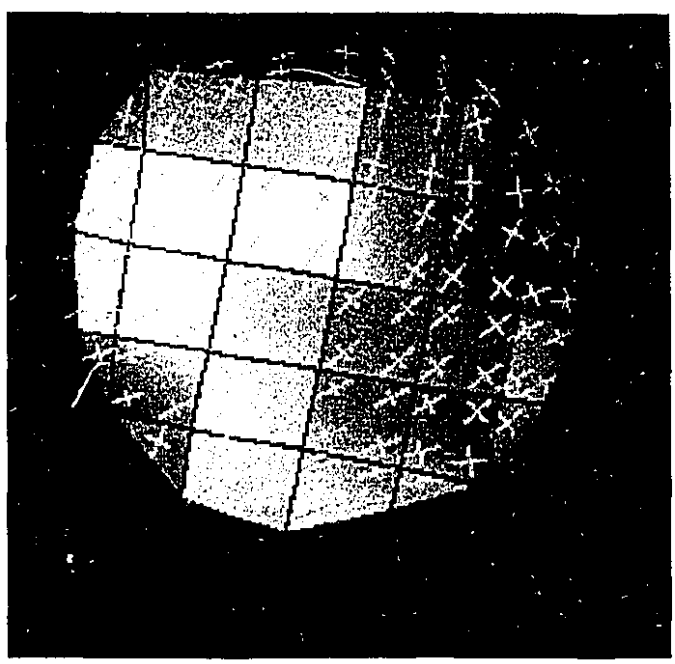

(b) Image of the magnitude of the largest principal strain at each point in the plane. Black pixels correspond to the smallest principal strain values (0.1), and white pixels correspond to the greatest principal strain values (0.27).

PLATE X: Plane strain results for the canine pericardium membrane of experiment I. The fitted finite element meshes and the principal strains at the Gauss points are shown as overlays.

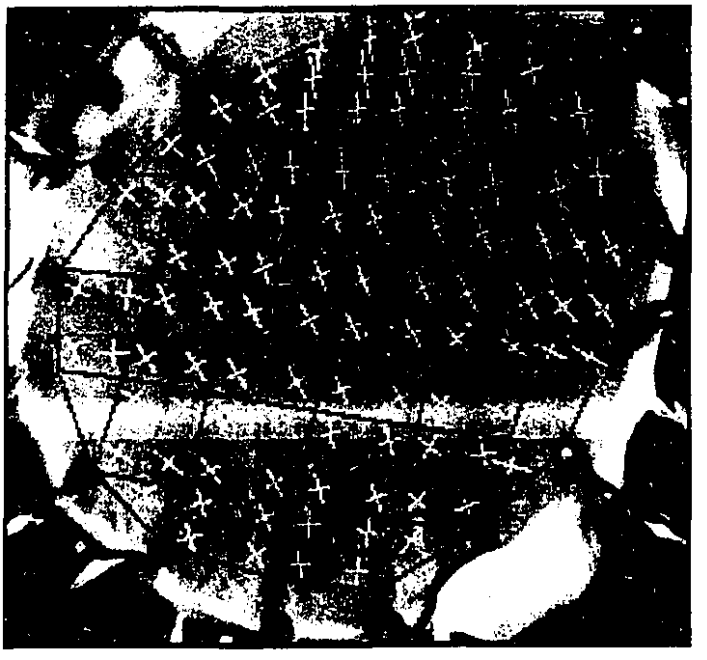

(a) White light image of the pericardium membrane in the fully stretched state.

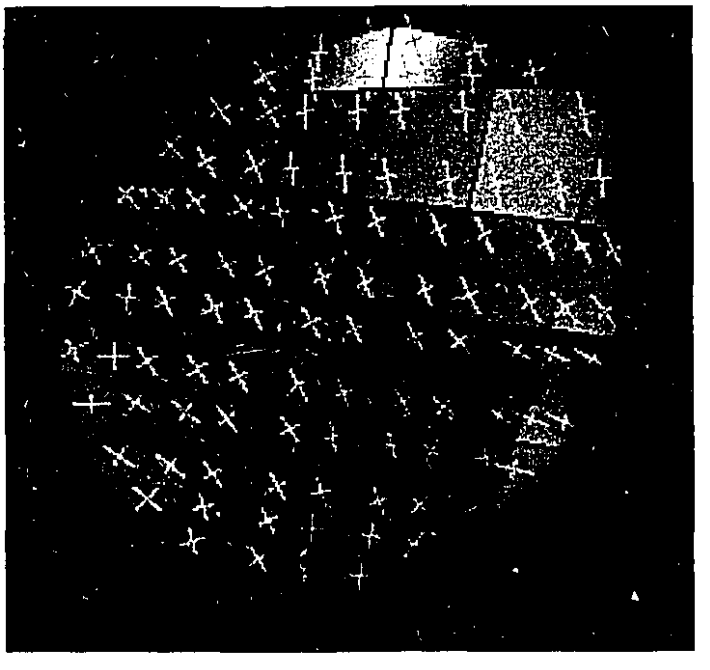

(b) Image of the magnitude of the largest principal strain at each point in the plane. Black pixels correspond to the smallest principal strain values (0.12), and white pixels correspond to the greatest principal strain values (0.29).

PLATE XI: Plane strain results for the canine pericardium membrane of experiment II. The fitted finite element meshes and the principal strains at the Gauss points are shown as overlays.

For consistency with the parameter estimation discussion below, the principal strains were shown within each element in the figures at the *Gauss points* (see below), the location of which are determined by numerical integration issues. In traditional finite element elasticity problems, stress and strain are related by some constitutive law in the equilibrium equation which is generally expressed as an integral over the element area. This integral must usually be solved numerically.

One of the most efficient and accurate method of numerical integration is the *Gauss integration formula* or *Gauss-Legendre quadrature* (Kreyszig, 1988). In this method, the numerical estimation of an integral over a closed interval requires the evaluation of the bounding function at selected points called the Gauss points. The number of Gauss points involved depends on the required degree of accuracy in the estimate. For example, in the case of 4 Gauss points over a two dimensional element domain, the function need only be evaluated at $\xi_i = \frac{1}{2} \pm \frac{1}{2\sqrt{3}}$.

6.3 Distributed parameter estimation

As stated earlier, the ultimate objective of the experimenter is to build a constitutive model of the system under investigation. The model can then be used to compare quantitatively the outcome of different experiments by comparing the values of the model parameters generated with the data from each experiment. The model can also be used to predict the behavior of the material under conditions other than that produced in the experiments. The model is based on one or more constitutive laws which reflect the various aspects of the material behavior of interest. The constitutive law parameters are calculated using parameter estimation techniques, as described below.

In the case of finite elasticity problems, as in the present case, the purpose of the constitutive law is to express as succinctly as possible the experimentally observed relationship between a material's stress and strain tensors, over the range of stress and strain likely to be encountered in the application of the law. As well as providing a faithful representation of the material behavior, the constitutive law must be numerically efficient and as well behaved as possible when used in numerical stress analysis. A further important consideration is that the constitutive law must allow stable parameter estimation: i.e.: small changes in the data should not produce large parameter changes.

6.3.1 General formulation of constitutive laws

The constitutive law relating stress and strain is often expressed by the *strain energy* function W. The strain energy, which depends on the thermodynamic process within the material, is a function of the strain tensor components. For an incompressible material, the Kirchhoff stress tensor components $T_{\alpha\beta}$ can be obtained from W by (Fung, 1981):

$$T_{NM} = \frac{\partial(\rho_o W)}{\partial e_{NM}} - p\frac{\partial X_N}{\partial x_r}\frac{\partial X_M}{\partial x_r}, \tag{6.24}$$

where e_{NM} are the Lagrangian strain tensor components, ρ_o is the undeformed material density, the X are the undeformed material coordinates, the x are the deformed material coordinates, and p is the hydrostatic pressure.

One approach to the formulation of the strain energy, which has met with considerable success in modeling the behavior of highly deformable rubbers, is to propose a relationship between the principal stresses and principal strains (Odgen, 1984). This approach relies however on the principal axes of stress coinciding with the principle axes of strain, which is not the case for anisotropic materials.

Other popular strain energy formulations involving strain invariants, polynomials or exponential functions have been used and are often mostly based on theoretical issues such as kinematic constraints and invariance with respect to the frame of reference (see reviews by Hunter and Smaill, 1989; Smaill and Hunter, 1991).

One such formulation, which is arguably the most popular strain energy function for describing the mechanical behavior of biological soft tissues and was first proposed by Fung (1967, 1973, 1981) is:

$$\begin{aligned}\rho_o W = &\frac{1}{2}\left(\alpha_1 e_{11}^2 + \alpha_2 e_{22}^2 + \alpha_3 e_{12}^2 + \alpha_3 e_{21}^2 + 2\alpha_4 e_{11} e_{22}\right) \\ &+ \frac{1}{2} C \exp(a_1 e_{11}^2 + a_2 e_{22}^2 + a_3 e_{12}^2 + a_3 e_{21}^2 + 2a_4 e_{11} e_{22} \\ &\qquad + \gamma_1 e_{11}^3 + \gamma_2 e_{22}^3 + \gamma_4 e_{11}^2 e_{22} + \gamma_5 e_{11} e_{22}^2) \quad ,\end{aligned} \tag{6.25}$$

where the α_i, a_i, and γ_i are constants and the e_{NM} are the Lagrangian strain tensor components. This formulation, or derivatives thereof, were used by Lanir (1979) for describing skin, Fung *et al.* (1979) for describing arteries, Chew *et al.* (1986) for pericardium, Humphrey *et al.* (1987) for pleura, Yin *et al.* (1987) for myocardium, and Choi and Vito (1990) for pericardium. Unfortunately, this formulation suffers however from wide variability in the estimated coefficients (Yin *et al.*, 1986).

6.3.2 Constitutive laws based on tissue micro-structure

Although such "black box" formulations may fit experimental data reasonably well given a sufficient number of free parameters, they bear little or no direct relation to the underlying structure of the material. An approach which incorporates knowledge of the material structure would potentially yield a more stable and parsimonious law. Moreover, the effect of changes in the proportions or properties of a certain component of the material would be easily understood if one or more material parameters in the constitutive law directly represented the mechanical properties of that component.

A compromise between the "black box" approach and the micro-structural approach is necessary because the complexity of the structure is too great to model in detail and our current knowledge of the mechanical properties of each component is too limited. However, the intracellular and extra-cellular structures of some soft biological tissues have been extensively investigated in recent years and several research groups have included details of the micro-structure in the formulation of a constitutive law (Shoemaker *et al.*, 1986; Humphrey and Yin, 1987; reviews by Hunter and Smaill, 1989, and Smaill and Hunter, 1991).

Pericardium has several features which make the task of defining a constitutive law formulation difficult. First, like most biological tissues, the stress-strain behavior is highly non-linear and anisotropic. Indeed, like other soft biological membranes, pericardium shows strain limiting behavior (sometimes referred to as a "hard spring"). That is, the force required to incrementally stretch the tissue in any direction increases markedly as the stretch approaches a limiting value, called the strain limit. Lanir (1979) hypothesized that this non-linear strain limiting behavior is due to the presence of collagen fibers which are compliant or slack when coiled or undulated, and stiff when pulled straight.

The constitutive law used here is the one proposed by Hunter *et al.* (1992) for use in modeling cardiac tissue. Its most distinguishing feature is that the strain energy function is defined with respect to a set of material coordinates (v_1, v_2, v_3) which are orthogonal at each point in the undeformed state and aligned with the local microstructural axes of the tissue, i.e.: the muscle fiber direction in the case of cardiac tissue, or the collagen fiber direction in the case of the pericardium. In keeping with all recent studies of pericardium, orthotropic material properties are assumed and the proposed strain energy function adopts a "pole-zero" form which exhibits strain limiting behavior along the micro-structurally defined axes.

There are three material parameters associated with each axis: one specifying the elastic strain limit, another the curvature of the uniaxial stress-strain curve in that axis, and a third the relative contribution of that axis to the total strain energy. Additional strain energy terms governing the shearing behavior of the tissue are included in the strain energy function, which has the following form:

$$W = k_1 \frac{e_{11}^2}{(a_1 - e_{11})^{\alpha_1}} + k_2 \frac{e_{22}^2}{(a_2 - e_{22})^{\alpha_2}} + k_3 \frac{e_{33}^2}{(a_3 - e_{33})^{\alpha_3}} + k_4 \frac{e_{12}^2}{(a_4 - e_{12})^{\alpha_4}} + k_5 \frac{e_{23}^2}{(a_5 - e_{23})^{\alpha_5}} + k_6 \frac{e_{31}^2}{(a_6 - e_{31})^{\alpha_6}}, \tag{6.26}$$

where the e_{NM} are the components of the Lagrangian strain tensor referred to the material coordinates aligned with the structurally defined axes of the tissue, the a_i are parameters expressing the limiting strain for a particular type of deformation, the α_i are parameters

expressing the curvature of the uniaxial stress-strain curves, and the k_i are parameters giving the relative contribution of each strain energy term.

Since in this application the material under consideration is a membrane, where the thickness of the tissue is small compared to its overall area, the k_5 and k_6 terms are assumed to be equal to zero. Furthermore, a linear stress-strain behavior in compression is assumed by setting α_3 to zero, hence the pole value a_3 is irrelevant. Therefore, the constitutive law has 10 free parameters.

6.3.3 Material parameter estimation

As mentioned above, the parameter estimation is an iterative process. In the method proposed by Hunter *et al.* (1992), the 10 free parameters in the strain energy function are determined by minimizing the sum of squared differences between the observed and predicted boundary forces. The model force predictions are obtained by numerically solving the mechanical equation of equilibrium with Gaussian quadrature over each element. This equation relates the stress to the applied boundary forces (Oden, 1972) by:

$$\int_{\Omega}\left(T_{NM}\frac{\partial x_k}{\partial v_N}\frac{\partial \psi_n}{\partial v_M}\right)d\Omega = f_k^n, \tag{6.27}$$

where the f_k^n are the components of boundary forces at node n, the x_k are the deformed material coordinates, the ψ_k are the interpolation basis functions, the T_{NM} are the stress components which are obtained from the strain energy function using (6.24), and Ω is the element area.

The material parameters are determined by the following estimation technique: the plane strain field is estimated throughout the membrane sample with speckle interferometry using the procedure described in previous sections, for a set of applied loads. For a given set of constitutive law parameters, (6.24) yields the stress field across the membrane and (6.27) the nodal forces required to maintain equilibrium. An error measure is obtained by summing the squared differences between the forces predicted by the model and the forces applied experimentally. Minimizing this error with respect to the set of unknown parameters yields the required parameters estimates.

The minimization for the data from experiment II was executed using the CMISS finite element analysis program, by Dr. Peter Hunter at the University of Auckland. The parameter values which minimized the sum of squared residuals for the strain field and boundary forces measured at maximum extension were the following:

$k_1 = 2.818$	$a_1 = 0.16$	$\alpha_1 = 0.943$
$k_2 = 28.98$	$a_2 = 0.21$	$\alpha_2 = 0.348$
$k_4 = 0.00264$	$a_4 = 0.05$	$\alpha_4 = 0.586$

and where $K_3 = 0$, assuming that there is no compressive resistance in the transmembrane direction. The differences between the (k_1, a_1, α_1) and (k_2, a_2, α_2) terms indicates that the membrane is highly anisotropic.

Note that the above set of parameters were only optimal for a single set of experimentally measured strain field and boundary forces, namely the set measured at maximum extension. In order to verify how well this set of material parameters represented the behavior of the membrane at other strain levels, the *percentage variance accounted for* (%VAF) by the pole-zero model was plotted for various stretch steps from experiment II in Figure 6.10 below.

In Figure 6.10, the %VAF expresses the percentage ratio between the sum of squared residuals and the sum of squared boundary forces, subtracted from 100%. At the boundary nodes, the residuals are the differences between the predicted and measured boundary forces. At the interior nodes however, the residuals are simply the predicted force values at these nodes (since there are no externally applied forces).

The two curves in the Figure show the %VAF values for two slightly different situations. The dashed curve expresses the %VAF by the pole-zero model when all elements in the mesh are included (i.e.: the normal case). The fit however is not very good because of unusually high residuals at the nodes of the boundary elements. This is probably due to a combination of the tissue opening and tearing at the holes, as well as the outer ring of buckled tissue just outside the tether points, resulting in rather unnaturally complex material behavior.

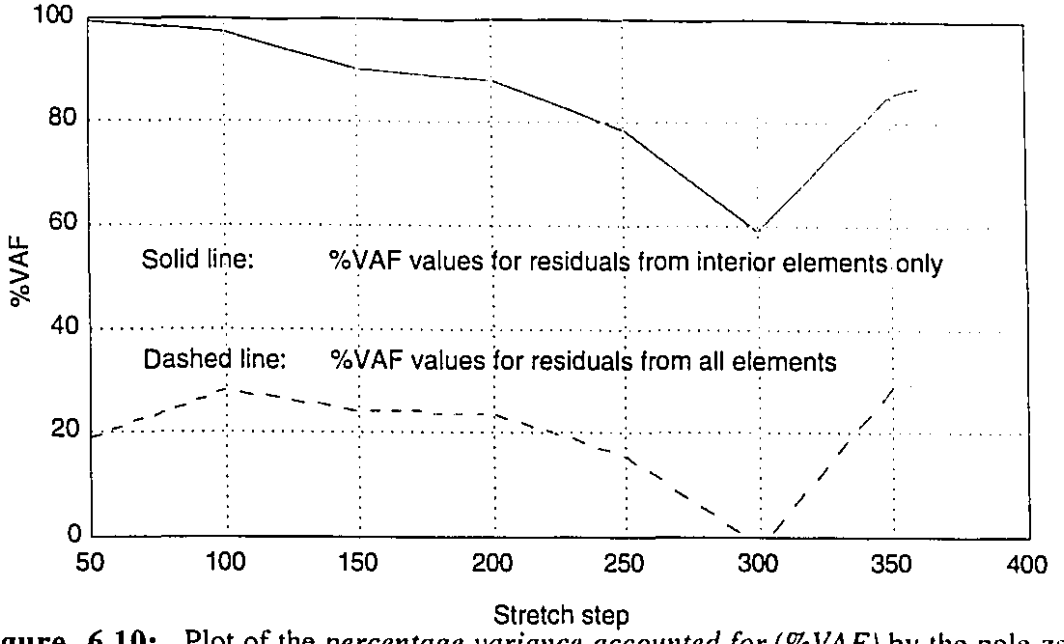

Figure 6.10: Plot of the *percentage variance accounted for (%VAF)* by the pole-zero model across the entire range of applied strains, for the data from experiment II. Courtesy of Dr. Peter Hunter, University of Auckland, New Zealand.

In order to evaluate the performance of the pole-zero law for the more natural conditions prevailing in the area just within the tether points, the %VAF for the interior mesh elements was calculated and plotted as a solid line in Figure 6.10. It can be seen from the Figure that the fit for the interior elements is very good. It must be emphasized however that the strain was successfully measured at every point on the membrane surface. It is the modeling, not the measurement procedure, that breaks down at the edges due to unnaturally complex mechanical conditions. With an inhomogeneous model including parameters and properties specifically designed to represent the material behavior at the edges, a better overall fit would be achieved.

Chapter 7

Conclusions

As stated in Chapter 1, the study of biological membranes is an important field in the science of Biomechanics. Indeed, in order to understand the normal function and mechanisms of failure of these membranes, as well as to certify artificial replacement materials, the mechanical properties of biological membranes must be well understood. Unfortunately, existing methods of study are either inadequate or incomplete. For this reason, a novel method of studying the mechanical properties of biological membranes was developed and presented in this work. In this last Chapter, the major elements of this thesis are reviewed, original contributions of this work are listed, and recommendations for future work are given.

7.1 Thesis overview

The task of fully characterizing biological membranes is particularly challenging because of the anisotropic and non-linear nature of their material properties. The method described in this thesis is particularly well suited to the task because of the multiple degrees of freedom in the applied stress mechanism and the usage of a speckle interferometry-based full field displacement measurement technique. In this way, few if any restrictions are imposed on the experimentally applied stress and strain fields, allowing thorough mechanical characterization of the membrane under investigation.

The experimental apparatus was described in terms of its four separate subsystems: data acquisition and control hardware and software, optics, and mechanics. The digital and analog control of the apparatus, as well as the subsequent data analysis, were executed by the custom designed XVG graphical interface program, running on an IBM RISC System/6000 workstation.

In the course of this work, a novel method of phase unwrapping was developed for analyzing the optical phase images. Unlike existing methods, this new technique is specially suited to phase images with a high noise content. Although it was developed specifically for speckle phase unwrapping, it is equally applicable to many other areas such as holography, Moiré methods, synthetic aperture radar interferometry, etc. Because of its robustness, it allows the analysis to be completely automated.

Finally, one of the many challenging aspects of this project was to develop a method of analyzing the large volume of data generated by the experimental apparatus. The approach taken here was based on the finite element method. Unlike traditional applications where the finite element method is used to predict the behavior of a material with known constitutive properties, finite elements were used here for distributed parameter estimation in order to identify and quantify the unknown properties of the material under test.

The finite element representation of the data was used to generate predicted paths of certain material points, based on the experimental data. These material point displacement predictions were compared with actual displacement measurements from the video record of the experiments and found to be in excellent agreement, thus validating the entire method. Analytical expressions based on the finite element representation of the data were also used to calculate the full finite strain tensor at every point in the plane. Results at each step of the complete procedure from two typical experiments on canine pericardium membranes were presented. Theoretical noise calculations for all phases in the experimental method were derived, and confirming experimental measurements were shown whenever possible.

7.2 Original contributions

- Complete two-dimensional mechanical testing method for membranes where arbitrary planar stress fields may be applied and resulting strain fields are measured in a full-field manner.
- Speckle interferometry used in transmission mode with a biological specimen.
- Robust phase unwrapping mechanism allowing fully automated analysis of phase images with a high noise content.
- Finite element representation of two dimensional displacement data measured with speckle interferometry.
- Material property modeling using a pole-zero constitutive law for canine pericardium

7.3 Suggestions for future work

As stated in Chapter 5, there are many different subsystems interfacing together in this apparatus, each one rather complex in its own right. In order for this first prototype to have a reasonable chance of success, it was felt that the different components should not be initially implemented to their fullest level of complexity. Now that the technique has been validated however, the objective is to rebuild the apparatus to exploit its full potential.

For example, in the experiments presented in this thesis, the applied stress fields were roughly uniform, so that the resulting strain fields were also fairly well behaved. In future experiments however, much more general stress fields will be applied to the membrane in order to emphasize any arbitrary aspect of the material behavior. As a consequence, it is expected that higher-order basis functions in the finite element interpolation such as bicubic Hermites will be required to represent adequately the data. The number of pulling actuators could also be increased in order to apply greater maximum strain levels with less edge effects at the tether points.

Similarly, the experiments presented in this thesis demonstrated quasi-static testing only. Therefore, the next step required to make mechanical characterization with this technique truly complete would be to study the *dynamic response* of the material under investigation. The only required modification to the mechanical perturbation subsystem to enable dynamic testing of materials would be to add explicit force transducers in the linkages. Indeed, for dynamic studies, the current-to-force relationship of the actuators would be difficult to use for estimating applied forces accurately. The pulling actuators employed in the apparatus would be suitable for dynamic testing since they have a flat bandwidth (as measured on the galvanometer shaft) to 100 kHz and a usable bandwidth for frequency response measurements to 1 kHz.

The main speed bottleneck in the speckle data acquisition subsystem was the slow image transfer rate of the frame grabber, which was the best device available at the time for the IBM workstation. With a better quality fast-transfer frame grabber board (if necessary on an alternative workstation platform), the image acquisition time could be reduced significantly and sampling could be done at much higher rates. With additional improvements such as dual wavelength laser light and two cameras, displacements in the two orthogonal directions in the plane could be sampled simultaneously, as opposed to

sequentially. Such improvements to the speckle data acquisition subsystem would make dynamic testing possible.

To conclude then, this thesis presents the description and experimental validation of a novel apparatus and technique which can mechanically characterize biological membranes to a degree never before attained. The current limitations to the apparatus are purely technological, and with the suggested improvements, the full potential of this technique could be exploited in order to provide full-field dynamic mechanical testing. This in turn would provide the fields of medicine and physiology with a highly useful clinical tool for complete materials testing of membrane tissues.

Appendix

XVG Control Program Interface Windows

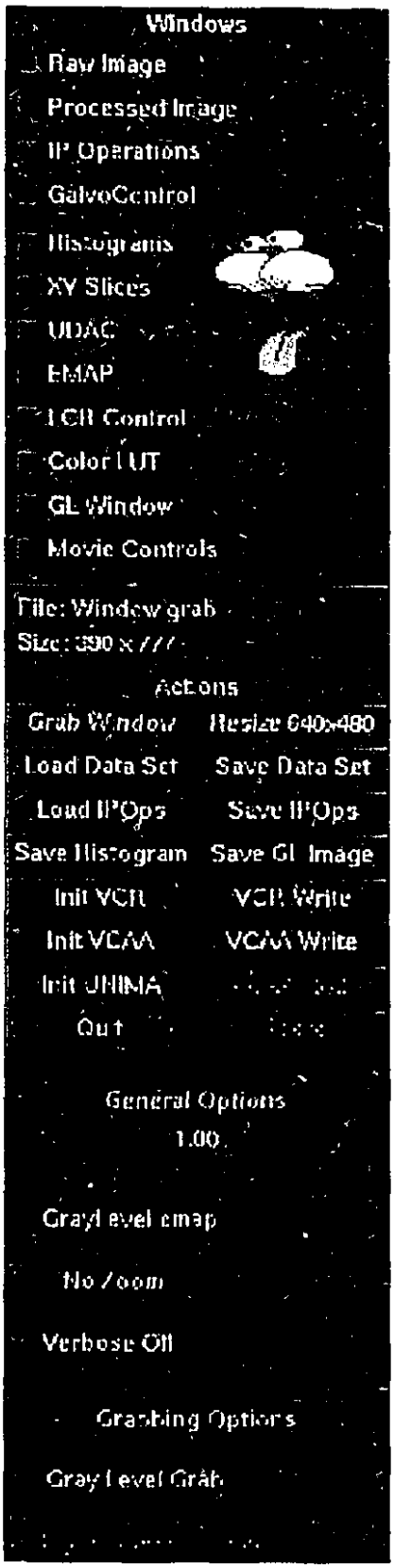

XVG main interface window

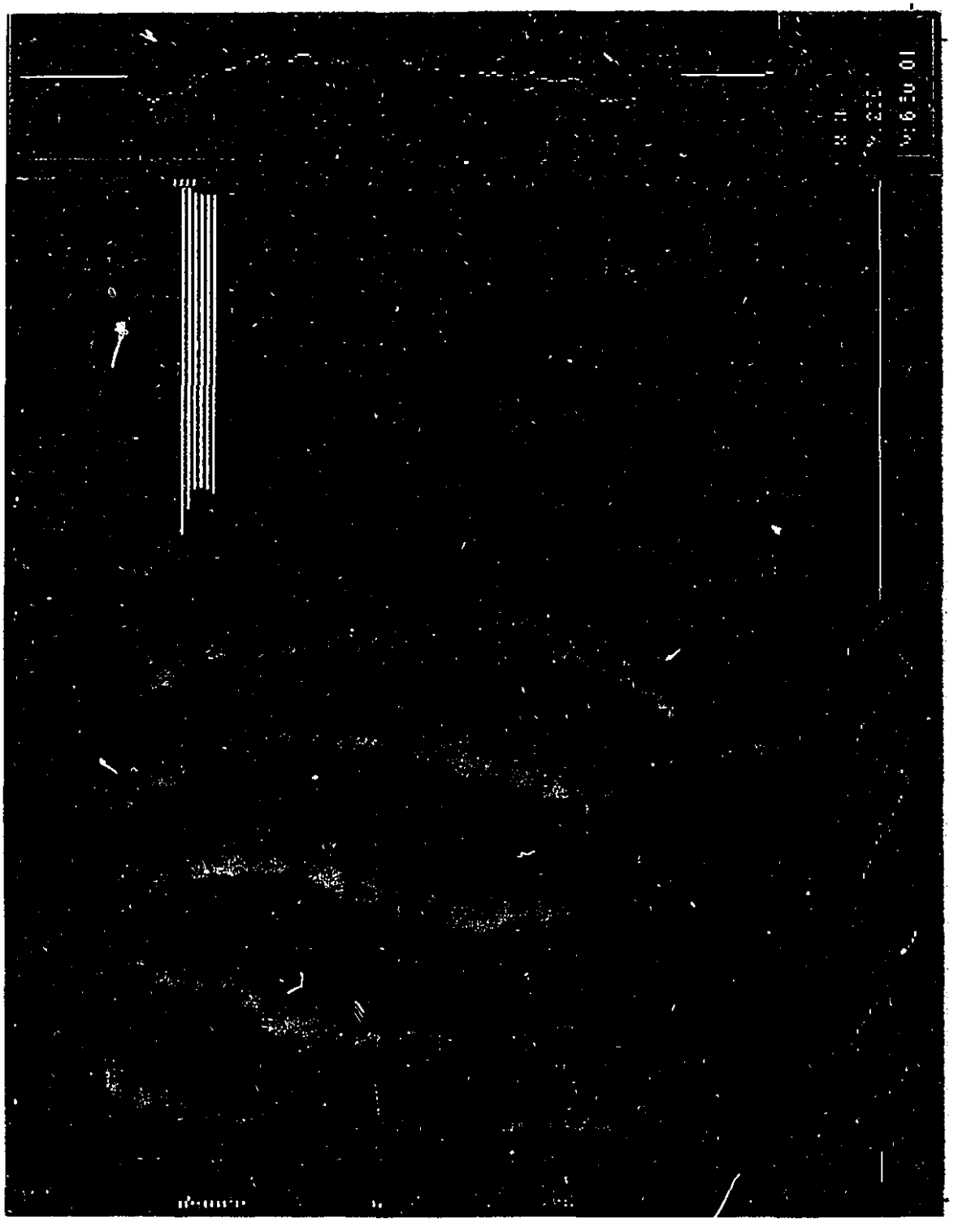

Processed image window

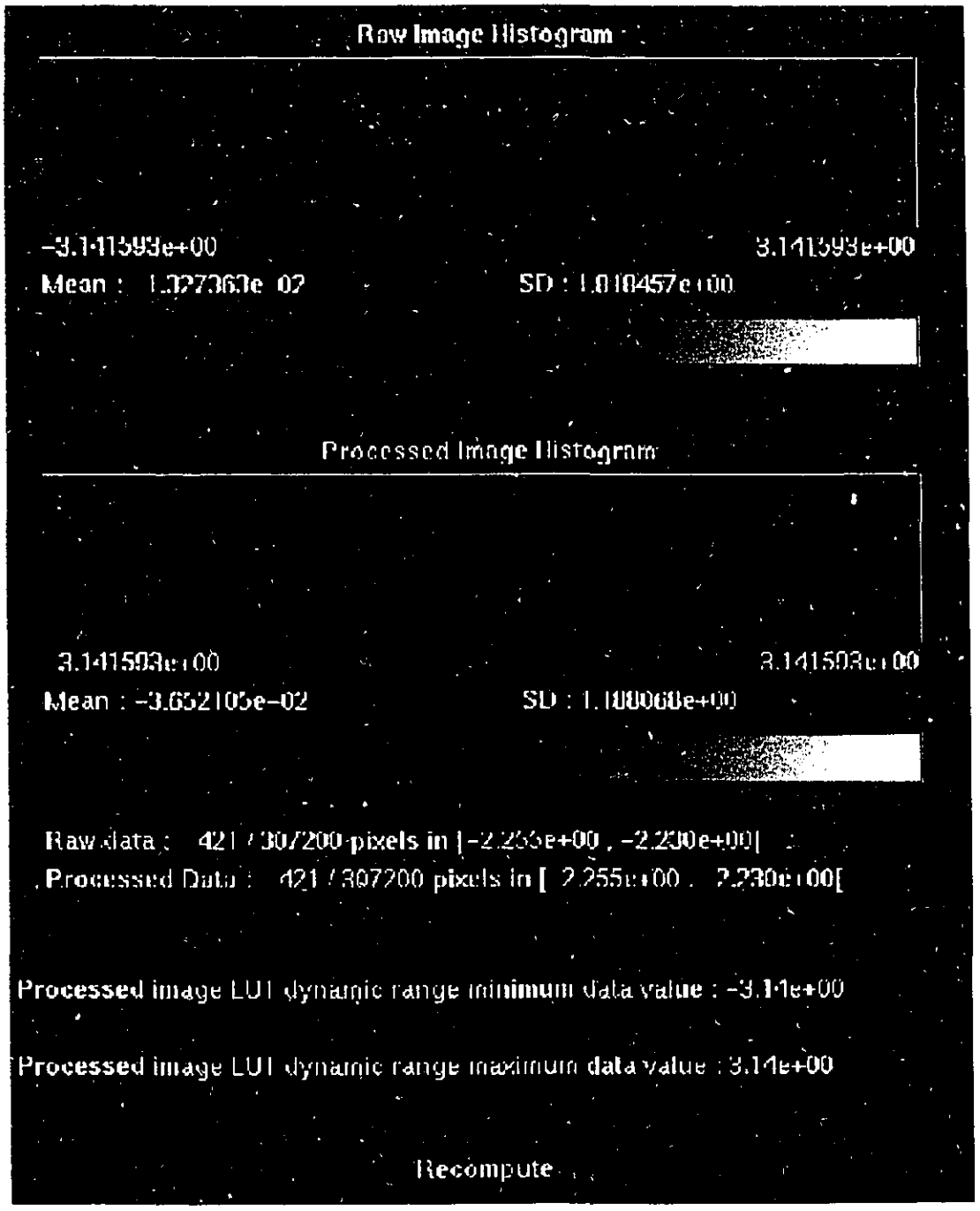

Histogram window

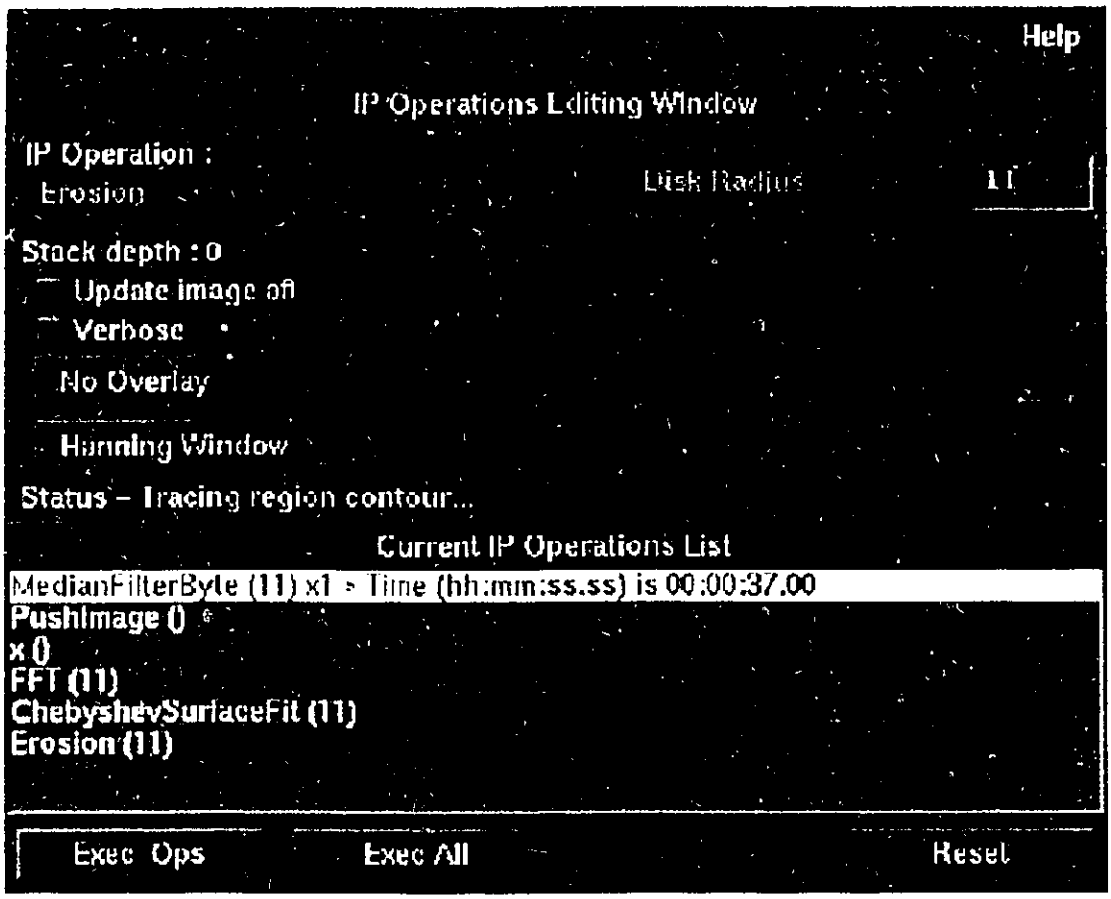

Image processing window

UDAC D/A control window

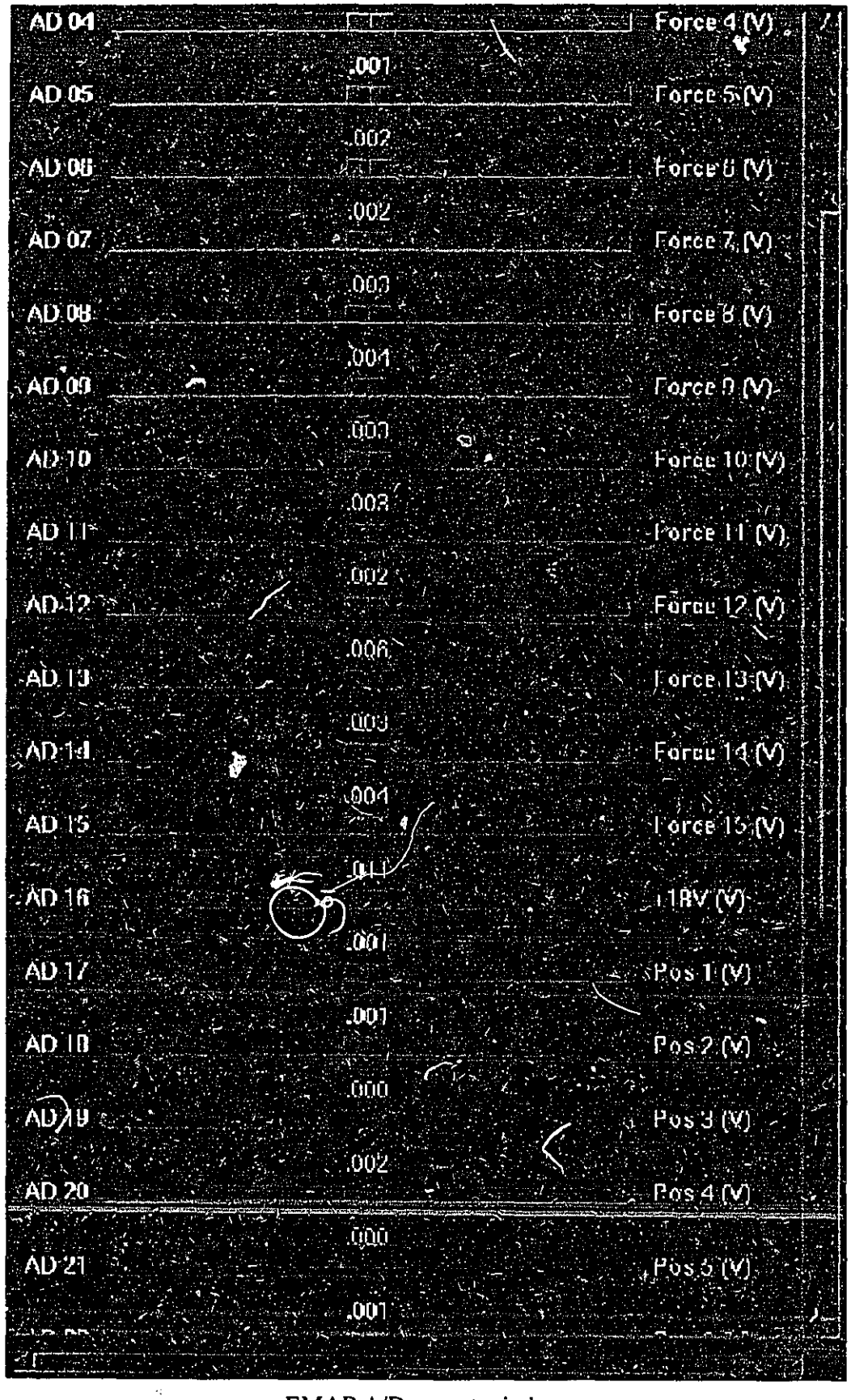

EMAP A/D output window

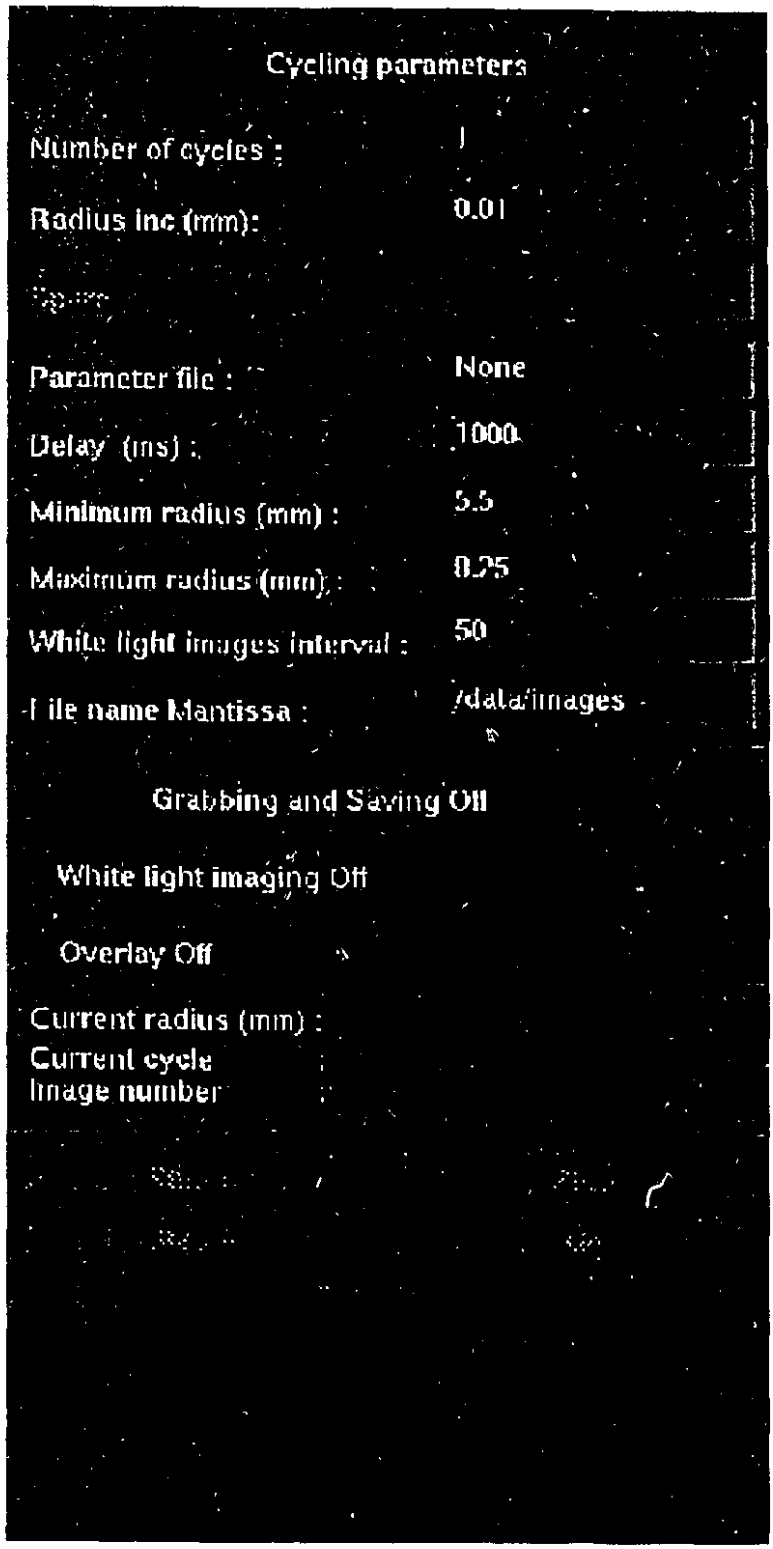

Experimental control window

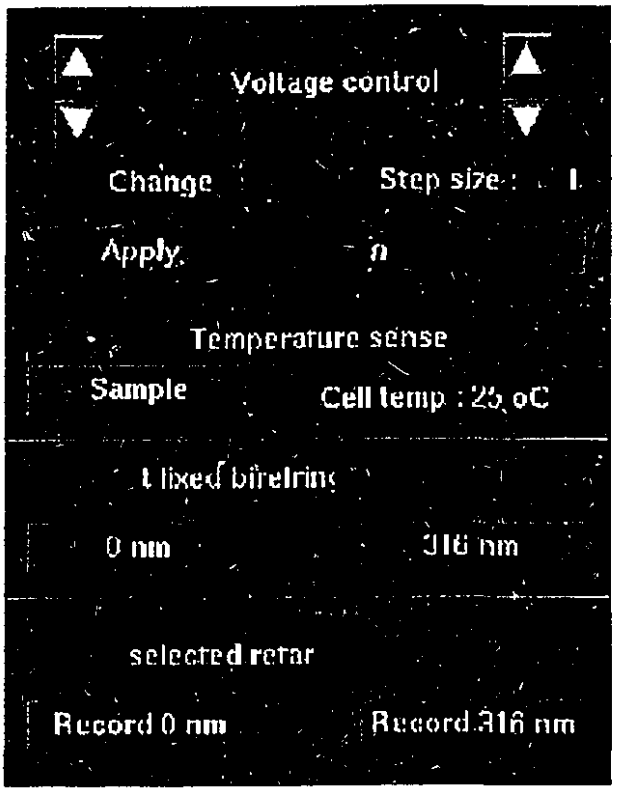

LCR control window

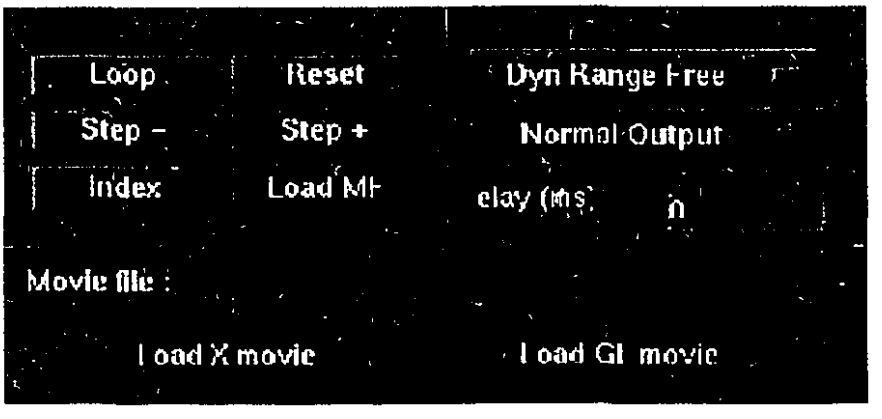

Movie control window

Color lookup table control window

3D transformation and viewing control window

References

Atkin, R.J. and Fox, N. *An Introduction to the Theory of Elasticity*. Essex: Longman Scientific & Technical, 1980.

Bergquist, B.D., Montgomery, P.C., Mendoza-Santoyo, F., Henry, P. and Tyrer, J.R. The present status of electronic speckle pattern interferometry (ESPI) with respect to automated inspection and measurement. *SPIE: Automatic Optical Inspection*, 1986, *654*, 95-100.

Bone, D.J. Fourier fringe analysis: the two-dimensional phase unwrapping problem. *Applied Optics*, 1991, *30*, 3627-3632.

Brenan, C.J.H., Charette, P.G. and Hunter, I.W. Environmental isolation platform for microrobot system development. *Review of Scientific Instruments*, 1992, *63*, 3492-8.

Butters, J.N. and Lenndertz, J.A. Holographic and video techniques applied to engineering measurement. *Measurement and Control*, 1971, *4*, 349-354.

Butters, J.N., Jones, R. and Wykes, C. Electronic speckle pattern interferometry. *Speckle Metrology*, Editor: R.K. Erf. New York: Academic Press, 1978.

Button, B.L., Cutts, J., Dobbins, B.N., Moxon, C.J. and Wykes, C. The identification of fringe positions in speckle patterns. *Optics and Laser Technology*, 1985, *17*, 189-192.

Canny, J. A computational approach to edge detection. *IEEE Transactions on Pattern Analysis and Machine Intelligence*, 1986, *PAMI-8*, 679.

Carré, P. Installation et utilisation du comparateur photoélectrique et interférentiel du Bureau International des Poids et Mesures. *Metrologia*, 1966, *2*, 13-23.

Charette, P.G. An integrated fringe counting and interpolation laser heterodyne interferometer for micro-robot position measurement. Masters Thesis, 1990.

Charette, P.G., Hunter, I.W. and Brenan, C.J.H. A complete high performance heterodyne interferometer displacement transducer for microactuator control. *Review of Scientific Instruments*, 1992, *63*, 241-248.

Chew, P.H., Yin, F.C.P. and Zeger, S.L. Biaxial stress-strain properties of canine pericardium. *Journal of Molecular and Cellular Cardiology*, 1986, *18*, 567-578.

Choi, H.S. and Vito, R.P. Two-dimensional stress-strain relationship for canine pericardium. *Journal of Biomechanical Engineering*, 1990, *112*, 153-159.

Conerty, M., Castracane, J. and Saravia, E. Development of an otolaryngological interferometric fiber optic diagnostic probe. *SPIE: Optical Fibers in Medecine VII*, 1992.

Crawford, F.A., Sade, R.M. and Spinale, F. Bovine pericardium for correction of congenital heart defects. *Annals of Thoracic Surgery*, 1986, *41*, 602-605.

Creath, K. Phase-shifting speckle interferometry. *Applied Optics*, 1985, *24*, 3053-3058.

Creath, K. Phase-shifting speckle interferometry. *SPIE: International Conference on Speckle*, 1985, *556*, 337-346.

Creath, K. Phase measurement interferometry techniques. *Progress in Optics XXVI*, Ed: E.Wolf. London: Elsevier Science Publishers, 1988, 349-393.

Dainty, J.C. *Topics in Applied Physics: Laser Speckle and Related Phenomena*. Berlin: Springer-Verlag, 1975.

Dougherty, E.R. *An Introduction to Morphological Image Processing*. Bellingham: SPIE Optical Engineering Press, 1992.

Ennos, A.E. Measurement of in-plane surface strain by hologram interferometry. *Journal of Scientific Instruments*, 1968, *1*, 731-734.

Ennos, A.E. Speckle interferometry. *Progress in Optics XVI*, Ed: E. Wolf. North-Holland, 1978.

Erf, R.K. *Speckle Metrology*. New York: Academic Press, 1978.

Foley, J.D., vanDam, A., Feiner, S.K. and Hughes, J.F. *Computer Graphics: Principles and Practice, Second Edition*. Reading, Mass: Addison-Wesley Publishing Company, 1990.

Franklin, C.E. and Davie, P.S. The pericardium facilitates pressure work in the eel heart. *Journal of Fish Biology*, 1991, *39*, 559-564.

Frieden, B.R. *Probability, Statistical Optics, and Data Testing, Second Edition*. Berlin: Springer-Verlag, 1991.

Fuji, H. and Asakura, T. Effect of surface roughness on the statistical distribution of image speckle intensity. *Optics Communications*, 1974, *11*, 35-38.

Fung, Y.C. Elasticity of soft tissue in simple elongation. *Ameraican Journal of Physiology*, 1967, *213*, 1532-1544.

Fung, Y.C. Biorheology of soft tissue. *Biorheology*, 1973, *10*, 139-155.

Fung, Y.C., Fronek, K. and Patitucci, P. Pseudoelasticity of arteries and the choice of its methamatical expression. *American Journal of Physiology: Heart and Circulation Physiology*, 1979, *6*, H620-H631.

Fung, Y.C. *Biomechanics: Mechanical Properties of Living Tissue*. New York: Springer-Verlag, 1981.

Ganesan, A.R., Kothiyal, M.P. and Sirohi, R.S. Simple image processing techniques for the contrast enhancement of real-time digital speckle pattern interferometry fringes. *Optical Engineering*, 1989, *28*, 1019-1022.

Ghiglia, D.C., Mastin, G.A. and Romero, L.A. Cellular-automata method for phase unwrapping. *Journal of the Optical Society of America A*, 1987, *4*, 267-280.

Gierloff, J.J. Phase unwrapping by regions. *SPIE: Current developments in Optical Engineering*, 1987, *818*, 2-9.

Goldstein, R.M., Zebker, H.A. and Werner, C.L. Satellite radar interferometry: Two-dimensional phase unwrapping. *Radio Science*, 1988, *23*, 713-720.

Gonzales, R.C. and Woods, R.C. *Digital Image Processing*. Reading, Mass.: Addison-Wesley Publishing Company, 1992.

Goodman, J.W. *Topics in Applied Physics: Laser Speckle and Related Phenomena.* Editor J.C. Dainty. Berlin: Springer-Verlag, 1975.

Hariharan, P., Oreb, B.F. and Eiju, T. Digital phase-shifting interferometry: a simple error-compensating phase calculation algorithm. *Applied Optics*, 1987, *26*, 2504-2507.

Hecht, E. *Optics*. Reading, Mass: Addison-Wesley, 1987.

Hildebrand, J., Fukaya, H. and Martin, C.J. Stress-strain relations of tissue sheets undergoing uniform two-dimensional stretch. *Journal of Applied Physiology*, 1969, *27*, 758-762.

Hoffman, A.H. and Grigg, P. A method for measuring strains in soft tissue. *Journal of Biomechanics*, 1984, *17*, 795-800.

Holt, J.P. The normal pericardium. *The American Journal of Cardiology*, 1970, *26*, 455-465.

Humphrey, J.D. and Yin, F.C.P. On constitutive relations and finite deformations of passive cardiac tissue: I. A pseudo strain-energy function. *Transactions of the ASME*, 1987, *109*, 298-304.

Humphrey, J.D. and Yin, F.C.P. A new constitutive formulation for characterizing the mechanical behavior of soft tissue. *Biophysical Journal*, 1987, *52*, 563-570.

Humphrey, J.D., Vawter, D.L. and Vito, R.P. Pseudoelasticity of excised visceral pleura. *Journal of Biomechanical Engineering*, 1987, *109*, 115-120.

Humphrey, J.D., Vawter, D.L. and Vito, R.P. Quantification of strains in biaxially tested soft tissues. *Journal of Biomechanics,* 1987, *20*, 59-65.

Hung, Y.Y. Displacement and strain measurement. *Speckle Metrology*, Editor: R.K. Erf. New York: Academic Press, 1978.

Hunter, P.J. and Smaill, B.H. The analysis of cardiac function: a continuum approach. *Progress in Biophysical and Molecular Biology*, 1988, *52*, 101-164.

Hunter, P.J., Hunter, I.W. and Smaill, B.H. A "pole-zero" constitutive law for myocardium. 1992, under revision.

Hunter, P.J., Hunter, I.W. and Smaill, B.H. Constitutive law parameter estimation in biaxial testing of soft tissue. 1992, under revision.

Huntley, J.M. Noise-immune phase unwrapping algorithm. *Applied Optics*, 1989, *28*, 3268-3270.

Huntley, J.M. and Saldner, H. Temporal phase-unwrapping algorithm for automated interferogram analysis. *Applied Optics*, 1993, *32*, 3047-3052.

IBM RISC System/6000 manual: AIXwindows Interface Composer Developer's Guide, Version 1.2, 1993.

Jin, G and Tang, S. Electronic speckle pattern interferometer with a polarization phase-shift technique. *Optical Engineering*, 1992, *31*, 857-860.

Joenathan, C. Effect of non-linearity of the TV camera in electronic speckle pattern interferometry. *Optik*, 1990, *85*, 33-37.

Joenathan, C., Pfister, B. and Tiziani, H.J. Contouring by electronic speckle pattern interferometry employing dual beam illumination. *Applied Optics*, 1990, *29*, 1905-1911.

Joenathan, C. Vibration fringes by phase stepping on an electronic speckle pattern interferometer: an analysis. *Applied Optics*, 1991, *30*, 4658-4665.

Johnson, H.S., Gilbert, J.A., Matthys, D.R. and Dudderar, T.D. Real-time Moiré interferometry. *Experimental Mechanics*, 1989, *29*, 231-236.

Jones, R. and Wykes, C. *Holographic and Speckle Interferometry, Second Edition.* Cambridge: Cambridge University Press, 1989.

Kanazawa, M., Shirato, K., Ishikawa, K., Nakajima, T., Haneda, T. and Takishima, T. The effect of pericardium on the end-systolic pressure-segment length relationship in canine left ventricle in acute volume overload. *Circulation*, 1983, *68*, 1290-1298.

Kasprzak, H., Förster, W.N. and von Bally, G. Holographic measurement of changes of the corneal curvature due to intraocular pressure differences. *Optical Engineering*, 1994, *33*, 198-203.

Kerr, D. and Tyrer, J.R. The application of phase stepping to the analysis of ESPI fringe patterns. *SPIE: Photomechanics and Speckle Metrology*, 1987, *814*, 379-389.

Kerr, D., Mendoza Santoyo, F. and Tyrer, J.R. Manipulation of the Fourier components of speckle fringe patterns as part of an interferometer analysis process. *Journal of Modern Optics*, 1989, *36*, 195-203.

Kerr, D., Mendoza Santoyo, F. and Tyrer, J.R. Extraction of phase data from electronic speckle pattern interferometric fringes using a single-phase-step method: a novel approach. *Journal of the Optical Society of America A*, 1990, *7*, 820-826.

Kobayashi, A.S. Hybrid experimental-numerical stress analysis. *Experimental Mechanics*, 1983, *23*, 338-347.

Kreis, T.M. and Jüptner, W.P.O. Fourier-transform evaluation of interference patterns: the role of filtering in the spatial domain. *SPIE: Laser Interferometry: Quantitative Analysis of Interferograms*, 1989, *1162*, 116-125.

Kreske, K., Keren, E. and Kafri, O. Insights on Moiré deflectometry. *Lasers & Optronics*, October 1988, 63-66.

Kreyszig, E. *Advanced Engineering Mathematics, Sixth Edition.* New York: John Wiley & Sons, 1988.

Krishnaswamy, S. Algorithm for computer tracing of interference fringes. *Applied Optics*, 1991, *30*, 1624-1628.

Lanir, Y. and Fung, Y.C. Two-dimensional mechanical properties of rabbit skin-I. Experimental system. *Journal of Biomechanics*, 1974, *7*, 29-34.

Lanir, Y. and Fung, Y.C. Two-dimensional mechanical properties of rabbit skin-II. Experimental results. *Journal of Biomechanics*, 1974, *7*, 171-182.

Lanir, Y. Biaxial stress-strain constitutive relationship in the skin. *Israël. Journal of. Technology*. 1979, *17*, 78-85.

Lanir, Y. A structural theory for the homogeneous biaxial stress-strain relationships in flat collegenous tissues. *Journal of Biomechanics*, 1979, *12*, 423-436.

Larkin, K.G. and Oreb, B.F. A new seven sample symmetrical phase-shifting algorithm. *SPIE: Techniques and Analysis*, 1992, *1755*, 2-11.

Larkin, K.G. and Oreb, B.F. Propagation of errors in different phase-shifting algorithms: a special property of the arctangent function. *SPIE: Interferometry: Techniques and Analysis*, 1992, *1755*, 219-227.

Lee, M.-C., LeWinter, M.M., Freeman, G., Shabetai, R. and Fung, Y.C. Biaxial mechanical properties of the pericardium in normal and volume overload dogs. *American Journal of Physiology*, 1985, *249*, H222-H230.

Leendertz, J.A. Interferometric displacement measurement on scattering surfaces utilizing speckle effect. *Journal of Physics E: Scientific Instruments*, 1970, *3*, 214-218.

Lin. Q., Vesecky, J.F. and Zebker, H.A. Phase unwrapping through fringe-line detection in synthetic aperture radar interferometry. *Applied Optics*, 1994, *33*, 201-208.

Macy, W.W. Two-dimensional fringe-pattern analysis. *Applied Optics*, 1983, *22*, 3898-3901.

Mann, D., Lew, W., Ban-Hayashi, E., Shabetai, R., Waldman, L. and LeWinter, M. In vivo mechanical behavior of canine pericardium. *American Journal of Physiology*, 1986, *251*, H349-H356.

Martel, S., Hunter, I.W., Lafontaine, S. and Hunter P.J. EMAP: An electrophysiological mapping system. *18th Conference of the Canadian Medical and Biological Engineering Society*, Totonto, 1992, 102-103.

Matthys, D. R., Dudderar, T.D., Gilbert, J.A., Taher, M.A. and Johnson, H.S. Speckle metrology combined with finite-element modeling for stress analysis. *Optical Engineering*, 1986, *25*, 749-753.

Mendoza Santoyo, F., Kerr, D. and Tyrer, J.R. Interferometric fringe analysis using a single phase step technique. *Applied Optics*, 1988, *27*, 4362-4364.

Mendoza Santoyo, F., Shellabear, M.C. and Tyrer, J.R. Whole field in-plane vibration analysis using pulsed phase-stepped ESPI. *Applied Optics*, 1991, *30*, 717-721.

Meunier, J., Bertrand, M., Mailloux, G.E. and Petitclerc, R. Local myocardial deformation computed from speckle motion. *Proceedings of the 1988 IEEE Computers in Cardiology Conference*, 1988, 133-136.

Moore, A.J. and Tyrer, J.R. An electronic speckle pattern interferometer for complete in-plane displacement measurement. *Measurement Science Technology*, 1990, *1*, 33-39.

Nielsen, P.M.F., Hunter, P.J. and Smaill, B.H. Biaxial testing of membrane biomaterials: Testing equipment and procedures. *Journal of Biomechanical Engineering*, 1991, *113*, 295-300.

Odgen, R.W. *Nonlinear Elastic Deformations*. New York: Ellis Horwood. 1984.

Owner-Petersen, M. Decorrelation and fringe visibility: on the limiting behavior of various electronic speckle-pattern correlation interferometers. *Journal of the Optical Society of America A*, 1991, *8*, 1082-1089.

Petrou, M. and Kittler, J. Optimal edge detector for ramp edges. *IEEE Transactions on Pattern Analysis and Machine Intelligence*, 1991, *13*, 483-491.

Preater, R. and Swain, R. Fourier transform fringe analysis of ESPI fringes from rotating components. *SPIE:Industrial Applications of Optical Inspection Metrology and Sensing*, 1992, *1821*,82-100.

Preater, R. and Swain, R. Fourier transform fringe analysis of electronic speckle pattern interferometry fringes from high-speed rotating components. *Optical Engineering*, 1994, *33*, 1271-1279.

Press, H., Teukolsky, S.A., Vetterling, W.T. and Flannery, B.P *Numerical Recipes in C, Second Edition*. Cambridge: Cambridge University Press, 1992.

Pryputniewicz, R.J. Speckle metrology techniques and their applications. *SPIE: International Conference on Speckle*, 1985, *556*, 90-98.

Purinya, B., Kasyanov, V., Volkolakov, J., Latsis, R. and Tetere, G. Biomechanical and structural properties of the explanted bioprosthetic valve leaflets. *Journal of Biomechanics*, 1994, *27*, 1-11.

Ramesh, K. and Pramod, B.R. Digital image processing of fringe patterns in photomechanics. *Optical Engineering*, 1992, *31*, 1487-1497.

Ratnam, M.M., Evans, W.T. and Tyrer, J.R. Measurement of thermal expansion of a piston using holographic and electronic speckle pattern interferometry. *Optical Engineering*, 1992, *31*, 61-69.

Reid, G.T. Automatic fringe pattern analysis : A review. *Optics and Lasers in Engineering*, 1986/7, *7*, 37-68.

Schmit, J. and Creath, K. Spatial and temporal phase-measurement techniques: a comparison of major error sources in one dimension. *SPIE: Interferometry: Techniques and Analysis*, 1992, *1755*, 202-211.

Schwider, J., Falkenstörfer, O., Shreiber, H., Zöller, A. and Streibl, N. New compensating four-phase algorithm for phase-shift interferometry. *Optical Engineering*, 1993, *32*, 1883-1885.

Sciammarella, C.A. and Narayanan, R. The determination of the components of the strain tensor in holographic interferometry. *Experimental Mechanics*, 1984, *24*, 257-264.

Shoemaker, P.A., Schneider, D., Lee, M.C. and Fung, Y.C. A constitutive model for two-dimensional soft tissues and its application to experimental data. *Journal of Biomechanics*, 1986, *19*, 695-702.

Sirkis, J.S., Chen, Y.-M., Singh, H. and Cheng, A.Y. Computerized optical fringe pattern analysis in photomechanics: a review. *Optical Engineering*, 1992, *31*, 304-314.

Smaill, B.H. and Hunter, P.J. Structure and function of the diastolic heart: Material properties of passive myocardium. Chapt 1 in *Theory of Heart: Bioemchanics, Biophysics and Nonlinear Dynamics of Cardiac Function*. Editors: L.Glass, P.J. Hunter and A.D. McCulloch. New York: Springer-Verlag, 1991.

Spencer, A.J.M. *Continuum Mechanics*. Essex: Longman Scientific & Technical, 1980.

Stetson, K.A. A review of speckle photography and interferometry. *Optical Engineering*, 1975, *14*, 482-490.

Stetson, K.A. Phase-step interferometry of irregular shapes by using an edge-following algorithm. *Applied Optics*, 1992, *31*, 5320-5325.

Surrel, Y. Phase stepping: a new self-calibrating algorithm. *Applied Optics*, 1993, *32*, 3598-3600.

Takeda, M., Ina, H. and Kobayashi, S. Fourier-transform method of fringe-pattern analysis for computer-based topography and interferometry. *Journal of the Optical Society of America*, 1982, *72*, 156-160.

Thompson Composants Militaires et Spatiaux. *The CCD Image Sensor*, DB2-CCD-1288, Technical information booklet, 1988.

Thubrikar, M. and Eppink, R.T. A method for analysis of bending and shearing deformations in biological tissue. *Journal of Biomechanics*, 1982, *15*, 529-535.

Tyberg, J.V., Taichman, G.C., Smith, E.R., Douglas, N.W.S., Smiseth, O.A. and Wilbert, J.K. The relationship between pericardial pressure and right atrial pressure: an intraoperative study. *Circulation*, 1986, *73*, 428-432.

Tyrer, J.R. Critical review of recent developments in electronic speckle pattern interferometry. *SPIE: Holographic Nondestructive Testing*, 1986, *604*, 95-111.

Varman, P. and Wykes, C. Smoothing of speckle and Moiré fringes by computer processing. *Optics and Lasers in Engineering*, 1982, *3*, 87-100.

Vikram, C.S., Witherow, W.K. and Trolinger, J.D. Algorithm for phase-difference measurement in phase-shifting interferometry. *Applied Optics*, 1993, *32*, 6250-6252.

Vito, R.P. The role of the pericardium in cardiac mechanics. *Journal of Biomechanics*, 1979, *12*, 587-592.

Vito, R.P. The mechanical properties of soft tissues-I: A mechanical system for bi-axial testing. *Journal of Biomechanics*, 1980, *13*, 947-950.

Wait, R. and Mitchell, A.R. *Finite Element Analysis and Applications*. New York: John Wiley & Sons Ltd., 1985.

Walker, C.A. and McKelvie, J. Optical methods (of NDT). *Non-Destructive Testing of Fibre-Reinforced Plastics Composites, Vol.1*. London: Elsevier Applied Science Publishers, 1987, 105-49.

Weathers, J.M., Foster, W.A., Swinson, W.F. and Turner, J.L. Integration of laser-speckle and finite-element techniques of stress analysis. *Experimental Mechanics*, 1985, *25*, 60-65.

Wyant, J.C., Shagam, R.N., Bescos, J., Hidalgo, A., Plaza, L. and Santamaria, J. Use of electronic phase measurement techniques in optical testing. *Optics Present and Future: Proceedings of the eleventh congress of the international commission for optics ICO-11 Madrid*, 1978, 659-662.

Wyant, J.C., Koliopoulos, C.L., Bhushan, B. and George, O.E. An optical profilometer for surface characterization of magnetic media. *ASLE Transactions*, 1984, *27*, 101-113.

Yin, F.C.P., Chew, P.H. and Zeger, S.L. An approach to quantification of biaxial tissue stress-strain data. *Journal of Biomechanics*, 1986, *19*, 27-37.

Yin, F.C.P., Strumpf, R.K., Chew, P.H. and Zeger, S.L. Quantification of the mechanical properties of non contracting canine myocardium under simultaneous biaxial loading. *Journal of Biomechanics*, 1987, *20*, 577-589.

Zienkiewicz, O.C. and Morgan, K. *Finite Elements and Approximation*. New York: John Wiley & Sons, 1983.

Zioupos, P.N. *Mechanical Properties and Structure of Bovine Pericardium*. PhD thesis, University of Strathclyde, Glasgow, 1989.

Zioupos, P., Barbanel, J.C. and Fisher, J. Mechanical and optical anisotropy of bovine pericardium. *Medical and Biological Engineering & Computing*, 1992, *30*, 76-82.